



Escola Tècnica Superior d'Enginyers
de Camins, Canals i Ports de Barcelona

UNIVERSITAT POLITÈCNICA DE CATALUNYA

PROJECTE O TESINA D'ESPECIALITAT

Títol

**Determination of flutter derivatives of bridge sections based
on wind tunnel experiments under forced excitation**

Autor/a

Robert Fontecha González

Tutor/a

**Joan Ramon Casas Rius
Carles Colomer Segura**

Departament

Enginyeria de la construcció

Intensificació

Data

Gener 2012

Determination of flutter derivatives of bridge sections based on wind tunnel experiments under forced excitation

Author: Robert Fontecha González

Tutors: Carles Colomer Segura and Joan Ramon Casas Rius

Key words: flutter derivatives, flutter, galloping, non-stationary, aeroelastic, coefficients, forced excitation.

Abstract

In the last centuries new technologies and structural knowledge have made possible the construction of filigree structures, which economize the required material quantities by taking material capacity to its limits. However, this evolution has led to structures characterized by low self-weights and low damping capacities, which combined with certain aeroelastic wind effects has proven to be potentially fatal. The breakdown of the Tacoma Narrows Bridge is a good example of how aeroelastic wind effects, even when generated at low wind velocities, can produce resonance vibrations and lead to rapid structure failure.

One of these aeroelastic wind effects is the self-induced vibration, also denoted galloping if it occurs along one single degree of freedom. Classical quasi-stationary wind force approaches based on the linearization of the problem led to unsafe results, and therefore the use of non-linear, non-stationary aeroelastic coefficients (or flutter derivatives) in semi-empirical wind force approaches became necessary.

The goal of this work is to set an algorithm that allows calculating the flutter derivatives of any bridge section using as reference the corresponding methodology developed by Hortmanns. Therefore, the flutter derivatives shall be determined by measuring the dynamic response in wind tunnel experiments of a bridge model under forced excitation. The semi-empirical force approaches of Scanlan and Starossek shall be used to consider the non-stationary character of low-velocity wind effects. The methodology of Hortmanns shall be afterwards enlarged with the calculations and concepts that support the presented algorithm and especially with those relative to the used spectral methods, which have been developed in this thesis. The algorithm will be finally used to determine the flutter derivatives of the Simone-de-Beauvoir footbridge in Paris.

The experiments have been carried out in the wind tunnel of the Institute for Steel Constructions of the RWTH Aachen University.

Determination of flutter derivatives of bridge sections based on wind tunnel experiments under forced excitation

Autor: Robert Fontecha González

Tutores: Carles Colomer Segura y Joan Ramon Casas Rius

Palabras clave: funciones de flameo, galope, no estacionarios, aeroelásticos, coeficientes, oscilación forzada.

Resumen

En los últimos siglos las nuevas tecnologías y conocimientos estructurales han permitido la construcción de estructurasafiligranadas que llevan la capacidad de los materiales hasta sus límites. Sin embargo, esta evolución ha derivado en estructuras de bajo peso propio y reducida capacidad amortiguadora, lo que combinado con ciertos efectos aeroelásticos propios del viento ha demostrado ser potencialmente fatal. La caída del puente de Tacoma Narrows es un buen ejemplo de como los efectos aeroelásticos del viento, incluso cuando éste es de baja velocidad, pueden producir resonancias y llevar a un rápido fallo de la estructura.

Uno de estos efectos aeroelásticos es la vibración autoinducida, también llamada galope si ocurre a lo largo de un único grado de libertad. Los enfoques cuasi-estacionarios clásicos usados para describir la fuerza del viento y basados en linealizaciones del problema han llevado en el pasado a resultados del lado de la inseguridad, por lo que el uso de coeficientes aeroelásticos no lineales y no estacionarios (o funciones de flameo) combinados con enfoques semi-empíricos pasó a convertirse en una necesidad urgente.

El objetivo de este trabajo es establecer un algoritmo que permita calcular las funciones de flameo de una sección de puente cualquiera usando como referencia la metodología desarrollada por Hortmanns. Así, las funciones de flameo serán determinadas midiendo la respuesta durante ensayos en túnel de viento de un modelo de puente sometido a oscilación forzada. Se usarán los enfoques semi-empíricos de Scanlan y Starossek para considerar el carácter no-estacionario de los efectos de un viento de baja velocidad. La metodología de Hortmanns será posteriormente ampliada con los cálculos y conceptos que sirven de base para el algoritmo presentado, especialmente con aquellos relativos a los métodos espectrales, los cuales son originales de esta tesina. El algoritmo será finalmente usado para determinar las funciones de flameo de la pasarela Simone-de-Beauvoir en Paris.

Los experimentos se han llevado a cabo en el túnel de viento del Instituto de Construcciones metálicas de la Universidad RWTH de Aachen.

Acknowledgements

The realization of this work is the result of the help and support of many, to whom I would like to thank.

Thanks firstly to my tutor in Aachen, Carles Colomer, who offered me an early chance to work with him and showed me a way of enjoying this degree I could have never found on my own. Without his support and almost infinite help I could have not realized this thesis.

Thanks to all the workers of the experiments hall of the Institute for Steel Constructions of the RWTH Aachen, who have helped me in mounting the necessary equipment for this work. Especially thanks to Frank for his help and valuable commentaries, and to Fabian for his unexpected but equally welcomed help.

Thanks to Esther Real for being so welcoming and helpful when she had no obligation, and for giving me some useful advice and knowledge about how to begin this work.

Thanks to my internal tutor Joan Ramon Casas for his constant availability and efficiency at facilitating the finalization of this work.

Finally, special thanks to all of those who have walked with me during these university years.

To Carlos and Itsaso for reminding me that there is more than one reality.

To Sergio for inspiring me since the first year to the present day.

To Sandra, Gaba, Nacho and Tornay. I have lived some of the best moments of my life with you, and thanks to you I have been able to escape from the worst ones. Thanks for making me feel that you are going to be there always that I need you and always that I do not.

To Luci, for the immense support and tenderness you have given me. Thanks for understanding and helping me every day, for being a family where there is no home.

Thanks to my father and my brother, for supporting and helping me always that I needed it, even when I did not ask.

This work is dedicated to my mother, from whom I only got pure love and unconditional support, and who, much to my regret, will not be able to see the result of so many steps we walked together.

Table of Contents

Abstract	1
Resumen	2
Acknowledgements	3
Table of Contents	4
List of most commonly used letters and symbols	8
List of Figures	9
List of Tables	10
1 Introduction	11
1.1 Historical background	11
1.2 Scope of works	12
1.3 Aeroelastic phenomena	13
1.3.1 Introduction to the galloping and flutter phenomena	13
1.3.2 Instability condition and onset velocity in galloping oscillations	14
1.3.3 Instability condition and onset velocity in flutter oscillations	19
2 Movement-induced wind forces	21
2.1 Quasi-stationary force approach	21
2.1.1 Linearizations and development of the force expressions	21
2.1.2 Influence of the non-stationary effects on the quasi-stationary force approach...	25
2.1.3 Influence of the non-linear effects on the quasi-stationary force approach	27
2.2 Semi-empirical approaches	28
2.2.1 Semi-empirical Approach by Scanlan and Sabzebari	29
2.2.2 Semi-empirical Approach by Starossek: complex formulation with non-stationary coefficients	30
3 Classic theory for aeroelastic phenomena	32

3.1	Classic galloping theory	32
3.1.1	General	32
3.1.2	Bending galloping oscillations	32
3.1.3	Torsion galloping oscillations	34
3.2	Flutter	35
3.2.1	Generalities and physical description.....	35
3.2.2	Movement equations and calculation of the onset velocity	36
4	Measurement of non-stationary, aeroelastic coefficients	40
4.1	Introduction	40
4.2	Measuring methods	40
4.2.1	Free Oscillation Method (Decrement method).....	40
4.2.2	Forced Oscillation Method (Direct measure of the flow forces)	41
4.2.3	Phase Resonance Method.....	41
4.2.4	Chosen method	42
4.3	Experiment set-up	42
4.3.1	Wind Tunnel.....	42
4.3.2	Test rig.....	43
4.3.3	Force Sensors	46
4.3.4	Bridge model	46
4.4	Measurement parameters.....	48
4.4.1	Preparation of the measurement events.....	48
4.4.2	Determination of the air density.....	48
4.4.3	Excitation frequency and oscillation amplitude	48
4.4.4	Number of measurement values	49
5	Processing of measured non-stationary, aeroelastic coefficients	50
5.1	Introduction	50

5.2	Needed correction algorithms	50
5.2.1	Tilting of the connecting rods	50
5.2.2	Dynamic bending line	51
5.2.3	Phase displacement between sensors	53
5.3	Filtering the measured data	54
6	Calculation algorithms for the non-stationary, aeroelastic coefficients	56
6.1	Introduction to the used spectral analysis concepts	56
6.2	Assumed ideal conditions to solve the problem	59
6.2.1	Dynamics of the bending case.....	59
6.2.2	Dynamics of the torsion case	61
6.3	Use of spectral analysis in order to separate the system forces	62
6.4	Conceptual proceeding to obtain the aerodynamic forces	64
6.5	Calculation of the aerodynamic coefficients	66
6.5.1	Bending case	66
6.5.2	Torsion case.....	69
7	Study case: solution algorithm applied to the Simone-de-Beauvoir footbridge in Paris	71
7.1	Introduction	71
7.2	Considerations previous to the measurements	71
7.3	Setting the measurement parameters	72
7.3.1	Amplitude, excitation frequency and wind velocities	72
7.3.2	Number of values	75
7.4	Processing the measured data	76
7.4.1	Situation before processing the data.....	76
7.4.2	Defining test magnitudes.....	76
7.4.2.1	Bending case	76

7.4.2.2	Torsion case	77
7.4.3	Filtering the data.....	80
7.5	Calculating the non-stationary, aeroelastic coefficients	81
7.5.1	Amplitudes of the magnitude's signals	81
7.5.2	Additional deflection due to lack of stiffness.....	83
7.5.3	Aerodynamic force of the surrounding air	85
7.5.4	Calculating the aerodynamic coefficients	86
8	Results and commentaries	87
8.1	Introduction to the analysis of the results.....	87
8.2	Bending aerodynamic coefficients	88
8.2.1	Results and commentaries	88
8.2.2	Comparison with results of other authors	90
8.3	Torsion aerodynamic coefficients	92
8.3.1	Results and commentaries	92
8.3.2	Comparison with results of other authors	94
8.4	Recommendations to improve the quality of the results	96
9	Conclusions	99
10	Bibliography.....	101
11	ANNEX.....	103
11.1	7 th degree polynomial coefficients:.....	103
11.2	Filter information	104
11.3	Force Transducers.....	108
11.4	Images of the test rig	111

List of Figures

Figure 1.1: Tacoma Narrows bridge during its collapse.....	11
Figure 1.2: Static square under the action of an oblique inflow.	14
Figure 1.3: Moving square under the action of a horizontal inflow.	14
Figure 1.4: Pressure distribution of cases shown in Figure 1.2 and Figure 1.3.....	14
Figure 1.5: Static body under action of inflow with speed u_∞	15
Figure 1.6: Evolution of the aerodynamic coefficient CF_y	19
Figure 1.7: Principal progress of galloping amplitudes.....	19
Figure 2.1: Quasi-stationary wind forces in an oscillating profile.....	22
Figure 2.2: Assumed progress of the aerodynamic force coefficients and linearization according to equations (2.11) to (2.13).....	24
Figure 2.3: Definition of wavelength λ_w in an oscillating body.....	26
Figure 2.4: Definition of non-stationary and quasi-stationary regions and representation of the progress of L in both regions.	27
Figure 2.5: Aerodynamic hysteresis for lineal (left) and nonlinear (right) aeroelastic behavior.	28
Figure 3.1: Two-dimensional object oscillating in the bending degree of freedom (vertical oscillation).	32
Figure 3.2: Two-dimensional object oscillating in the torsion degree of freedom (torsion oscillation).	34
Figure 3.3: Energy balance of a wind force acting on a bluff body during coupled oscillation. Limit case for phase difference $\beta = 0^\circ$	36
Figure 3.4: Energy balance of a wind force acting on a bluff body during coupled oscillation. Maximal force case due to uninterrupted positive work for phase difference $\beta = 90^\circ$	36
Figure 3.5: Two-dimensional object oscillating in both bending and torsion degrees of freedom.	37
Figure 4.1: Equivalent system in Free Oscillation Method and representation of model's movement with decreasing oscillation amplitude and frequency.....	40
Figure 4.2: Equivalent system in Forced Oscillation Method and representation of model's movement with two different oscillation amplitudes and constant frequency.....	41
Figure 4.3: Equivalent system in Phase Resonance Method and conceptual representation of model's movement.	41
Figure 4.4: 3D model of the wind tunnel of the "Institute of steel construction - RWTH Aachen".....	42
Figure 4.5: Cross-section, elevation and plan of the test rig.	43
Figure 4.6: Overall sight of the test rig.....	44
Figure 4.7: Metallic discs at the end of the rotation transmitters.....	44
Figure 4.8: Sight of the connection of the model with the test rig.	45
Figure 4.9: Force sensors in connecting rods during a torsion test.	46
Figure 4.10: Simone-de-Beauvoir footbridge in Bercy, Paris.	47
Figure 4.11: Photo of the model used in the tests.....	47
Figure 5.1: Geometrical relations in the experiment set-up.....	51
Figure 5.2: Simply supported beam under uniform distributed load p	52
Figure 5.3: Beam in a Saint-Venant's torsion state under uniform moment mt	52
Figure 5.4: Phase difference between the different sensors.....	53
Figure 5.5: Example of measured signal before filtering.....	54
Figure 5.6: Unstable zone of a measured signal after applying a band-pass filter of order 10.	55
Figure 6.1: Oscillating mass as idealization of the problem.....	59
Figure 6.2: Simplified oscillating system in the torsion test.....	61
Figure 6.3: Phase angle between F^b , T^t and y^t , and decomposition of F^b , T^t in inertial and aerodynamic forces (F^{bt}) and in damping forces (D^b , y^t).....	63
Figure 6.4: Conceptual determination of the aerodynamic force FT , α , and its decomposition in Fa and Da . ..	64
Figure 6.5: Total force and acceleration signals and angle between them.....	64
Figure 6.6: Determination of complex plane $Re' - Im'$	65
Figure 6.7: Projection of total force with wind action on the plane $Re' - Im'$	65
Figure 6.8: Projection of total force with no wind action on the plane $Re' - Im'$	65
Figure 6.9: Determination of the aerodynamic force and damping.....	66

Figure 6.10: Location and positive direction of the bending test magnitudes. 66

Figure 6.11: Location and positive direction of the torsion test magnitudes. 69

Figure 7.1: Location and positive orientation of the measured forces and accelerations in the bending test..... 77

Figure 7.2: Location and positive orientation of the measured forces and accelerations in the torsion test 78

Figure 7.3: Decomposition of the torsion acceleration of the accelerometer located on the plate at the extreme of the bridge model. 78

Figure 7.4: Change of sign of the forces coefficients after using the CPSD. 79

Figure 8.1: Calculated bending aerodynamic coefficients..... 89

Figure 8.2: Comparison between coefficients $H1^*$ from this work and from the internal study. 90

Figure 8.3: Comparison between coefficients $H4^*$ from this work and from the internal study. 91

Figure 8.4: Comparison between coefficients $A1^*$ and $A4^*$ obtained in this work and those of the internal study..... 92

Figure 8.5: Calculated torsion aerodynamic coefficients 93

Figure 8.6: Comparison between coefficients $A2^*$ from this work and from the internal study..... 94

Figure 8.7: Comparison between coefficients $A3^*$ from this work and from the internal study..... 95

Figure 8.8: Comparison between coefficients $H2^*$ and $H3^*$ obtained in this work and those of the internal study..... 95

Figure 8.9: Bending aerodynamic coefficients obtained with different excitation frequencies. 96

Figure 8.10: Aerodynamic coefficients $H1^*$ and $H4^*$ obtained with minimum oscillation amplitude 0.0135m. 97

Figure 8.11: Aerodynamic coefficients $H1^*$ and $H4^*$ obtained with the recommended parameters. 98

Figure 11.1: Cogged belts connecting the motor to the rotation transmitters. 111

Figure 11.2: Rotation transmitters moves by the cogged belts connected to the motor..... 112

Figure 11.3: General view of the test rig in front of the wind tunnel. 112

Figure 11.4: Side-view of the test rig during a torsion test. 113

Figure 11.5: Frontal view of the test rig during a torsion test..... 114

Figure 11.6: One of the two accelerometers located at middle section..... 117

Figure 11.7: Accelerometer located at one side of the plate of one extreme of the model. 117

List of Tables

Table 7.1: Masses of elements above the force transducers 72

Table 7.2: Range of reachable frequencies for different oscillating amplitudes..... 73

Table 7.3: Undisturbed wind velocities at given frequencies in order to obtain the wanted reduced velocities. . 74

Table 7.4: Variables and magnitudes obtained after applying the solution algorithm explained in section 5. 86

1 Introduction

1.1 Historical background

Throughout history, structures such as buildings and bridges have been designed to resist actions like their own weight and loads of very different nature. New technologies and structural knowledge made the construction of filigree structures possible, which economized the required material quantities by taking material capacity to its limits. Examples of these kinds of constructions are suspension bridges, which can be built with considerably light decks taking advantage of the high traction capacity of steel cables. This kind of structure is however characterized not only by a low self-weight, but also by an extremely reduced damping capacity. This fact proved to be fatal in several cases, being one of the most known the collapse of the Tacoma Narrows Bridge ([28]). This bridge, although being designed to bear its own weight and the appropriate traffic loads, did not take into account the resonance phenomena due to aeroelastic effects of the wind forces, and thus collapsed under the action of a relative low-speed wind force.



Figure 1.1: Tacoma Narrows bridge during its collapse.

A wind force, even when it is not especially strong, can produce resonance vibrations in structures. Examples of this phenomenon are the vortex-excited transversal vibrations and self-induced vibrations, such as the galloping and the flutter phenomena.

Classical wind force approaches used until the second half of the 20th century, which were based on a linearization of the air force and a quasi-stationary treatment of the problem, gave as a result too high and thus unsafe values for the onset velocity, which is the velocity that can start an unstable oscillatory state of a bridge. In fact, quasi-stationary conditions are only

given for high wind speeds over the threshold $u_{red} \approx 20$, a rough reference value used by several authors which, besides, depends on the form of the section (see the definition of u_{red} in section 2.1.2).

This non-stationary character of the wind action causes the air force to have a non-linear dependence of the flow velocity, which must be considered by non-stationary aerodynamic coefficients. These arguments justify the necessity of considering non-stationary effects when studying the galloping and the flutter problems.

1.2 Scope of works

The goal of this work is to investigate an algorithm that allows determining the non-stationary flutter derivatives of any given bridge section. By applying this algorithm, it will be possible to observe the evolution of the aerodynamic coefficients in non-stationary conditions and thus notice if the designed bridge section can show unstable oscillations.

It should be noted that during this thesis different methodologies for the derivation of the aeroelastic coefficients have been investigated and partly self-contained derived. However, most assumptions and principles follow the prior findings from Hortmanns [1]. The aim of this study is therefore also a comprehensive recapitulation of the methods, the set-up and operation of the aerodynamic test rig as well as the assembly of the needed numerical methods. Especially all the presented spectral methods have been newly derived in this thesis.

The work is composed by 9 sections that can be grouped in three blocks.

The first block, which is composed by sections 1 to 3, is an introduction to the galloping and flutter phenomenon. With that purpose, self-induced vibrations will be firstly exposed (section 1.3). Afterwards, the most important wind forces approaches (quasi-stationary and semi-empirical) will be presented and some of them will be explained (section 2). To close this introduction, the explained quasi-stationary force approach will be used in classic theory of aeroelastic phenomena to determine the instability conditions and the expressions of the onset velocity for the galloping and flutter oscillations (section 3).

The second block, composed by sections 4 to 6, deals with the investigation of the algorithm to determinate the non-stationary, aeroelastic coefficients. Therefore it will expose the necessary information for the measurement and calculation of the coefficients. Firstly, section 4 deals with all those aspects relative to the measurement process that should be considered. Section 5 explains how the measured data should be corrected and filtered in order to remove the most important distortions. Finally, section 6 explains some necessary concepts of signal analysis and how they are used together with other calculations to determine the aerodynamic coefficients.

The third block is composed by sections 7 to 9, and contains a particular case (or study case) in which the developed algorithm is tested, the obtained results, commentaries about the results and general conclusions and recommendations. First of all, the concepts explained in sections 4 to 6 are used in section 7 to determine the aerodynamic coefficients of the Simone-de-Beauvoir footbridge in Paris. Section 7 is therefore an example of how the developed

algorithm can be used to calculate these coefficients. In section 8 the results obtained in section 7 will be exposed, commented and compared with results of other authors. Finally, in section 9 the conclusions, recommendations and final commentaries about the work are exposed.

1.3 Aeroelastic phenomena

1.3.1 Introduction to the galloping and flutter phenomena

Natural wind can cause a state of resonance vibrations in different kind of structures through different phenomena, such as vortex shedding, turbulence induced shear-vibrations and self-induced vibrations. The latter ones are the aim of this work.

Self-induced vibrations were firstly detected and exhaustive investigated in airspace engineering, after spontaneous vibration started during different flights, endangering passengers' and the aircraft's safety. After developing an adequate body of theory that could explain the cause of such phenomena, the *flutter* was defined as a case of coupled, self-induced vibration. However, flutter is not an exclusive phenomenon of airspace engineering.

Nowadays the different types of self-induced vibrations are classified using different criteria. This work will differentiate between *galloping* and *flutter* when talking about self-induced vibrations.

Classical flutter can be defined as a self-feeding vibration resulting from a coupling between aerodynamic forces and a structure's natural mode of vibration: that is, the structure's vibration increases the aerodynamic force, which in turn makes the vibration amplitude larger. This process being repeated cyclically depends on the system's energy balance; if the input energy of the aerodynamic force during a cycle is larger than that dissipated by aerodynamic and structure's damping, the amplitude of the vibration will increase until system's failure or until both energies are equaled to each other (see [29]).

In this work, the description above can be used for both galloping and flutter. The only difference between them is the number of degrees of freedom in which the self-induced oscillations occur.

In the *galloping* case oscillations occur only in one degree of freedom, which can be the vertical one, in which case the galloping will be denoted as "bending galloping" or "across-wind" galloping, or the torsion degree of freedom, in which case "torsion galloping" will be used. In both cases they can be also called "uncoupled oscillations".

In the *flutter* case, oscillations occur in both degrees of freedom simultaneously. Therefore they can also be denoted "coupled oscillations", as there is a coupling between both vertical and torsion degrees of freedom.

1.3.2 Instability condition and onset velocity in galloping oscillations

Gallopings oscillations are produced through the interaction between structure's vibrations and the flowing medium. The next images and descriptions, which are based in content of [25], explain in a more clearly way the excitation mechanism of vertical or across-wind galloping:

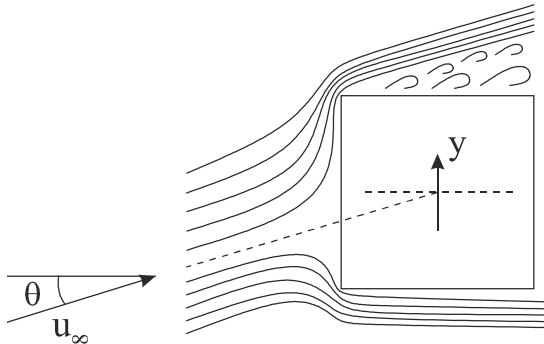


Figure 1.2: Static square under the action of an oblique inflow.

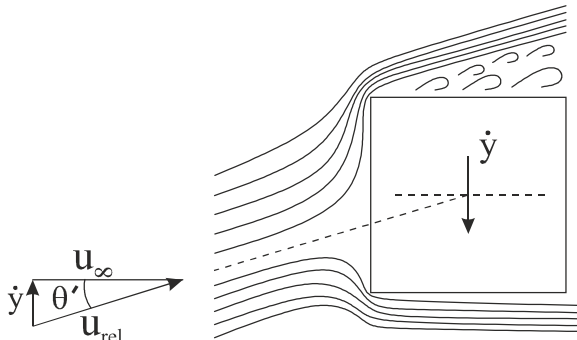


Figure 1.3: Moving square under the action of a horizontal inflow.

The first image (Figure 1.2) represents the case of a static square object under the effect of an oblique air force with attack angle θ and velocity vector u_∞ . This force produces a pressure distribution that can be represented qualitatively like in the third image (Figure 1.4).

In the second image (Figure 1.3) the air velocity vector u_∞ is perfectly horizontal ($\theta = 0$), but the object oscillates with a velocity \dot{y} . From the superposition of both velocity vectors, u_∞ and \dot{y} , results the relative wind velocity vector $u_{rel}(\theta')$. This wind velocity vector, which results from the relative movement between the solid and the existent air flow, produces exactly the same pressure distribution as in the first case, and can therefore also be represented with the third image (Figure 1.4). In this case, the pressure distribution causes a force with the same direction as the movement of the body, and thus reinforcing the oscillation.

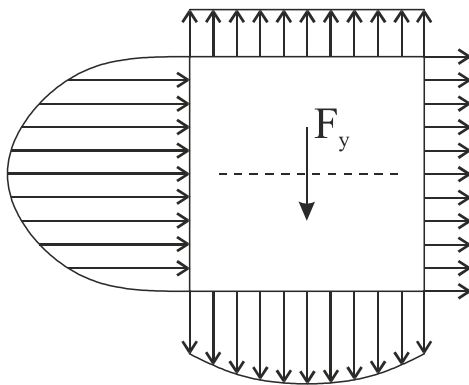


Figure 1.4: Pressure distribution of cases shown in Figure 1.2 and Figure 1.3.

If the energy deriving from this force is bigger than the dissipation energy of the material damping, big oscillation amplitudes will quickly appear.

The fact that an initial oscillation is needed to begin the excitation mechanism is the reason why this phenomenon is called "Movement Induced Excitation" (MIE) or "self-induced vibration".

The instability condition for uncoupled oscillations can be determined starting from these states (Figure 1.2 to Figure 1.4) and using the concepts explained by Scanlan in [2]. In this case, the only degree of freedom that will be studied is the vertical displacement, which corresponds to the across-wind galloping case.

Firstly, it will be considered a fixed, static body under the action of a wind force with angle of attack θ , which corresponds to the case of Figure 1.2 and can be completed through the next image:

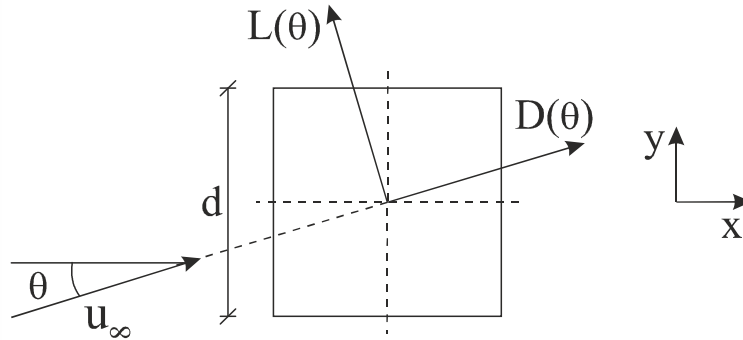


Figure 1.5: Static body under action of inflow with speed u_∞ .

The Drag and Lift forces are defined, respectively, as follows:

$$D(\theta) = \frac{1}{2} \cdot \rho \cdot u_\infty^2 \cdot d \cdot C_D(\theta) \quad (1.1)$$

$$L(\theta) = \frac{1}{2} \cdot \rho \cdot u_\infty^2 \cdot d \cdot C_L(\theta) \quad (1.2)$$

Here $C_D(\theta)$ and $C_L(\theta)$ represent the quasi-stationary, aerodynamic coefficients referred to the attack angle θ .

Taking as reference Figure 1.5 and using the equations (1.1) and (1.2), the vertical force experimented by the body can be determined as follows:

$$F_y(\theta) = D(\theta) \cdot \sin(\theta) + L(\theta) \cdot \cos(\theta) = \frac{1}{2} \cdot \rho \cdot u_\infty^2 \cdot d \cdot C_{Fy}(\theta) \quad (1.3)$$

Where:
$$u = u_\infty \cdot \cos(\theta) \quad (1.4)$$

$$C_{Fy}(\theta) = [C_L(\theta) + C_D(\theta) \cdot \tan(\theta)] \cdot \sec(\theta) \quad (1.5)$$

If now the body is considered to be in an oscillatory state, the situation becomes the one represented in Figure 1.3, which corresponds to the second case. Here the velocities satisfy the next expressions:

$$u_{rel} = \sqrt{u_{\infty}^2 + \dot{y}^2} \quad (1.6)$$

$$\theta' = \arctan \frac{\dot{y}}{u_{\infty}} \quad (1.7)$$

θ' is, according to the notation of this work, the relative attack angle resulting from the oscillatory movement of the section. In this case the system will be assumed as a single-degree-of-freedom oscillatory body with mass m per unit length, linear mechanical damped and elastically supported:

$$m[\ddot{y} + 2\mu\omega_n\dot{y} + \omega_n^2y] = F_y \quad (1.8)$$

Here μ is the damping ratio, ω_n the natural circular frequency and F_y the aerodynamic force acting on the body. F_y is assumed to be the same as in (1.3), as the coefficients $C_L(\theta')$ and $C_D(\theta')$ are considered to be the same in oscillatory and the fixed body.

If now a small motion is considered, the body will oscillate with velocities close to $\dot{y} = 0$, wherein:

$$\theta' \cong \frac{\dot{y}}{u_{\infty}} \cong 0 \quad (1.9)$$

With this condition, the aerodynamic force can be expressed as:

$$F_y \cong F_y(\theta' = 0) + \left. \frac{\partial F_y}{\partial \theta'} \right|_{\theta'=0} \cdot \theta' = \left. \frac{\partial F_y}{\partial \theta'} \right|_{\theta'=0} \cdot \theta' \quad (1.10)$$

This expression makes necessary the analysis of the coefficient $C_{Fy}(\theta')$ around $\theta' = 0$, as it is the only component of F_y that depends on the angle value according to expression (1.3). This is done through differentiation of expression (1.5) at $\theta' = 0$, obtaining

$$\left. \frac{dC_{Fy}}{d\theta'} \right|_{\theta'=0} = - \left(\left. \frac{dC_L}{d\theta'} + C_D \right) \right|_{\theta'=0} \quad (1.11)$$

This leads to the next movement equation for small motion, which yields from substituting the right term of expression (1.8) by the results in expressions (1.10) and (1.11):

$$m[\ddot{y} + 2\mu\omega_n\dot{y} + \omega_n^2 y] = -\frac{1}{2}\rho u_\infty^2 d \left(\frac{dC_L}{d\theta'} + C_D \right) \Big|_{\theta'=0} \cdot \frac{\dot{y}}{u_\infty} \quad (1.12)$$

As both system damping and aerodynamic force share a linear relation with the body velocity \dot{y} , the aerodynamic force can be considered as a contribution to the overall system damping, obtaining as a result a system damping coefficient:

$$2m\mu\omega_n + \frac{1}{2}\rho u_\infty d \left(\frac{dC_L}{d\theta'} + C_D \right) \Big|_{\theta'=0} \quad (1.13)$$

Two terms can be identified in this coefficient: the first one corresponds to the mechanical damping, whereas the second one is denoted “aerodynamic damping” ([2]). As in a single-degree-of-freedom oscillator with viscous damping, the oscillatory movement will tend to stability if the damping coefficient is positive and to instability if it is negative. Since μ is usually positive, instability can only happen if the aerodynamic damping is negative:

$$\left(\frac{dC_L}{d\theta'} + C_D \right) \Big|_{\theta'=0} < 0 \quad (1.14)$$

This condition is known as the Glauer-Den Hartog criterion, which is a *necessary* condition for the appearance of galloping instability.

This criterion is analogous to the condition shown in [1], which was already presented by Den Hartog in 1936 (see [5]), as he stated that aerodynamic stability depends on the growth of the aerodynamic force F_y with variation of the flow angle θ :

- $\frac{dF_y}{d\theta} < 0$, instability
- $\frac{dF_y}{d\theta} > 0$, stability

These conditions, which are focused in the aerodynamic force itself, mean that a given section will present galloping instability if the growth of F_y respect to the growth of θ is negative, which means the aerodynamic force F_y acts in the same direction as the body velocity vector and therefore reinforces the oscillatory movement.

Returning to the previous expressions, it is immediate to realize that, while the expression (1.14) is a *necessary* condition, a *sufficient* condition for apparition of across-wind galloping is a negative total damping coefficient, which can be expressed as

$$2m\mu\omega_1 + \frac{1}{2}\rho u_\infty d \left(\frac{dC_L}{d\theta'} + C_D \right) \Big|_{\theta'=0} < 0 \quad (1.15)$$

It can be therefore stated, that the study of section stability can be reduced to the study of the aerodynamic coefficient $C_{Fy}(\theta')$ (Scanlan [2]). A detailed study of the evolution of this coefficient is normally carried out through a development of C_{Fy} in powers of \dot{y}/u_∞ , which is the factor that corresponds to the tangent of θ' for small motion.

This development was presented by Novak ([8], [10]), and consists on an abbreviated power series with several odd powers of \dot{y}/u_∞ and an appropriately signed second-power term to smooth the fit:

$$C_{Fy} = A_1 \left(\frac{\dot{y}}{u_\infty} \right) - A_2 \left(\frac{\dot{y}}{u_\infty} \right)^2 \frac{\dot{y}}{|\dot{y}|} - A_3 \left(\frac{\dot{y}}{u_\infty} \right)^3 + A_5 \left(\frac{\dot{y}}{u_\infty} \right)^5 \dots \quad (1.16)$$

As this expression assumes the motion of the body to be small, it can also be linearized making only necessary the first coefficient, which takes the value of $A_1 = dC_{Fy}/d\theta'$. This linearization is used in the most used expression of the onset velocity, which is mostly used due to the absence in the standard of alternative proceeding descriptions for galloping study ([1]).

This expression, given in this way in different standards (see [26], [27]), will be commented now but developed with more detail in section 3.1:

$$u_{on} = \frac{2 \cdot m \cdot \delta_{s,y}}{\rho \cdot d^2} \cdot \frac{2 \cdot f_e \cdot d}{-\frac{dC_{Fy}}{d\theta'}} \quad (1.17)$$

Here f_e is the natural frequency of the body and $\delta_{s,y}$ the logarithmic decrement of the structure damping. According to the way the stability parameter $dC_{Fy}/d\theta'$ has been defined, it is a constant value that depends only on the form of the profile form. This would involve the onset velocity having a linear relation with the damping $\delta_{s,y}$, while other physical and geometric dimensions would present a constant contribution. These properties have proved to be wrong due to different reasons. First of all, this equation implies the appearance of the onset velocity in quasi-stationary flow conditions (an assumption for the linearization), which is not always true ([1]). Examples of this are cases of high oscillating frequencies or big section widths, where non-stationary effects play an important role and cause the surpassing of the onset velocity in non-stationary conditions. Another argument against this expression is the fact that double damping does not imply double onset velocity as the expression suggests ([1]). It has been shown in some tests that doubling the structure damping can increase at most a 20% the onset velocity for torsion galloping oscillations. Another problem of this expression is the divergence of values given to the stability parameter $dC_{Fy}/d\theta'$ in the literature, which can be due to different grades of turbulence during simulations and different types of tests ([1]). These reasons among others justify the necessity of considering non-stationary effects in the study of the onset velocity.

The linearization that leads to expression (1.17) can also be avoided through considering more terms of the development presented by Novak shown in expression (1.16), which makes

possible finding stationary limit amplitudes. Here limit amplitudes are determined by aerodynamics. The results obtained by Novak starting from expression (1.16) can be summarized in Figure 1.6 and Figure 1.7.

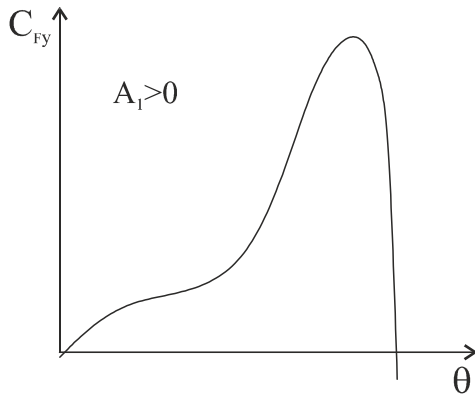


Figure 1.6: Evolution of the aerodynamic coefficient C_{Fy}

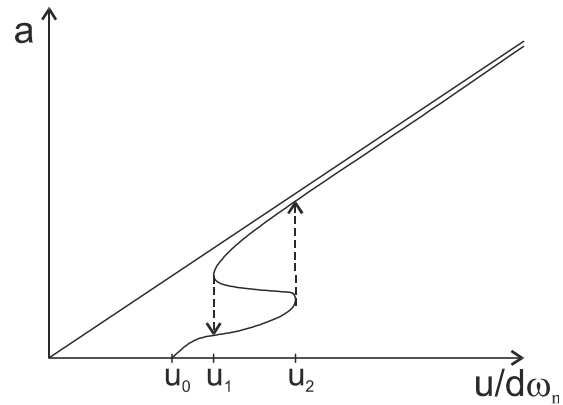


Figure 1.7: Principal progress of galloping amplitudes

These figures illustrate the response curve from a square section under smooth airflow, and show the possible values for the coefficient C_{Fy} depending on the value of θ and the possible values of the galloping response amplitudes a as functions of the reduced velocity $u/d\omega_n$. The amplitudes in Figure 1.7 can only take the values from the upper and the lower branch through following the discontinuous lines.

This graphic enables therefore the calculation of the galloping amplitudes only for stationary, linear systems.

The influence of turbulence in the galloping phenomenon is in general not clear. For example, Hortmanns ([1]) states that turbulent flow diminishes the magnitude of the minimal necessary perturbation that makes the profile oscillate on its own. Parkinson and Smith ([12]) stated that, depending on the profile form, turbulence can have a stabilizer or destabilizer effect. Novak affirmed in ([8]) that turbulence can transform steady oscillations into unsteady ones (as for example in [10], where he showed how a rectangular section with ratio $B/d=10$, which was stable with smooth flow, became unstable in turbulent flow), reduce the magnitude of the aerodynamic damping and, in certain cases, depending upon its scale and intensity, even destroy the necessary conditions for galloping. More about Novak's considerations relative to the effects of turbulence on galloping instability can be found in [11].

1.3.3 Instability condition and onset velocity in flutter oscillations

As it was explained in section 1.3.1, the term "flutter" is usually used to denote coupled oscillations with bending and torsion degrees of freedom.

The first theory addressed to determine flutter onset velocity was developed by Theodorsen [18]. The studied case was however the case of thin airfoils in incompressible flow. Theodorsen used basic principles of potential flow theory to show that the expressions for the

lift and the drag forces, $L(\theta)$ and $D(\theta)$, are linear in y and φ (vertical and torsion movements) and in their first and second derivatives respectively. In the expressions of such forces appears a coefficient called Theodorsen's circulation function, a function composed by two theoretical functions $F(k)$ and $G(k)$, which are its real and imaginary part respectively. These functions define the *aerodynamic coefficients*, which have been determined for a vast number of cases through wide and prolonged research.

In the case of bluff objects, common in civil engineering, it has not been possible to develop expressions for the aerodynamic coefficients with basic fluid-flow principles yet. Different authors ([4], [7]) have tried unsuccessfully to introduce correction coefficients in Theodorsen's theory to adjust it to the bluff body case.

However, it has been shown in [90] that self-excited lift and moment may be treated as linear in vertical displacement, rotation and their first and second derivatives for small oscillations, and that it is possible to measure the aerodynamic coefficients in specially designed wind tunnel tests, what indicates that aerodynamic coefficients of bluff bodies are functions of the reduced velocity.

Scanlan ([1],[14], [15], [16]) proposed the most used air-force approach with non-stationary coefficients. This approach allows the determination of the onset velocity by imposing the phase shift between bending oscillations and torsion oscillation equal to zero. Further explanation about Scanlan's approach will be given in section 2.2.1 and along section 3.

2 Movement-induced wind forces

2.1 Quasi-stationary force approach

2.1.1 Linearizations and development of the force expressions

This section deals with the linearized, quasi-stationary force approach. It is therefore aimed to describe the aerodynamic forces that result from an incident flow on an oscillatory, bluff-body section, and is based on the concepts exposed in [1].

This approach uses some linearization in order to describe the movement-induced wind forces. The assumptions that justify them are the next ones:

- a. Slim and line-form bending and torsion systems: as a result, the aerodynamic forces will be treated as two-dimensional line forces.
- b. Incompressible flow.
- c. Symmetric or double-symmetric sections.
- d. The incident flow has the same shape over the whole span.
- e. The turbulence, oscillation amplitudes and incident angle θ depend on the force approach.

This approach also considers a linear relation between displacements and air force. This assumption is especially adequate for small oscillation amplitudes and for unique aerodynamic displacement-force relations. Therefore the quasi-stationary aerodynamic coefficients will be taken as linear coefficients.

In order to limit the amount of study cases, the case of horizontal flow will be considered below. This flow will act on a rectangular section that is carrying out an oscillatory movement in both bending and torsion degrees of freedom. Expressions for the aerodynamic lift and moment will be developed, which will consider the relative incident inflow angle due to the section's oscillatory movement.

The movement-induced wind forces resulting from aeroelastic effects are represented in the next figure:

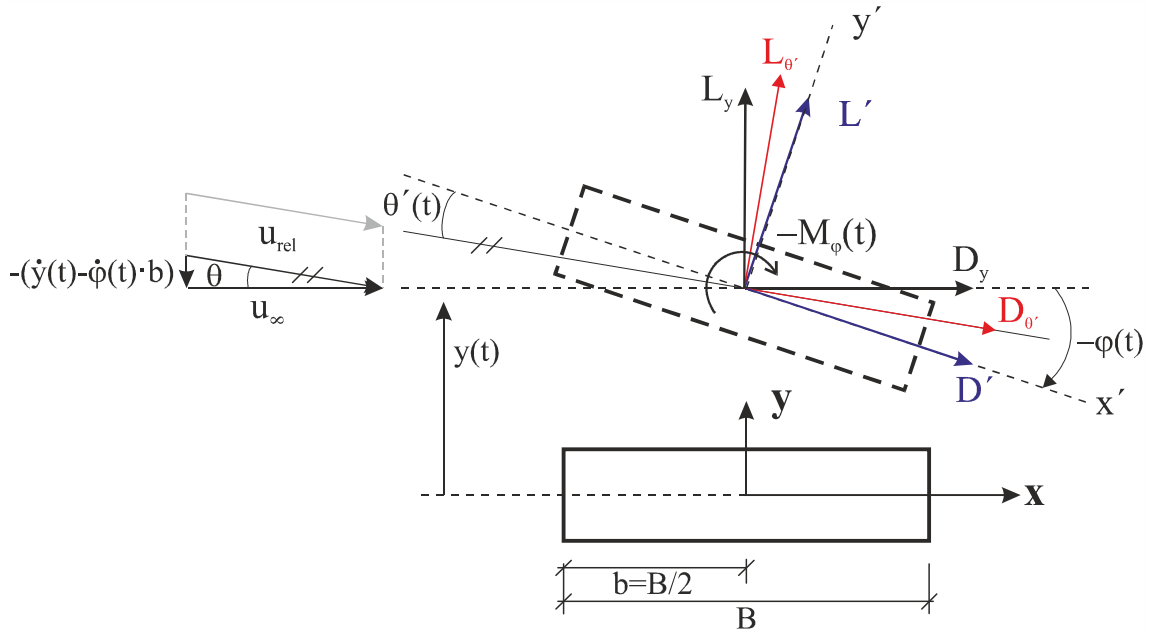


Figure 2.1: Quasi-stationary wind forces in an oscillating profile

It is important to note the difference between $\theta(t)$ and $\theta'(t)$. The first one is the incident flow angle referred to the global coordinate system, while the second one is the incident flow angle referred to the local (body-fixed) coordinate system.

Taking this consideration into account, the aerodynamic forces referred to the inflow velocity u_{rel} can be determined as follows:

$$L_{\theta'}(t) = \frac{\rho}{2} \cdot u_{rel}^2 \cdot B \cdot C_L(\theta'(t)) \quad (2.1)$$

$$D_{\theta'}(t) = \frac{\rho}{2} \cdot u_{rel}^2 \cdot B \cdot C_D(\theta'(t)) \quad (2.2)$$

$$M_{\theta'}(t) = \frac{\rho}{2} \cdot u_{rel}^2 \cdot B^2 \cdot C_M(\theta'(t)) \quad (2.3)$$

The coefficients $C_L(\theta'(t))$, $C_D(\theta'(t))$ and $C_M(\theta'(t))$ of the previous expressions are the quasi-stationary, aerodynamic coefficients referred to the attack angle $\theta'(t)$.

The system represents a section with width B and degrees of freedom $y(t)$ and $\varphi(t)$. If the vertical displacement and the rotation movements are small, the relative inflow angle $\theta'(t)$ can be linearized and, if it is referred to the windward edge, expressed as:

$$\theta'(t) = \varphi(t) + \frac{-\dot{y}(t) + \dot{\varphi}(t) \cdot b}{u_{\infty}} \quad (2.4)$$

Here the center of motion is considered to coincide with the center of gravity. This assumption is not completely true, but as the distance between both centers is small and its calculation requires high-cost procedures, it is normally considered as a good assumption.

The lifting force in the global system $L_y(t)$ is given by:

$$L_y(t) = \frac{\rho}{2} \cdot u_\infty^2 \cdot B \cdot C_L(t)|_{\theta=0} = q \cdot B \cdot C_L(t)|_{\theta=0} \quad (2.5)$$

This force can also be expressed as the projection of the aerodynamic forces referred to the inflow velocity u_{rel} , which are $L_{\theta'}(t)$ and $D_{\theta'}(t)$, on the axis of the global coordinates system $x - y$:

$$\begin{aligned} L_y(t) &= L_{\theta'}(t) \cdot \cos(\varphi(t) - \theta'(t)) - D_{\theta'}(t) \cdot \sin(\varphi(t) - \theta'(t)) = \\ &= \frac{\rho}{2} \cdot u_{rel}^2 \cdot B \cdot C_L(\theta') \cdot \cos(\varphi(t) - \theta'(t)) - \frac{\rho}{2} \cdot u_{rel}^2 \cdot B \cdot C_D(\theta') \cdot \sin(\varphi(t) - \theta'(t)) \end{aligned} \quad (2.6)$$

For small deviations, the inflow velocity u_{rel} can be expressed as follows:

$$u_{rel} = \frac{u_\infty}{\cos(\varphi - \theta')} \quad (2.7)$$

Introducing (2.7) into (2.6) it yields:

$$L_y(t) = \frac{\rho}{2} \cdot B \cdot u_\infty^2 \cdot \left[\frac{C_L(\theta') \cdot \cos(\varphi(t) - \theta'(t)) - C_D(\theta') \cdot \sin(\varphi(t) - \theta'(t))}{\cos^2(\varphi(t) - \theta'(t))} \right] \quad (2.8)$$

At this point it is necessary to examine the aerodynamic coefficients. First of all, the lift coefficient $C_L(t)|_{\theta=0}$ in a global coordinate system is given by:

$$C_L(t)|_{\theta=0} = C_L(\theta'(t)) \cdot \frac{1}{\cos(\varphi(t) - \theta'(t))} - C_D(\theta'(t)) \cdot \frac{\tan(\varphi(t) - \theta'(t))}{\cos(\varphi(t) - \theta'(t))} \quad (2.9)$$

If this expression is linearized (which means $\cos(\varphi - \theta') \approx 1$ and $\tan(\varphi - \theta') \approx \varphi - \theta'$) it yields:

$$C_L(t)|_{\theta=0} \simeq C_L(\theta'(t)) - C_D(\theta'(t)) \cdot (\varphi(t) - \theta'(t)) \quad (2.10)$$

This expression corresponds to the part between brackets in equation (2.8) if it is assumed that deviations (and therefore also angles) are small. If these deviations are small enough, the aerodynamic coefficients can be linearized through a polynomial approach:

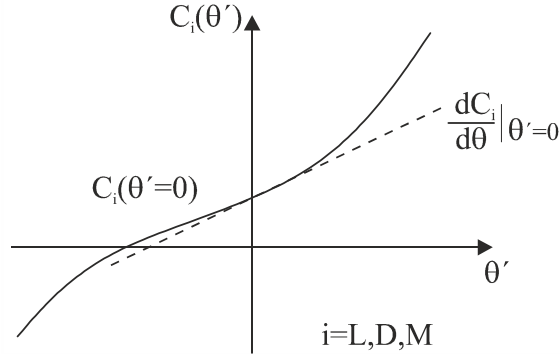


Figure 2.2: Assumed progress of the aerodynamic force coefficients and linearization according to equations (2.11) to (2.13)

$$C_L(\theta'(t)) = C_L(\theta' = 0) + \left. \frac{dC_L}{d\theta'} \right|_{\theta'=0} \cdot \theta' \quad (2.11)$$

$$C_D(\theta'(t)) = C_D(\theta' = 0) + \left. \frac{dC_D}{d\theta'} \right|_{\theta'=0} \cdot \theta' \quad (2.12)$$

$$C_M(\theta'(t)) = C_M(\theta' = 0) + \left. \frac{dC_M}{d\theta'} \right|_{\theta'=0} \cdot \theta' \quad (2.13)$$

If the expressions of the aerodynamic coefficients (2.11) to (2.13) and the expression of the relative angle θ' (2.4) are introduced in expression (2.10), which corresponds to the previously linearized expression of C_L , it yields:

$$C_L(t)|_{\theta=0} = \left[C_L(\theta' = 0) + \left. \frac{dC_L}{d\theta'} \right|_{\theta'=0} \right] \cdot \left(\varphi(t) + \frac{-\dot{y}(t) + \dot{\varphi}(t) \cdot b}{u_\infty} \right) - \left[C_D(\theta' = 0) + \left. \frac{dC_D}{d\theta'} \right|_{\theta'=0} \right] \cdot \left(\varphi(t) - \varphi(t) - \frac{-\dot{y}(t) + \dot{\varphi}(t) \cdot b}{u_\infty} \right) \quad (2.14)$$

Theoretically $C_L(\theta' = 0)$ is zero for symmetric sections. If now quadratic terms are neglected (like the products of the form “angle · angle”), expression (2.14) becomes:

$$C_L(t)|_{\theta=0} = \left(\left. \frac{dC_L}{d\theta'} \right|_{\theta'=0} + C_D(\theta' = 0) \right) \cdot \left(\frac{-\dot{y}(t) + \dot{\varphi}(t) \cdot b}{u_\infty} \right) + \left. \frac{dC_L}{d\theta'} \right|_{\theta'=0} \cdot \varphi(t) \quad (2.15)$$

The acceleration of the surrounding air due to the movement of the section produces the apparition of one more aerodynamic force, which according to Theodorsen [18] can be theoretically expressed in a normalized form as:

$$\frac{L_{\ddot{y}}(t)}{q \cdot B} = -\frac{\pi}{2} \cdot \frac{B}{u_{\infty}^2} \cdot \ddot{y}(t) \quad (2.16)$$

This aerodynamic force and its torsion version will be known in this work as ‘‘Theodorsen’s forces’’. If this force due to the acceleration of the surrounding air (2.16) is added to the lifting force in (2.5), the resulting lifting force can be expressed in a compact form as:

$$\frac{L_y(t)}{q \cdot B} = C_L(t)|_{\theta=0} - \frac{\pi}{2} \cdot \frac{B}{u_{\infty}^2} \cdot \ddot{y}(t) \quad (2.17)$$

Here q is the mean velocity pressure $q = \frac{\rho}{2} \cdot u_{\infty}^2$.

If expression (2.17) is developed using the result exposed in (2.15), the final expression of the lifting force is obtained:

$$\frac{L_y(t)}{q \cdot B} = -\frac{\pi}{2} \frac{B}{u_{\infty}^2} \ddot{y}(t) + \left(\frac{dc_L}{d\theta'} \Big|_{\theta'=0} + c_D(\theta' = 0) \right) \left(\frac{-\dot{y}(t) + \dot{\varphi}(t) \cdot b}{u_{\infty}} \right) + \frac{dc_L}{d\theta'} \Big|_{\theta'=0} \cdot \varphi(t) \quad (2.18)$$

An analog procedure can be carried out to obtain the air force moment, whose resulting expression is:

$$\frac{-M_{\varphi}(t)}{q \cdot B^2} = -\frac{\pi}{4} \cdot \frac{B^2}{16 \cdot u_{\infty}^2} \cdot \ddot{\varphi}(t) + \frac{dc_M}{d\theta'} \Big|_{\theta'=0} \cdot \left(\varphi(t) + \frac{-\dot{y}(t) + \dot{\varphi}(t) \cdot b}{u_{\infty}} \right) \quad (2.19)$$

Expressions (2.18) and (2.19) represent the lift force and moment assuming quasi-stationary conditions and the linearizations that have been explained along their development in this section. In the next sections it will be briefly exposed why these assumptions may lead to wrong results and must therefore be changed.

2.1.2 Influence of the non-stationary effects on the quasi-stationary force approach

The quasi-stationary approach can only be used if the wind speeds are high or/and the oscillation frequencies are low. These are the conditions that are usually given in an instability study. A measure of instability is the reduced frequency K :

$$K = \frac{B \cdot f_e}{u_{\infty}} \quad \text{or} \quad K = \frac{B \cdot \omega}{u_{\infty}} \quad (2.20)$$

Another measure is its reciprocal value, the reduced velocity u_{red} , which can be normalized with the section width B :

$$u_{red,B} = \frac{u_\infty}{B \cdot f_e} = \frac{u_\infty/f_e}{B} = \frac{\lambda_W}{B} \quad (2.21)$$

Here f_e is the frequency $f_e = (\sqrt{k/m})/2\pi$, which coincides with the excitation frequency.

Hortmanns ([1]) compares the reduced velocity u_{red} with the wavelength λ_W of the trailing flow normalized with a section width B that results in a case like the one represented in the next image:

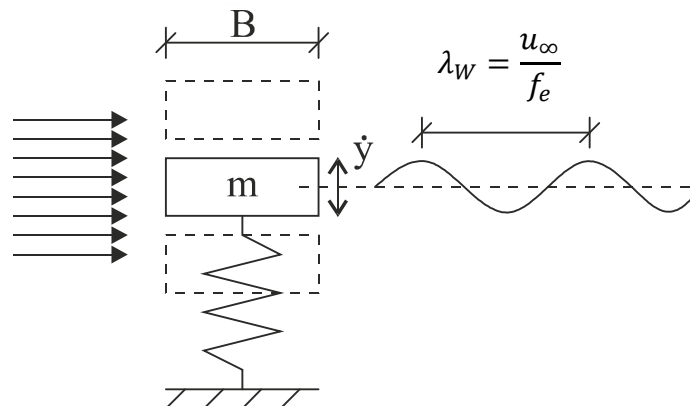


Figure 2.3: Definition of wavelength λ_W in an oscillating body

If the value of u_{red} is high (due to a high λ_W or to a small width B), it can be assumed that the action of the wind affects instantaneously to the whole section and therefore any change of the flow boundary conditions in the windward side will be very quickly transmitted to the rest of the section. In conclusion, the higher the value of u_{red} is, the more quasi-stationary the flow will be.

On the other hand, if u_{red} is small, any change of the boundary conditions in the windward side will need some time to affect to the rest of the section. The consequence of this phenomenon is the simultaneous action in the section of different forces, which results of simultaneous interaction of the present time step and various different past ones.

The limit value of u_{red} in which the non-stationary and the quasi-stationary states are divided depends on the experiment and is usually not precisely defined. Höffer [6] proposes a value of $u_{red} \approx 20$ for double-symmetric bridge profiles, a value that is dependent on the profile geometry though. Figure 2.4 is a graphic representation of the evolution of the non-stationarity grade with the growth of u_{red} :

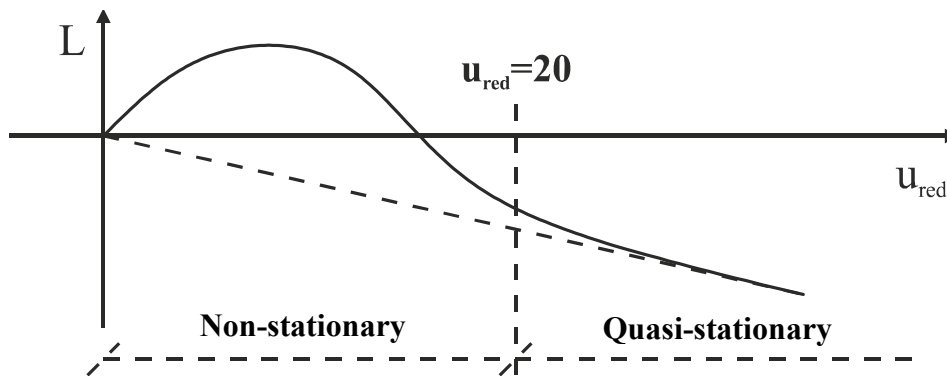


Figure 2.4: Definition of non-stationary and quasi-stationary regions and representation of the progress of L in both regions.

The non-stationary effects can be measured in wind tunnel experiments, or considered with coefficient functions which depend on the oscillation amplitude and the turbulence grade ([2],[6]).

The phenomenon of non-stationarity has been already considered by some authors, who developed semi-empirical force approaches to include non-stationary effects. These approaches will be treated in section 2.2.

2.1.3 Influence of the non-linear effects on the quasi-stationary force approach

Most approaches and procedures assume a linear relation between displacements and air forces, a linearization that is not acceptable if the displacement-force curves show big curvatures or if they are not clear enough as to confirm a linear relation.

If the absolute oscillation amplitude is wanted, which implies considering big displacements, non-linear calculations will be necessary. Besides, a non-linear approach may be necessary for certain profiles and inflow angles.

For these non-linear approaches the dependence of the oscillation amplitude, the inflow angle and the turbulence should be considered. Some aspects about non-linearities are commented below:

a. Aerodynamic Hysteresis

In the linear elastic theory of harmonic oscillations a constant phase-shifting between displacements and air forces configures an elliptic hysteresis. However, for determined profiles the resultant hysteresis curve is a self-cutting curve that changes its run sense ([10], [13],[17]). This makes necessary the consideration of non-linear effects for these profiles.

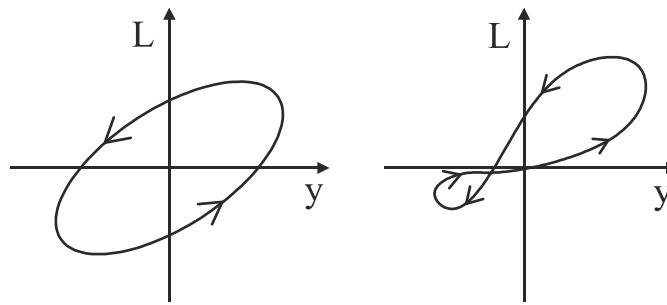


Figure 2.5: Aerodynamic hysteresis for lineal (left) and nonlinear (right) aeroelastic behavior.

b. Displacement of the center of rotation

A displacement of the center of rotation occurs always that a profile exhibits a rotation movement ([1]). Therefore it should be always considered when determining the non-stationary coefficients.

However, this displacement, most often referred to the position of the center of mass, can only be estimated, and thus is usually ignored or neglected. This phenomenon is the reason why tests with forced excitation and those with the method of the free oscillations can give different results to the same problem, as in forced excitation both centers are mechanically forced to coincide.

c. Consideration of non-linear effects through the aero-elastic coefficients

Non-linear effects can lead to stabilization of amplitudes caused by the onset velocity as well as they can lead to instability while the profile is oscillating at amplitudes caused by velocities inferior to the onset velocity ([1]).

In the quasi-stationary formulation of the dynamic wind forces the aerodynamic coefficients are expressed using the relative flow attack angle θ' , which implicitly contains information about the oscillating velocity \dot{y} . If, contrary to what has been done in section 2.1.1, the expression of the aerodynamic coefficients is not linearized, nonlinearities for quasi-stationary conditions can be taken into account.

However this formulation of the aerodynamic coefficient does not consider their dependence of the oscillating velocity. To consider aeroelastic effects emerged from the coupling between the oscillating system and the incident flow, dynamic tests must be carried out. Thus the non-linear coefficients can be expressed through a curve which depends on the oscillating amplitude.

2.2 Semi-empirical approaches

In the case of aerospace engineering, Theodorsen studied the case of an airfoil under the action of a quasi-stationary inflow. In this case he could determine exactly the resulting aerodynamic forces using a potential approach based on fluids theory.

However, that approach cannot be used in the typical cases of bluff-body sections in civil engineering. Various authors tried unsuccessfully to determine correction functions that could adapt Theodorsen's solution to the bluff-body cases. Linear approaches had to be developed then to obtain an approximate solution to this problem (see for example previous section). However, they led to unsafe solutions, as they do not consider non-stationary effects.

In order to consider non-stationary effects, semi-empirical approaches were developed. The main difference between them and the linear ones, is that semi-empirical approaches use non-stationary coefficients to consider the aerodynamic forces' dependence of the reduced velocity u_{red} . These non-stationary coefficients contain therefore the necessary information of non-stationary effects, and thus can offer more accurate and safe solutions to the problem.

2.2.1 Semi-empirical Approach by Scanlan and Sabzebari

This is probably the oldest and most well-known approach for non-stationary wind forces. It was first presented by Scanlan and Sabzebari in 1969 ([14]). The expression of these forces is done in an abstract, system-oriented way. According to this approach only the aeroelastic coefficients can be measured in the wind tunnel, while correction functions cannot be determined this way. These functions will therefore be calculated using the measured coefficients and the results of static and dynamic measurements.

The air forces according to Scanlan and Sabzebari are defined as follows:

$$L_y = m \cdot (H_1 \cdot \dot{y} + H_2 \cdot \dot{\varphi} + H_3 \cdot \varphi + H_4 \cdot y) \quad (2.22)$$

$$M_\varphi = \theta \cdot (A_1 \cdot \dot{y} + A_2 \cdot \dot{\varphi} + A_3 \cdot \varphi + A_4 \cdot y) \quad (2.23)$$

Coefficients H_i and A_i ($i = 1 - 4$) are bounded dimensionally (have dimensions) and depend on ω_y , ω_φ , and on the reduced frequencies K_y and K_φ . This fact is the main obstacle in the computational approach for the transferability to other scales and possible solving mechanisms.

If dimensionless coefficients H_i^* and A_i^* are used, and the reduced frequencies K_y and K_φ are considered as the 2π -times reduced frequencies (as shown in the first part of expression (2.20), where $K = \frac{B \cdot f_e}{u_\infty} = \frac{B \cdot \omega}{u_\infty \cdot 2\pi}$), the expressions of the air forces become:

$$L_y = \left(\frac{1}{2} \cdot \rho \cdot u_\infty^2 \right) \cdot (2B) \cdot (K_y H_1^* \cdot \frac{\dot{y}}{u_\infty} + K_\varphi H_2^* \cdot \frac{B \cdot \dot{\varphi}}{u_\infty} + K_\varphi^2 H_3^* \cdot \varphi + \frac{K_y^2}{B} H_4^* \cdot y) \quad (2.24)$$

$$M_\varphi = \left(\frac{1}{2} \cdot \rho \cdot u_\infty^2 \right) \cdot (2B^2) \cdot (K_y A_1^* \cdot \frac{\dot{y}}{u_\infty} + K_\varphi A_2^* \cdot \frac{B \cdot \dot{\varphi}}{u_\infty} + K_\varphi^2 A_3^* \cdot \varphi + \frac{K_y^2}{B} A_4^* \cdot y) \quad (2.25)$$

Through the aeroelastic coefficients H_i^* and A_i^* , also called ‘Flutter Derivatives’, both aeroelastic effects and influence of the non-stationary effects can be considered.

2.2.2 Semi-empirical Approach by Starossek: complex formulation with non-stationary coefficients

A complex formulation of the problem offers considerable advantages in comparison with the standard formulation. This approach was presented by Starossek ([17]) and is analog to the one from Scanlan and Sabzevari (section 2.2.1). As a result, the coefficients of both approaches can be switched with an easy transformation. In this work calculations will be done using Starossek's coefficients, but results will be translated and presented in Scanlan's notation (as "flutter derivatives") in order to enable an easier comparison with other author's results.

Starossek's approach will be explained through matrix expressions. First of all, the forces vector is taken as:

$$F_L := \begin{pmatrix} L_y \\ M_\varphi \end{pmatrix} \quad (2.26)$$

The displacement vector is expressed using complex formulation:

$$r := \begin{pmatrix} y \\ \varphi \end{pmatrix} = \begin{pmatrix} y_0 \cdot e^{i\omega_y t - \beta_y} \\ \varphi_0 \cdot e^{i\omega_\varphi t - \beta_\varphi} \end{pmatrix} \quad (2.27)$$

where ω_y and ω_φ are the circular frequencies. Its time derivatives are therefore:

$$\begin{aligned} \dot{r} &= i \cdot \omega_j \cdot r \\ \ddot{r} &= -\omega_j^2 \cdot r \end{aligned} \quad \begin{matrix} j = y, \varphi \\ \\ \end{matrix} \quad (2.28)$$

The force vector can be now expressed as:

$$F_L := \pi \cdot \rho \cdot b^2 \cdot C^* \cdot \begin{pmatrix} y \cdot \omega_y^2 \\ \varphi \cdot \omega_\varphi^2 \end{pmatrix} \quad (2.29)$$

Where C^* is the matrix of complex coefficients $c_{ik} = c'_{ik} + i \cdot c''_{ik}$, which can be developed as follows:

$$C^* = \begin{pmatrix} c_{yy} & b \cdot c_{y\varphi} \\ b \cdot c_{\varphi y} & b^2 \cdot c_{\varphi\varphi} \end{pmatrix} = \begin{pmatrix} c'_{yy} + i \cdot c''_{yy} & b \cdot (c'_{y\varphi} + i \cdot c''_{y\varphi}) \\ b \cdot (c'_{\varphi y} + i \cdot c''_{\varphi y}) & b^2 \cdot (c'_{\varphi\varphi} + i \cdot c''_{\varphi\varphi}) \end{pmatrix} \quad (2.30)$$

These coefficients are referred to the section width $b = B/2$, an important fact that must be considered when comparing and observing results. Taking into account this fact and comparing these equations with the ones from Scanlan's approach, the next relations between coefficients can be settled:

$$\begin{aligned}
 H_1^* &= \frac{\pi}{4} \cdot c''_{yy} , & H_2^* &= \frac{\pi}{8} \cdot c''_{y\varphi} , & H_3^* &= \frac{\pi}{8} \cdot c'_{y\varphi} , & H_4^* &= \frac{\pi}{4} \cdot c'_{yy} \\
 A_1^* &= \frac{\pi}{8} \cdot c''_{\varphi y} , & A_2^* &= \frac{\pi}{16} \cdot c''_{\varphi\varphi} , & A_3^* &= \frac{\pi}{16} \cdot c'_{\varphi\varphi} , & A_4^* &= \frac{\pi}{8} \cdot c'_{\varphi y}
 \end{aligned}
 \tag{2.31}$$

As warned before, Scanlan's coefficients H_i^* and A_i^* are referred to the whole section width B , while Starossek's coefficients are referred to the half section width b .

In this work the semi-empirical approach of Starossek will be used in order to consider the non-stationary effects and thus improve the results of classic theory. The results will be afterwards translated to Scanlan's notation.

3 Classic theory for aeroelastic phenomena

3.1 Classic galloping theory

3.1.1 General

The main objective of the galloping theory is the determination of the onset velocity. Its forces formulation is based on the quasi-stationary force approach (section 2.1) and therefore on a linearization justified by the assumption of small oscillating amplitudes, which added to the fact that aeroelastic effects are not considered, results into a too high, not conservative value of the onset velocity.

The galloping phenomenon is important for the later understanding of the flutter phenomenon. Following the proceeding of [1], here it will be divided in two cases: bending galloping oscillations and torsion galloping oscillations.

3.1.2 Bending galloping oscillations

For the determination of the onset velocity the next simplified system, characterized by a quasi-stationary behavior, will be considered:

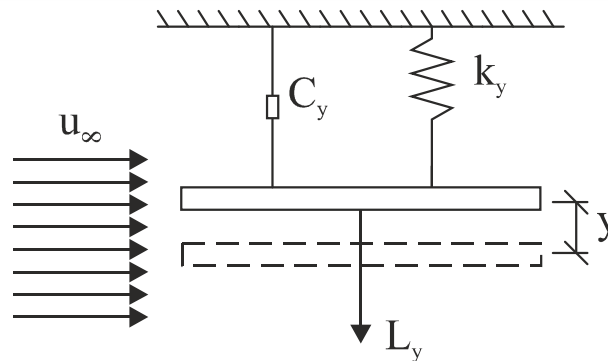


Figure 3.1: Two-dimensional object oscillating in the bending degree of freedom (vertical oscillation).

The system is composed by a simplified unitary-mass oscillator which is connected to a linear spring and to an element with damping proportional to the model's velocity. The air force is supposed to be the one corresponding to the onset velocity.

The differential equation describing the system is:

$$m \cdot \ddot{y} + C_y \cdot \dot{y} + k_y \cdot y = L_y(t) \quad (3.1)$$

The right term of equation (3.1) corresponds to the aerodynamic force $L_y(t)$ obtained through the quasi-stationary force approach, as it is shown in equation (2.18). If now only the bending degree of freedom (y) is considered, the resulting equation is:

$$m \cdot \ddot{y} + C_y \cdot \dot{y} + k_y \cdot y = q \cdot B \cdot \left(-\frac{\pi}{2} \cdot \frac{B}{u_\infty^2} \cdot \ddot{y} + \left(\frac{dC_L}{d\theta'} \Big|_{\theta'=0} + C_D(\theta' = 0) \right) \cdot \frac{-\dot{y}}{u_\infty} \right) \quad (3.2)$$

Here the term $\left(\frac{dC_L}{d\theta'} \Big|_{\theta'=0} + C_D(\theta' = 0) \right)$ can be related to that obtained in the right side of expression (1.11) in section 1.3.2, which corresponds to the derivative $\frac{d}{d\theta}$ of the coefficient C_{Fy} in the global coordinates system. This coefficient, as it was defined in section 1.3.2 (see equation (1.5)), contains the components of the wind forces that configure the aerodynamic lift $L_y(t)$, and depends on the inflow's incident angle θ . If now this angle is imposed to be $\theta = 0$, it can be seen that both coefficients $C_{Fy} \Big|_{\theta=0}$ and $C_L(t) \Big|_{\theta=0}$ are equivalent. Therefore, the derivative of C_{Fy} can be matched to that of $C_L(t) \Big|_{\theta=0}$, in which case it can be assumed:

$$\frac{dC_L}{d\theta} \Big|_{\theta=0} = \left(\frac{dC_L}{d\theta'} \Big|_{\theta'=0} + C_D(\theta' = 0) \right) \quad (3.3)$$

If now this term is moved to the left side of the equation and grouped with the other term proportional to the model's velocity, an expression analogous to (1.13) is found. This expression is composed by the sum of mechanical and aerodynamic damping. As it was explained section 1.3.2, galloping oscillations can only occur when the total damping becomes negative, which is equivalent to imposing the next condition:

$$C_y + \frac{q \cdot B}{u_\infty} \cdot \frac{dC_L}{d\theta} \Big|_{\theta=0} \leq 0, \quad \text{with } C_y = 2 \cdot m \cdot f_{e,y} \cdot \delta_{s,y} \quad (3.4)$$

This condition is equivalent to the stability condition of Glauer-Den Hartog exposed in expression (1.14).

In the limit case, when this condition is equal to 0, the onset velocity is determined by:

$$u_{on,y} = 2 \cdot f_{e,y} \cdot B \cdot \frac{Sc_{s,y}}{-\frac{dC_L}{d\theta}} \quad (3.5)$$

Where $Sc_{s,y}$ is the Scruton Number, defined as follows:

$$Sc_{s,y} = \frac{2 \cdot m \cdot \delta_{s,y}}{\rho \cdot B^2} \quad (3.6)$$

The Scruton number (or “*mass damping parameter*”) is a dimensionless parameter that indicates the structure susceptibility to galloping and is therefore a determining property for dynamic stability. Low Scruton numbers are a sign of instability, while higher numbers (due to higher masses or higher damping) mean higher stability and smaller oscillations ([3]).

3.1.3 Torsion galloping oscillations

Along the years different origins have been attributed to the appearance of torsion galloping, as the periodic alternate vortex shedding configured by the von Kármán vortex trail [19].

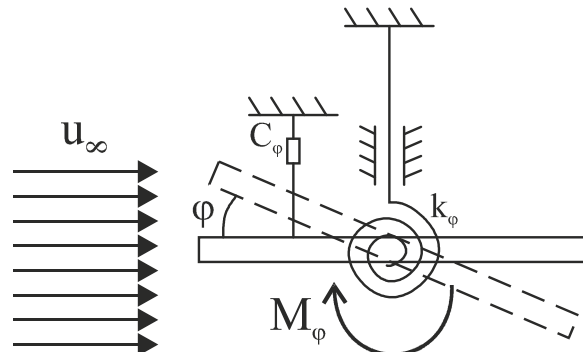


Figure 3.2: Two-dimensional object oscillating in the torsion degree of freedom (torsion oscillation).

Hortmanns ([1]) assumes that the cause of torsion oscillations is the same as that for the bending ones. Therefore torsion galloping occurs if the pressure distribution leads to a dominating moment, which causes the torsion oscillations. The differential equations for the torsion oscillations are:

$$\Theta \cdot \ddot{\varphi} + C_\varphi \cdot \dot{\varphi} + k_\varphi \cdot \varphi = M_\varphi(t) \quad (3.7)$$

If now the resulting moment of the quasi-stationary force approach exposed in equation (2.19) is introduced in the previous equation (3.7), next expression is obtained:

$$\Theta \cdot \ddot{\varphi} + C_\varphi \cdot \dot{\varphi} + k_\varphi \cdot \varphi = q \cdot B^2 \left(-\frac{\pi}{4} \cdot \frac{B^2}{16 \cdot u_\infty^2} \cdot \ddot{\varphi}(t) + \frac{dc_M}{d\theta'} \Big|_{\theta'=0} \cdot \left(\varphi + \frac{-\dot{\varphi}(t) \cdot b}{u_\infty} \right) \right) \quad (3.8)$$

If deflections are small, then $\frac{dc_M}{d\theta'} \Big|_{\theta'=0} \approx \frac{dc_M}{d\theta} \Big|_{\theta=0}$ and the condition for the starting of torsion oscillations is:

$$C_\varphi + \frac{q \cdot B^2 \cdot b}{u_\infty} \cdot \frac{dc_M}{d\theta} \Big|_{\theta=0} \leq 0, \quad \text{with } C_\varphi = 2 \cdot \Theta \cdot f_{e,\varphi} \cdot \delta_{s,\varphi} \quad (3.9)$$

As done in the previous section, the onset velocity is determined by imposing the extreme case (when condition (3.9) is equal to zero). In that case:

$$u_{0,\varphi} = 2 \cdot f_{e,\varphi} \cdot B \cdot \frac{Sc_{s,\varphi}}{-\frac{dc_M}{d\theta}} \quad (3.10)$$

where $Sc_{s,\varphi}$ is the Scruton Number:

$$Sc_{s,\varphi} = \frac{2 \cdot \Theta \cdot \delta_{s,\varphi}}{\rho \cdot b \cdot B^3} \quad (3.11)$$

3.2 Flutter

3.2.1 Generalities and physical description

Flutter theory was first developed in airplane construction. It can be described as the coupled oscillation of a system, where the movement is produced through the oscillation of two degrees of freedom that influence each other. As commented before, potential theories used for airfoils and correction functions have not led to satisfactory results when applied to bluff bodies.

This work deals with bridge sections, one of the most common bluff body cases in wind engineering. In this case the flutter phenomenon can be described as the coupled oscillation of the degrees of freedom bending and torsion caused by aerodynamic forces. The flutter frequency is therefore situated between the bending and the torsion natural frequencies ([1]). The oscillation of both degrees of freedom will only reinforce each other if the phase between them is such that the acting forces produce positive work, as next images based on [25] show.

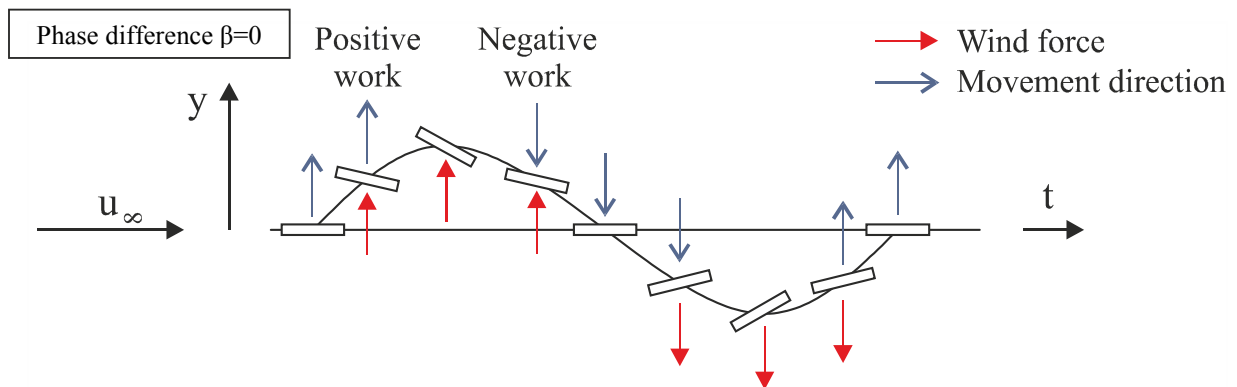


Figure 3.3: Energy balance of a wind force acting on a bluff body during coupled oscillation. Limit case for phase difference $\beta = 0^\circ$.

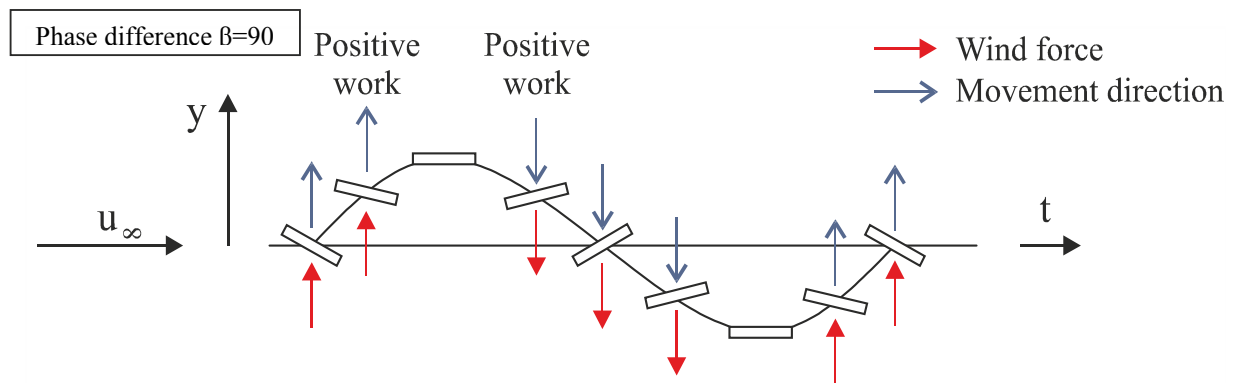


Figure 3.4: Energy balance of a wind force acting on a bluff body during coupled oscillation. Maximal force case due to uninterrupted positive work for phase difference $\beta = 90^\circ$.

As it can deduced from these figures, if the phase difference is $\beta=90^\circ$ the work is positive for the entire oscillation period, which leads to a maximal fanning force. The flutter will occur if this total work is higher than the work done by the damping forces. In classic flutter theory the considered phase difference is $\beta=0^\circ$, thus in this case the energy balance is already equal to zero.

The susceptibility to vibration of a structure depends mostly on three factors: the profile geometry, the decreasing natural frequency as a result of the increasing slenderness in bridge constructions and the low structural damping as a result of filigree constructions, which is specially critic in welded constructions.

3.2.2 Movement equations and calculation of the onset velocity

Figure 3.5 represents a two-dimensional system with acting forces L_y and M_ϕ .

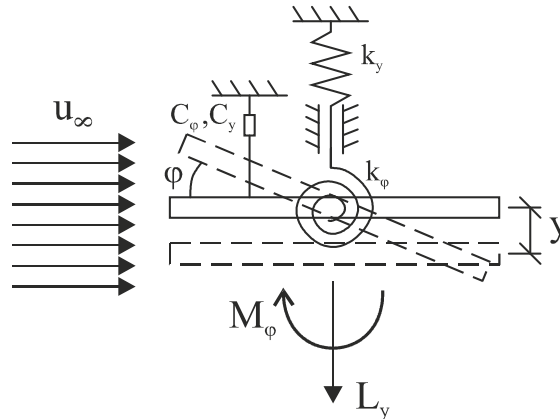


Figure 3.5: Two-dimensional object oscillating in both bending and torsion degrees of freedom.

For a phase angle between bending and torsion of $\beta = 0$, the movement equations are:

$$m \cdot \ddot{y} + C_y \cdot \dot{y} + k_y \cdot y = L_y(t) \quad (3.12)$$

$$\theta \cdot \ddot{\varphi} + C_\varphi \cdot \dot{\varphi} + k_\varphi \cdot \varphi = M_\varphi(t) \quad (3.13)$$

Both equations can be expressed in a more compact way using the matrix form:

$$M \cdot \ddot{r} + C \cdot \dot{r} + K \cdot r = F_L \quad (3.14)$$

With:

$$M := \begin{pmatrix} m & 0 \\ 0 & \theta \end{pmatrix} \quad \text{Mass matrix}$$

$$C := \begin{pmatrix} C_y & 0 \\ 0 & C_\varphi \end{pmatrix} \quad \text{Damping matrix}$$

$$K := \begin{pmatrix} k_y & 0 \\ 0 & k_\varphi \end{pmatrix} \quad \text{Stiffness/ Spring matrix} \quad (3.15)$$

$$r = \begin{pmatrix} y \\ \varphi \end{pmatrix} \quad \text{Displacements vector}$$

$$F_L := \begin{pmatrix} L_y \\ M_\varphi \end{pmatrix} \quad \text{Forces vector according to Starossek's approach}$$

It can be seen from these equations that the coupling between both degrees of freedom happens only through the forces vector. In the flutter case, bending and torsion frequencies are considered to be equal to the flutter frequency ($\omega_y = \omega_\varphi = \omega_F$). Besides, the phase displacement between the degrees of freedom y and φ in the flutter initialization moment is 0, which makes the consideration of the phase angle β unnecessary.

The displacement vector will be taken analogously to the one in expression (2.27):

$$\mathbf{r} := \vec{r}_0 \cdot e^{i\omega_F t}, \quad \text{with} \quad \vec{r}_0 := \begin{pmatrix} y_0 \\ \varphi_0 \end{pmatrix} \quad (3.16)$$

If the time derivatives are calculated as in expression (2.28) and the results are introduced in (3.14), the next system of differential equations is obtained:

$$-M \cdot \omega_F^2 \cdot \vec{r}_0 + i \cdot C \cdot \omega_F \cdot \vec{r}_0 + K \cdot \vec{r}_0 - F_L^* = 0 \quad (3.17)$$

With:

$$F_L^* := \pi \cdot \rho \cdot b^2 \cdot \omega_F^2 \cdot \begin{pmatrix} c'_{yy} + i \cdot c''_{yy} & b \cdot (c'_{y\varphi} + i \cdot c''_{y\varphi}) \\ b \cdot (c'_{\varphi y} + i \cdot c''_{\varphi y}) & b^2 \cdot (c'_{\varphi\varphi} + i \cdot c''_{\varphi\varphi}) \end{pmatrix} \cdot \vec{r}_0 \quad (3.18)$$

According to [1] (even though an analogous derivation can be found in [2]), the solution to this equation can be divided in real and imaginary parts:

Real part:

$$\begin{aligned} & \lambda_F^4 \cdot \left(1 + \frac{\rho \cdot B^4}{\theta} \cdot A_3^* - \frac{\rho^2 \cdot B^6}{m \cdot \theta} \cdot H_1^* \cdot A_2^* + \frac{\rho \cdot B^2}{m} \cdot H_4^* + \frac{\rho^2 \cdot B^6}{m \cdot \theta} \cdot H_4^* \cdot A_3^* \right. \\ & \quad \left. + \frac{\rho^2 \cdot B^6}{m \cdot \theta} \cdot (H_2^* \cdot A_1^* - H_3^* \cdot A_4^*) \right) \\ & \quad + \lambda_F^3 \cdot \left(2 \cdot \xi_y \cdot \frac{\rho \cdot B^4}{\theta} \cdot A_2^* + 2 \cdot \xi_\varphi \cdot \frac{\rho \cdot B^2}{m} \cdot H_1^* \cdot \frac{\omega_\varphi}{\omega_y} \right) \\ & \quad + \lambda_F^2 \cdot \left(- \left(\frac{\omega_\varphi}{\omega_y} \right)^2 - 4 \cdot \xi_y \cdot \xi_\varphi \cdot \frac{\omega_\varphi}{\omega_y} - 1 - \frac{\rho \cdot B^4}{\theta} \cdot A_3^* - \frac{\rho \cdot B^2}{m} \cdot H_4^* \cdot \left(\frac{\omega_\varphi}{\omega_y} \right)^2 \right) \\ & \quad + \lambda_F(0) + \left(\frac{\omega_\varphi}{\omega_y} \right)^2 = 0 \end{aligned} \quad (3.19)$$

Imaginary part:

$$\begin{aligned}
 & \lambda_F^3 \cdot \left(\frac{\rho \cdot B^4}{\theta} \cdot A_2^* + \frac{\rho^2 \cdot B^6}{m \cdot \theta} \cdot H_1^* \cdot A_3^* + \frac{\rho \cdot B^2}{m} \cdot H_1^* \right) \\
 & + \frac{\rho^2 \cdot B^6}{m \cdot \theta} \cdot (H_4^* \cdot A_2^* - H_2^* \cdot A_4^* - H_3^* \cdot A_1^*) \\
 & + \lambda_F^2 \cdot \left(-2 \cdot \xi_\varphi \cdot \frac{\omega_\varphi}{\omega_y} - 2 \cdot \xi_y - 2 \cdot \xi_y \cdot \frac{\rho \cdot B^4}{\theta} \cdot A_3^* \right) \\
 & \quad - 2 \cdot \xi_\varphi \cdot \frac{\rho \cdot B^2}{m} \cdot H_4^* \cdot \frac{\omega_\varphi}{\omega_y} \\
 & + \lambda_F \cdot \left(-\frac{\rho \cdot B^4}{\theta} \cdot A_2^* - \frac{\rho \cdot B^2}{m} \cdot H_1^* \cdot \left(\frac{\omega_\varphi}{\omega_y} \right)^2 \right) \\
 & + 2 \cdot \xi_y \cdot \left(\frac{\omega_\varphi}{\omega_y} \right)^2 + 2 \cdot \xi_\varphi \cdot \frac{\omega_\varphi}{\omega_y} = 0
 \end{aligned} \tag{3.20}$$

Where ξ_y and ξ_φ are respectively the bending and the torsion damping ratios and the variable λ_F is defined as follows:

$$\lambda_F = \frac{\omega_F}{\omega_Y} \tag{3.21}$$

Flutter will occur if both equations are equal to zero at the same time and having the same value of λ_F . As the non-stationary coefficients A_i^*, H_i^* depend on the reduced velocity u_{red} , the solution will be found as the first case in which both equations are equal to 0 during their calculation for different values of u_{red} . This means that the flutter solution must be found calculating the solution of the equations (3.19) and (3.20) iteratively for different values of the reduced velocity. At the point where the solution curves of the real part and the imaginary part cut each other, both conditions are fulfilled at the same time. The flutter onset velocity can be calculated using the reduced velocity that leads to the cutting of both curves. The flutter frequency will then be calculated as $\omega_F = \lambda_F \cdot \omega_Y$.

4 Measurement of non-stationary, aeroelastic coefficients

4.1 Introduction

Section 4 is aimed to explain the most important methods, factors and parameters that must be considered when measuring the aerodynamic coefficients. It is divided in three parts: the first part justifies the measuring method choice after describing the characteristics of some of them. The second part describes some of the elements used to measure the aerodynamic coefficients. Finally, the third part exposes and comments some of the parameters and previous processes that must be set and carried out in order to optimize each measuring event.

4.2 Measuring methods

4.2.1 Free Oscillation Method (Decrement method)

In the free oscillation method the model is suspended through two springs, initially deviated and left afterwards in a free oscillation state. During this decreasing oscillation (in which a frequencies also get lower, as shown in Figure 4.1) the frequency and the damping will be evaluated and used together with the equations of movement (3.12) and (3.13) to determine the four direct coefficients contained in expressions (2.24) and (2.25) that describe the aerodynamic excitation force during an uncoupled oscillation ([1]).

To determine the other four coefficients – the indirect coefficients – the model should be exposed to velocities over the onset velocity, which provokes the apparition of coupled oscillations that allow the evaluation of the phase and the amplitude relations.

However, this evaluation is generally difficult in regard to technical and numerical terms. Besides, the determination of the indirect coefficients requires the characteristic curves of the direct coefficients, which implies that mistakes done during the direct coefficients determination will be spread to the indirect ones.

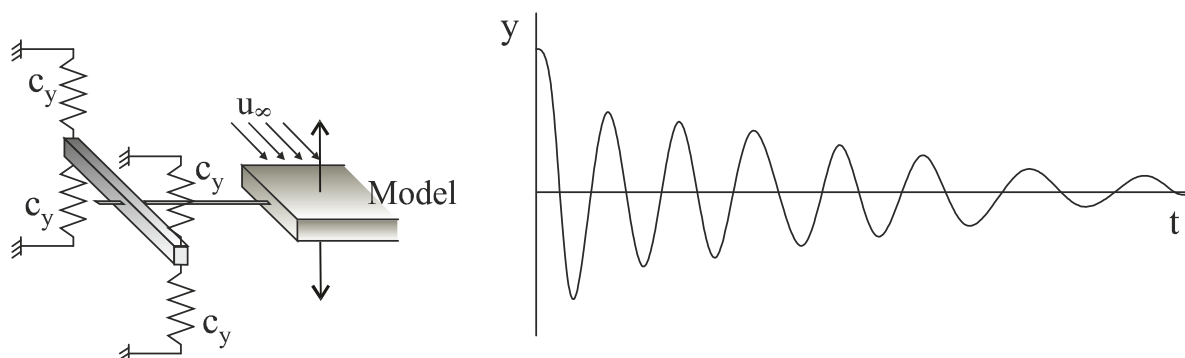


Figure 4.1: Equivalent system in Free Oscillation Method and representation of model's movement with decreasing oscillation amplitude and frequency.

4.2.2 Forced Oscillation Method (Direct measure of the flow forces)

In this method the model is excited with harmonic, constant amplitude oscillations vertically or around the central axis. The reaction forces are determined after the inertial forces are subtracted from the measured values. These inertial forces can be determined through acceleration measurements in the model. The difference between reaction and inertial forces corresponds to the flow forces. The lifting force and the moment of the air forces will be parallel measured; therefore the coupled vibration tests become unnecessary.

In a general case, non-stationary air forces act stochastically, which makes necessary that their evaluation is done in the frequency domain. Therefore a Fourier analysis will be carried out.

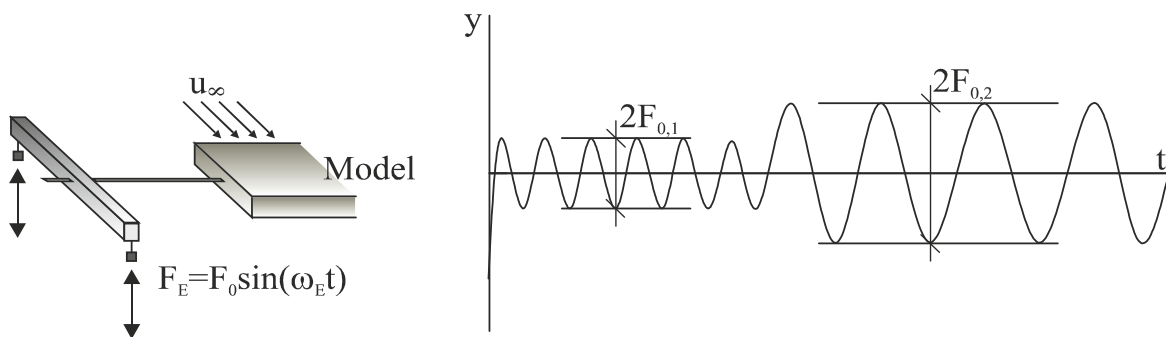


Figure 4.2: Equivalent system in Forced Oscillation Method and representation of model's movement with two different oscillation amplitudes and constant frequency.

4.2.3 Phase Resonance Method

This method mixes both two last methods; the model is suspended from two springs but also subjected to a forced excitation. The excitation frequency acts on one degree of freedom and is varied until the phase angle between exciting force and movement is equal to 90° , which leads to resonance. In this case the exciting force corresponds to the damping force.

If the force acts in the two degrees of freedom (coupled oscillation) the steady, stationary case will be measured and the coefficients will be determined using the equations of movement (3.12) and (3.13).

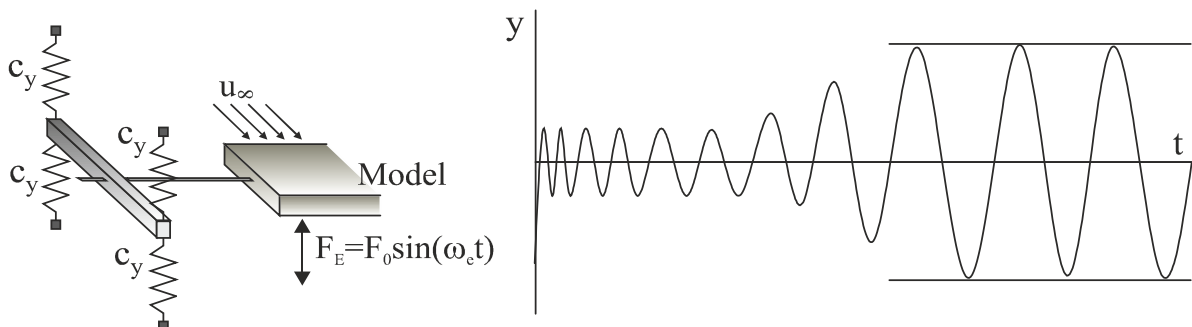


Figure 4.3: Equivalent system in Phase Resonance Method and conceptual representation of model's movement.

4.2.4 Chosen method

The chosen method should be able to measure the dependent behavior of the amplitude and give accurate enough results. The decrement method is not recommendable for the measuring of the amplitude behavior due to the lack of stationary harmonic oscillations. The phase resonance method is optimum for the determination of the direct coefficients, but involves serious difficulties while determining the indirect ones (see [1]). The forced oscillation method offers advantages like the accurate control of the oscillation amplitude and frequency, the constant coincidence between center of masses and center of rotation (see section 2.1.3b), and the relative facility of reproducing stationary harmonic oscillations.

In conclusion, the forced oscillation method prevails over the other methods as the most accurate and effective measuring method, and will therefore be the method used in this work.

4.3 Experiment set-up

4.3.1 Wind Tunnel

The wind tunnel is an essential element of the simulation, as it will provide the approximately constant, desired undisturbed wind velocity for each measurement. In the tests of this work the wind tunnel of the chair for structural steel engineering of the RWTH Aachen university (*“Institute of steel construction - RWTH Aachen”*) will be used. Figure 4.1.4 shows the appearance of this wind tunnel.

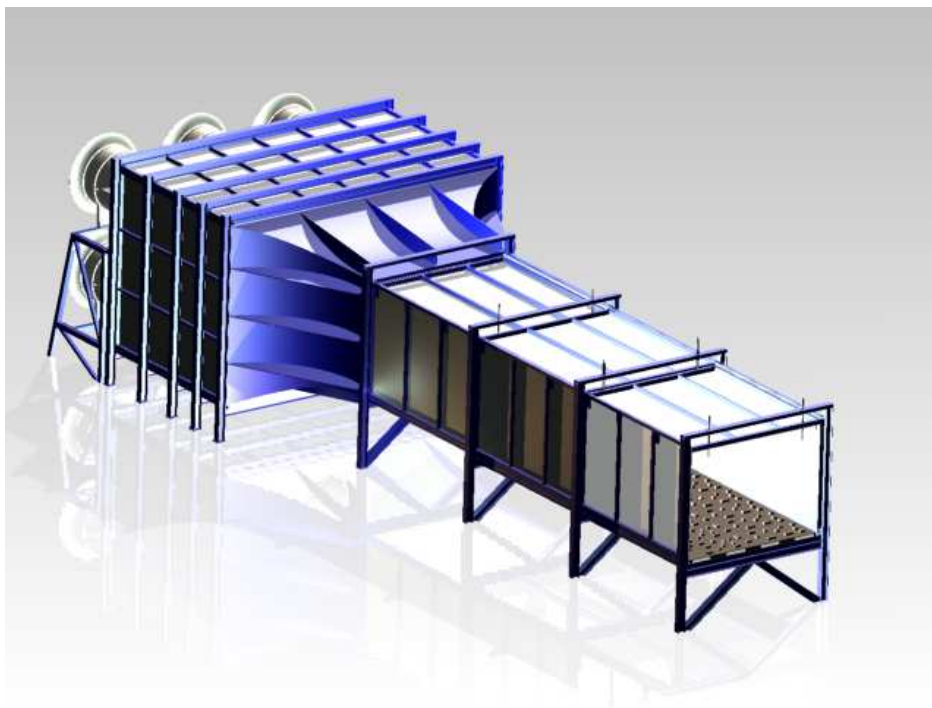


Figure 4.4: 3D model of the wind tunnel of the *“Institute of steel construction - RWTH Aachen”*

The cross-section is 2.5 m wide and 1.7 m high. The maximum reachable wind velocity has an approximate value of 30 m/s. The turbulence intensity is variable, and can be changed through the disposition of roughness elements inside the tunnel section. Without these elements the turbulence grade achieves a minimum value of $I_u = \sigma/u_m \approx 7\%$, where u_m is the average flow velocity. In this work the measurements will be done with this turbulence grade.

4.3.2 Test rig

The test rig consists of two trestles constructed and united through square hollow profiles, over which all the other elements are placed.

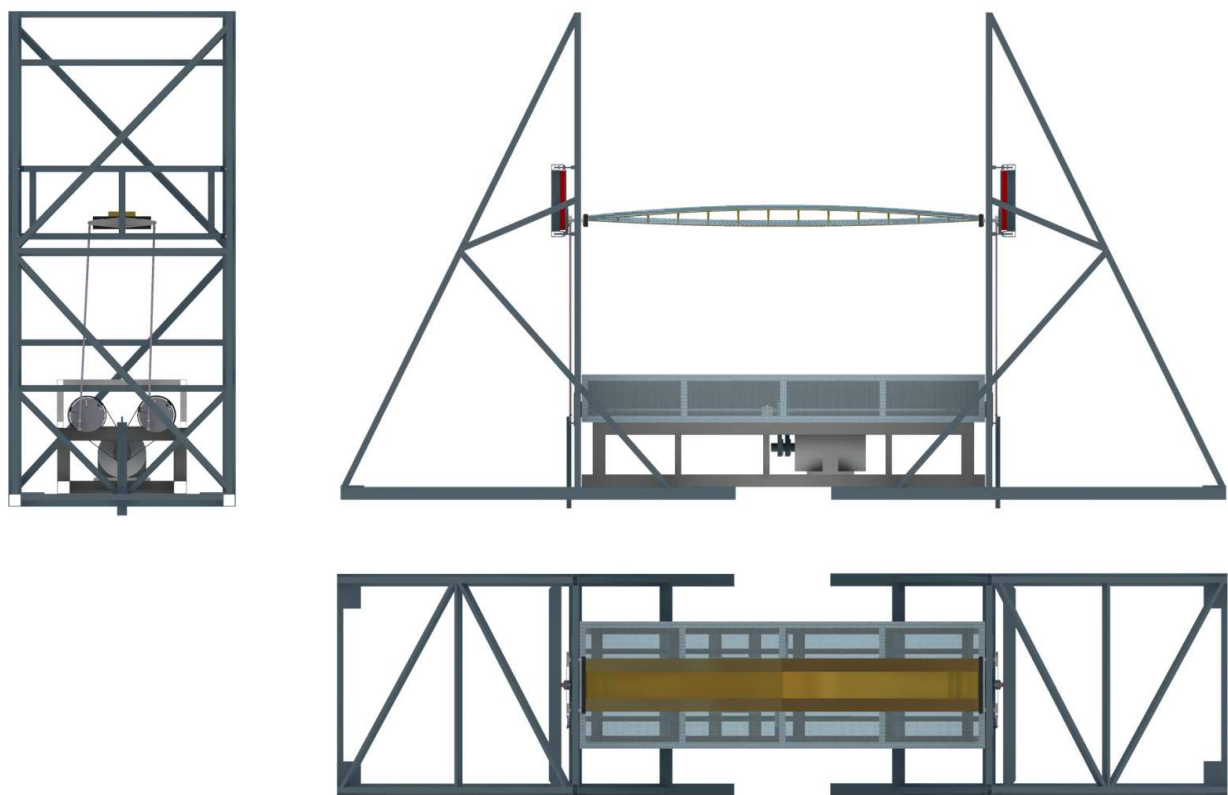


Figure 4.5: Cross-section, elevation and plan of the test rig.

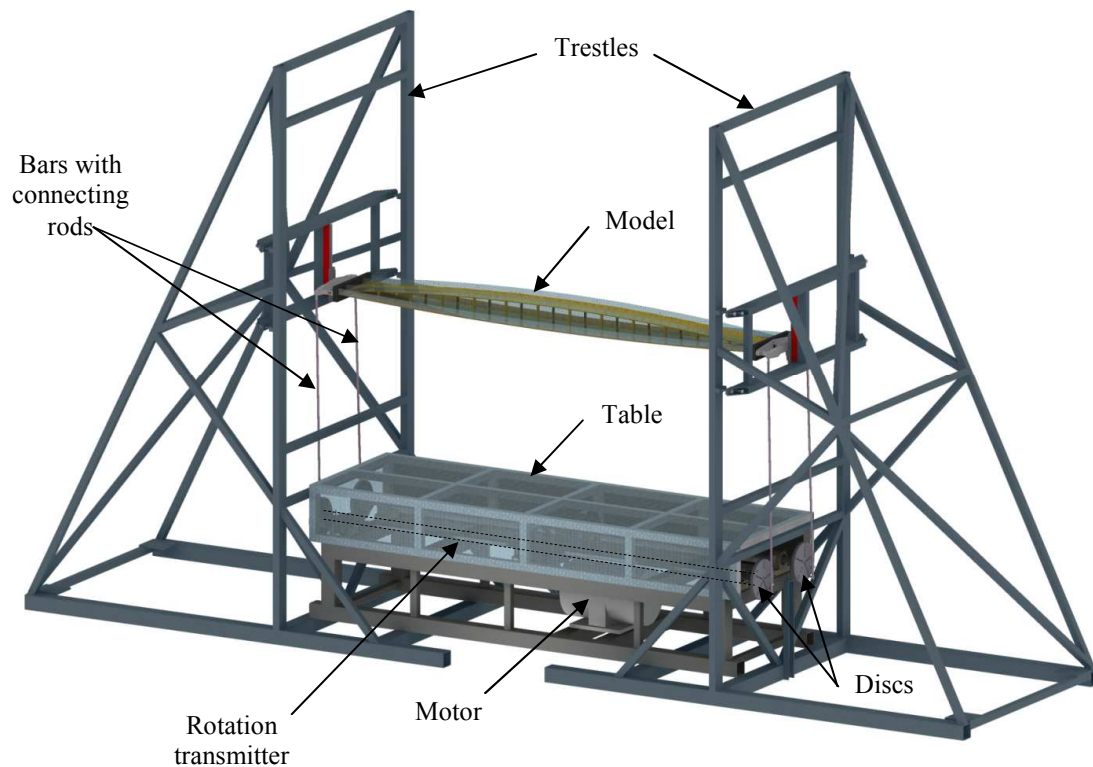


Figure 4.6: Overall sight of the test rig.

Figure 4.6 allows an overall visualization of the test rig. As it can be seen, the trestles act as a support for the table, which contains the motor and horizontal metallic bars that act as rotation transmitters and contain discs at their extremes (see Figure 4.7). These rotation transmitters are connected to the motor through cogged belts (see Figure 11.1 and Figure 11.2), which transfer the rotation of the motor to the bars and, as a result, to the discs and to the connecting rods. The rods are connected to the discs at the end of the rotation transmitters, and contain the force transducers close to their lower extreme. Each disc contains 5 radial rows of holes to enable different oscillation amplitudes during the tests. The connecting rods, the force transducers and the discs are shown in Figure 4.7.

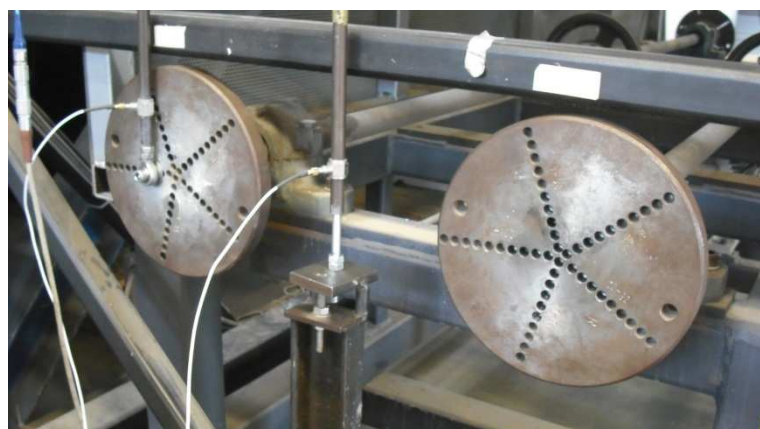


Figure 4.7: Metallic discs at the end of the rotation transmitters.

Figure 4.8 shows in higher detail the connection between model and test rig. The upper connecting rods are connected to the bridge holders, which have a double function: on the one hand, they hold the bridge and enable its disposition in different angles so that different wind attack angles can be simulated in the tests. On the other hand, they are also connected to a vertical guide, which works in two different ways; in the across-wind galloping tests (or bending galloping tests) it keeps the bridge model oscillating in a vertical direction, preventing the appearance of horizontal movements. It moves therefore up and down in harmony with the bridge model. In the torsion galloping tests it is connected to a central bar with a connecting rod in the upper extreme, which allows torsion movements preventing any vertical and horizontal movement. Although they are not shown in the figures for visibility reasons, there are plastic plates between the model extremes and the trestles in order to avoid flow perturbations (see Figure 11.5).

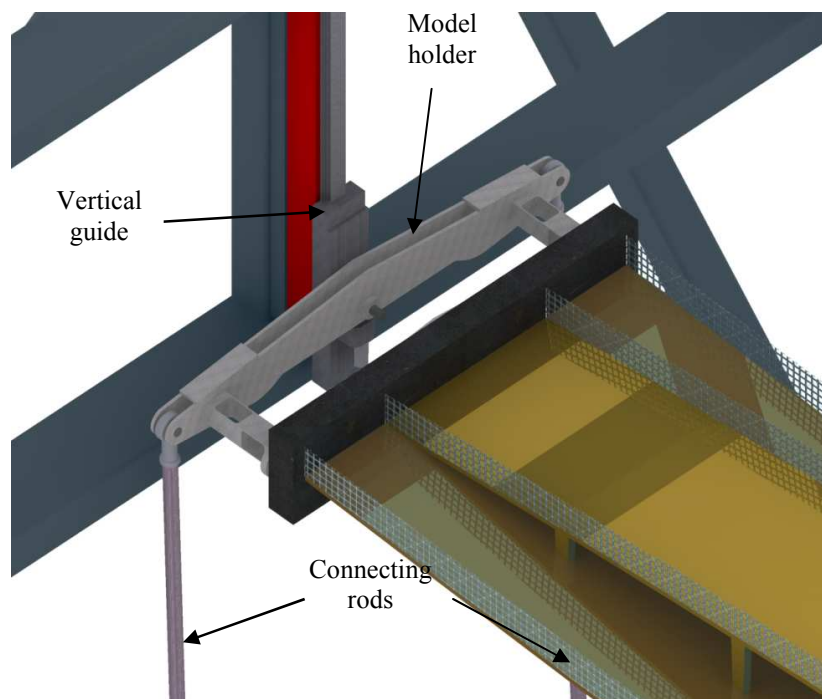


Figure 4.8: Sight of the connection of the model with the test rig.

Finally, the model is connected to the bridge holder through a set of different screws, which allow different inclinations of the bridge model for different tests.

The test rig is, in general, made of steel. Therefore it possesses a high self-weight and standing capacity, allowing measurements with a model oscillation frequency of 40 Hz. The model and structures above the connecting rods (with the latter included) are however relatively light: actually, the weight of the model should be minimized as much as the minimal required resistance allows. This is due to the necessity of minimizing inertial forces which could distort the measurement results. These inertial forces will be anyway first measured in zero-wind conditions and then subtracted from the measurements with wind.

Annex 11.4 contains several photos of the actual test rig.

4.3.3 Force Sensors

The sensors used to measure the forces produced during the tests are the force sensors 208C02 of the brand PCB.

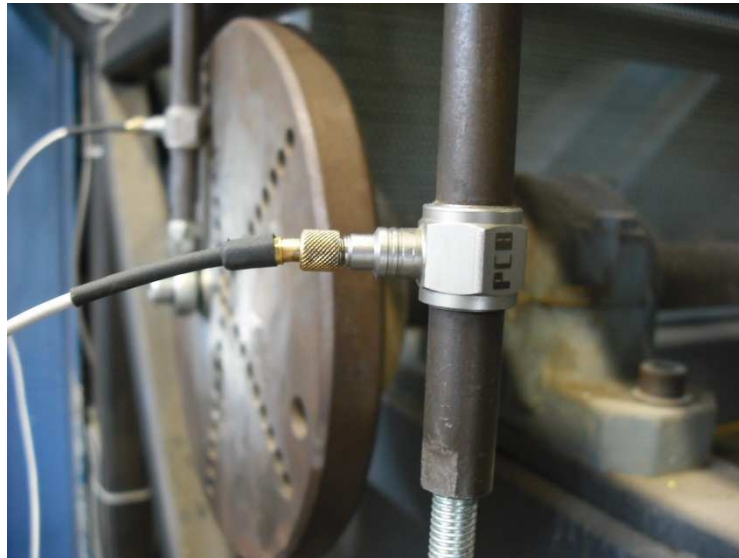


Figure 4.9: Force sensors in connecting rods during a torsion test.

They measure exclusively dynamic forces and their characteristics can be resumed as follows:

Model 208C02

Multi-purpose, ICP® force sensor, 100 lb comp., 100 lb tension, 50 mV/lb

- Measurement Range: (Compression) 100 lb (0.4448 kN)
- Sensitivity: ($\pm 15\%$) 50 mV/lb (11241 mV/kN)
- Low Frequency Response: (-5%) 0.001 Hz
- Upper Frequency Limit: 36000 Hz
- Temperature Range: -65 to +250 °F (-54 to +121 °C)
- Mounting Thread: 10-32 Female (Not Applicable)

More information about the force sensors can be found in the company website ([30]) and in the annex 11.3.

4.3.4 Bridge model

The tested bridge model is a scale model of the Simone-de-Beauvoir footbridge in Paris (see Figure 4.10).



Figure 4.10: Simone-de-Beauvoir footbridge in Bercy, Paris.

The model scale parameter is 1:36,5 , which makes the geometry in middle section to have a width of 328 mm (12 meters in reality) and a deck height of 109,5 mm (4 meters in reality). The mass of the model is 21.77 kg.

Due to construction reasons and given the fact that the study will be focused in the middle section of the bridge, the model is only constructed between the sections in which the superior and the inferior deck find each other.

The model is not perfectly stiff, which will be considered in the upcoming analysis by measuring the different accelerations measured in the middle section and in one of the extreme sections.



Figure 4.11: Photo of the model used in the tests

4.4 Measurement parameters

4.4.1 Preparation of the measurement events

Previously to each measuring event, all possible interferences and unwanted effects of the boundary conditions and the test environment should be avoided.

On the one hand, all cables connecting the force sensors and the accelerometers were attached to their closest parts of the trestles of test rig. This way some vibration and loads due to cable oscillation are considerably reduced.

On the other hand, the motor was turned on and the excitation mechanism activated between 30 and 45 minutes before the measurements started. This procedure is aimed to achieve a constant damping value during the measurements, as the warming of the excitation mechanism involves a reduction of the damping during the first minutes.

4.4.2 Determination of the air density

Before starting any series of experiments the air density must be determined, as it affects linearly to the results. Through temperature and air pressure differences the results can vary approximately 20% ([1]). For this reason the air density must be determined at the beginning of each experiment through de measurement of the air pressure and the use of the ideal gas law:

$$\rho = \frac{P}{R \cdot T} \quad (4.1)$$

Where: ρ = Air density [kg/m³]

R = Gas Constant = 287 [Nm/kgK]

T = Temperature [K]

P = Air pressure [Pa]

4.4.3 Excitation frequency and oscillation amplitude

While the dispersion in the measurement of the structural forces stays constant or even gets smaller for higher excitation frequencies, the aeroelastic forces grow to the power of two with the excitation frequency. Therefore, and considering that the structural forces should be determined before the aeroelastic forces, it is common to use only one excitation frequency for a whole series of experiments to save time. This frequency is usually chosen depending on several factors such as the stability and the mass of the model, the fixed excitation amplitude and the wanted reduced wind velocity. The latter will change along the tests by changing the inflow velocity.

4.4.4 Number of measurement values

In order to determine the number of measurement values, three parameters can be used: the sample rate, the number of values and the measuring time. Only two of them must be fixed to determine a measuring event (the third one is always dependent of the other two). Those parameters should be chosen in accordance with time reasons, computational costs and experience factors.

5 Processing of measured non-stationary, aeroelastic coefficients

5.1 Introduction

Section 5 is aimed to explain all the steps that lead from the just measured, not treated data to the aerodynamic coefficients. Therefore two main sections can be distinguished. The first one (section 5.2) corresponds to the correction algorithms, and contains some of the aspects relative to test inaccuracies and signal distortion that must be corrected before or during the calculation of the coefficients calculation. The second one (section 5.3) deals with the filtering of the signal and some of the filter characteristics that must be considered before choosing the filter characteristics.

5.2 Needed correction algorithms

Before starting the calculation algorithm that leads to the aerodynamic coefficients, the imperfections and distortions inherent to the measuring process should be considered. This does not only concern the distortions originated by technical and friction aspects, but also those design and physic aspects which cannot exactly match the ideal test design and execution.

In the next section three of the most important aspects are considered and briefly explained. Commentaries about their influence on the results and about their correction will be done in this section. The moment to use them will be mentioned in the sections in which these corrections are necessary.

5.2.1 Tilting of the connecting rods

As exposed on section 4.3.2, the force transducers are located in the lower part of the connecting rods. In an ideal case, these connecting rods would excite the model with a perfect vertical oscillatory movement and would therefore only measure forces with a vertical direction. However, in the test rig they have a different attack angle during the model's oscillation due to the way they are connected to the discs, which implies that more forces than the strictly vertical will be measured. This fact, though negligible in the bending tests, has a relatively high relevance in torsion oscillations.

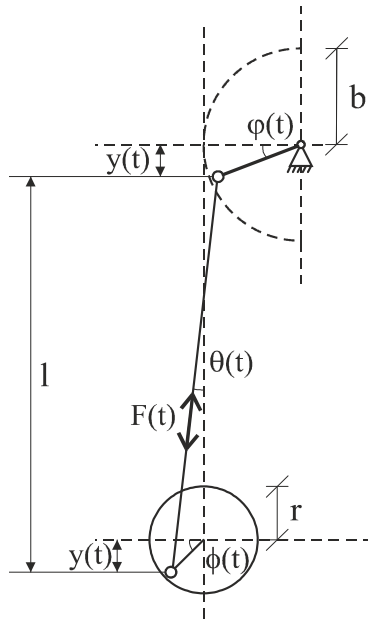


Figure 5.1: Geometrical relations in the experiment set-up.

As said previously, the wanted values are those corresponding to the vertical component of the measured forces.

Vertical reaction force:

$$R(t) = F(t) \cdot \cos(\theta(t)) \quad (5.1)$$

Relation between $\varphi(t)$ and $\phi(t)$:

$$\begin{aligned} y(t) &= r \cdot \sin(\phi(t)) \\ y(t) &= b \cdot \sin(\varphi(t)) \end{aligned} \quad (5.2)$$

$$\rightarrow r \cdot \sin(\phi(t)) = b \cdot \sin(\varphi(t))$$

Relation with $\theta(t)$:

$$\tan(\theta(t)) = \frac{r \cdot \cos(\phi(t)) + b \cdot (1 - \cos(\varphi(t)))}{l} \quad (5.3)$$

The tilting of the connecting rods does not change the amplitude of the inertial forces because the rods are in a vertical position when the maximal force is given. However, the tilting produces an increment of the damping forces and also an increment of the values of the signal close to the peak values. This leads to higher values of the measured force, which may have to be corrected through an integration of the power spectrum.

However, this effect was proven to be negligible by Hortmanns [1] in the bending tests, though it plays a role in the torsion ones.

5.2.2 Dynamic bending line

The fact that the bridge model is not absolutely stiff leads to its curvature during the forced oscillations, which implies that the acceleration values in the middle of the model are higher than those in the extremes.

To consider this additional deviation Hortmanns [1] carried out several experiments with different excitation frequencies and amplitudes, measuring in several points along the length of the model to determine the dynamic bending line. He calculated then the integral of the normalized dynamic bending line and compared it to the normalized integral obtained from a simply supported, single span beam with constant bending stiffness and under the action of a uniform distributed load p , which leads to a value of 0.64. As the difference between the experimental and the theoretical results was proven to be negligible, the theoretical, constant value 0.64 will be used during the measured data evaluation.

This value is obtained from the next operations:

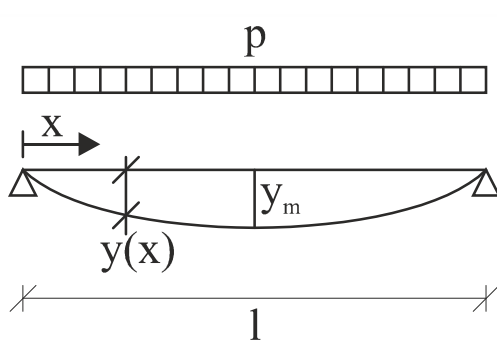


Figure 5.2: Simply supported beam under uniform distributed load p

$$y(x) = \frac{1 + \frac{x(l-x)}{l^2}}{24EI} \cdot \frac{x(l-x)}{l^2} \cdot q \cdot l^4 \quad (5.4)$$

$$y_m = \frac{5pl^4}{384EI} \quad (5.5)$$

$$\frac{\int_0^l y(x) dx}{y_m \cdot l} = \frac{\frac{p \cdot l^5}{120EI}}{\frac{5pl^5}{384EI}} = 0,64 \quad (5.6)$$

In the torsion case the magnitude of this dynamic effect depends on the section and torsional stiffness. For example, Hortmanns ([1]) proved in the models he used that this effect could be ignored because of its negligible effect on the results.

However, the model used in this case and, in general, any other used model may present lower torsion stiffness than those used by Hortmanns, and therefore this effect may be not negligible. A hypothesis will be made in this work in order to consider this effect.

Here it will be assumed, analogously to the bending case, that the normalized dynamic torsion line approximately equals the normalized integral obtained from a single span beam with constant torsion stiffness, which is under the action of a constant torsion moment m_t and supported in a way that twisting in its straight sections is allowed. In these conditions, the beam will be in a state of pure uniform torsion or Saint-Venant's torsion, in which case necessary values can be calculated as follows:

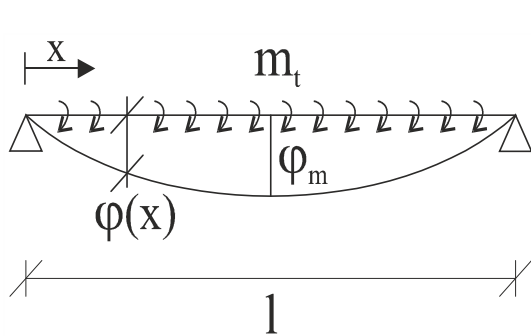


Figure 5.3: Beam in a Saint-Venant's torsion state under uniform moment m_t

$$\varphi(x) = \frac{1}{GI_t} \cdot \int_0^x \left(\frac{m_t \cdot L}{2} - m_t \cdot x \right) dx \quad (5.7)$$

$$\varphi_m = \frac{m_t l^2}{8GI_t} \quad (5.8)$$

$$\frac{\int_0^l \varphi(x) dx}{\varphi_m \cdot l} = \frac{\frac{m_t l^3}{12GI_t}}{\frac{m_t l^3}{8GI_t}} = 0,67 \quad (5.9)$$

As it can be seen in expression (5.9), the obtained result does not differ much from the one obtained in the bending case. This hypothesis will not be tested in the test rig due to lack of time and resources. However, the order of magnitude of the effect must be similar to the one

acquired with this hypothesis, and in both cases the influence of the additional deflection in the results is not critical.

In conclusion, both additional deviations in middle section (in bending and torsion tests) will be calculated and compared with those at extreme sections, and an adequate correction method will be used in order to consider them.

5.2.3 Phase displacement between sensors

As the essential part of the measured data is processed in the frequency domain, the phase angle between the different magnitudes and measurements has to be precisely calculated. Therefore the phase difference between the sensors should be studied and, if necessary, determined and corrected through an appropriate algorithm.

With that objective each of the 4 force transducers can be placed over the accelerometers in the model with a small additional mass. The measured acceleration and force values should have an exact phase difference of 180° .

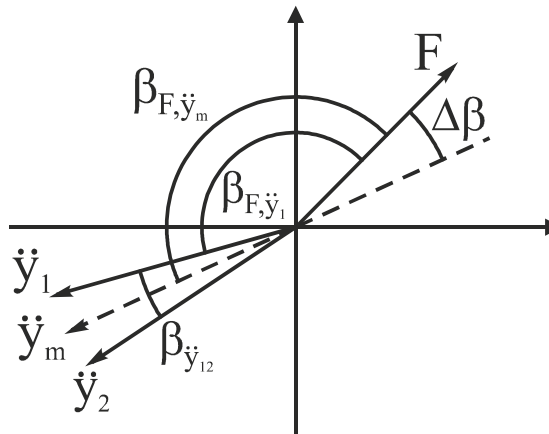


Figure 5.4: Phase difference between the different sensors

Using Figure 5.4 as a reference, it can be seen that the angle correction $\Delta\beta$ necessary to fulfill the 180° condition is:

$$\Delta\beta = 180^\circ - \beta_{F, \ddot{y}_m} = 180^\circ - \beta_{F, \ddot{y}_1} + \frac{1}{2}\beta_{\ddot{y}_1, \ddot{y}_2} \quad (5.10)$$

In this work the phase displacement between sensors was assumed to be negligible, as the observed peaks of the 4 measured forces presented in most cases a relative phase difference not bigger than 0.005 seconds. Further investigation about this phenomenon was not carried out.

5.3 Filtering the measured data

While measuring forces and accelerations it is unavoidable to also measure noise and distortion due to the measuring process and to the friction and vibrations proceeding from the test rig mechanisms. Therefore the measured data does not look like a clean sinusoidal signal, although a strong tendency to this type of signal can be appreciated.

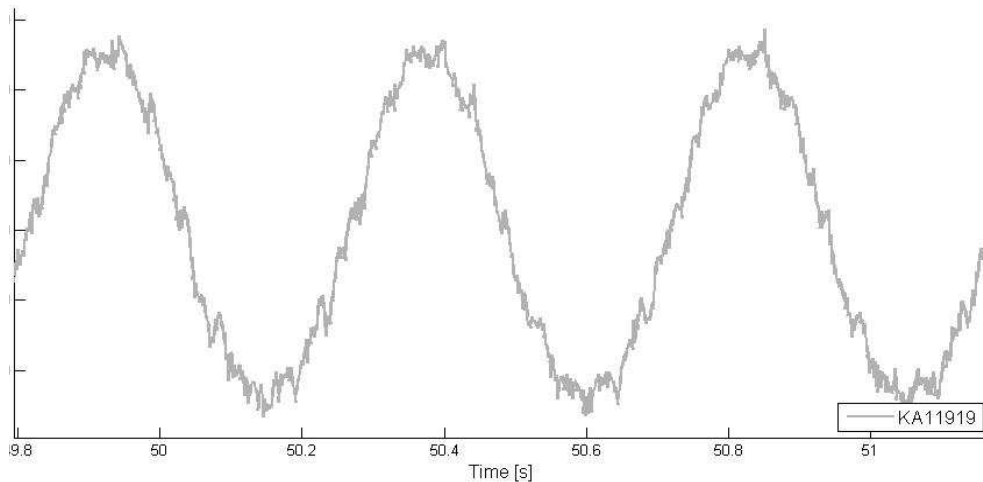


Figure 5.5: Example of measured signal before filtering

As the data analysis will be based on spectral density functions, the input signals should be barely contaminated with noise in order to obtain optimal results. Therefore all measured data will be filtered in order to remove noise components and harmonic multiples of the excitation frequency from the spectral density functions. This way the only relevant peak that will remain in these functions will be that corresponding to the excitation frequency.

Two possible types of filters were considered to process the data:

- **Low-pass filter:** the low-pass filter allows removing the information of all frequencies above the chosen one, which in this case is the excitation frequency. Given the fact that the excitation frequencies are relatively small compared to the frequencies of noises and harmonics, this filter type can be used here with the wanted results. The lack of control at frequencies lower than the excitation one can be compensated by integrating the spectral functions only in a small domain around the peak that corresponds to the excitation frequency. However the length of this domain is not constant and must therefore be chosen imposing a tolerance value, which makes the domain length depend on certain subjectivity. This can lead to a loss of information during the integration, which leaves the low-pass filter in an unfavorable position versus the second type of filter considered, the band-pass filter.
- **Band-pass filter:** the band-pass filter allows removing information of all the frequencies except those close to the chosen one, which in this case is again the excitation frequency. This makes it especially useful, as after filtering there is certainty that only the phenomena linked to the chosen frequency will be represented in the signal. This fact implies that the spectral functions can be integrated over the whole frequency domain, as all frequencies different from the excitation frequency

will present a zero contribution to the spectra and, consequently, to the integral result. In conclusion, the band-pass filter becomes the best choice to filter the measured signals.

Both filters present an unstable zone at their beginning. The magnitude and length of this zone can be diminished by reducing the steepness of the filter slope from passband to stopband, which means using a filter with a smaller order that can still suppress effectively the information of unwanted frequencies. The values of the unstable zone will be removed before the processing of the signal.

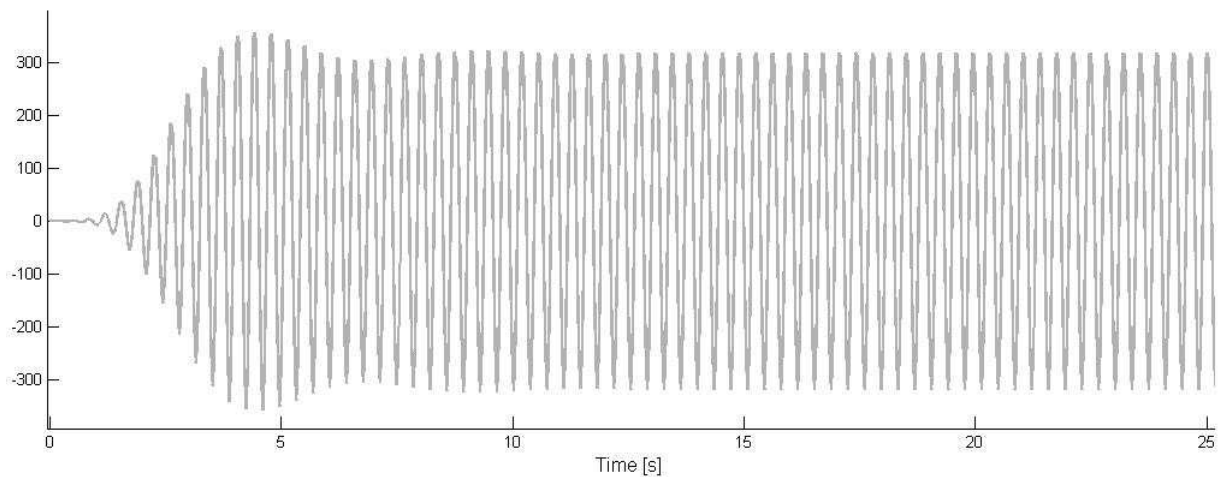


Figure 5.6: Unstable zone of a measured signal after applying a band-pass filter of order 10.

Some filtering processes can provoke a phase displacement between the original signal and the filtered one. This phase difference, which depends on frequency interval and slope of the transition between stopband and passband among other factors, would not become a problem as the same filter would be used for all the signals sharing an excitation frequency. This way all signals would be affected by the same phase displacement configuration, which would keep the relative phase between them unaffected.

However, in this work a zero-phase digital filter will be used in order to avoid any phase displacement that could contaminate the spectral functions.

6 Calculation algorithms for the non-stationary, aeroelastic coefficients

6.1 Introduction to the used spectral analysis concepts

This section deals briefly with some concepts of spectral analysis theory that are used to calculate the aerodynamic coefficients (see section 6.2). The notation used in this section is therefore functional and not significant for the rest of the work.

These concepts consist mainly on properties of the cross power spectral density (CPSD). The CPSD is a complex function. It has a real part that shows how the power of the two signals is distributed along frequency, and an imaginary part that contains phase information. As the signals measured in the tests are composed by discrete values, the expressions below will also be written in its discrete form.

The CPSD of two signals is calculated by applying the Fourier transform to the cross-correlation function of two signals:

$$S_{xy}(f) = \sum_{m=-\infty}^{\infty} R_{xy}(\tau) \cdot e^{-i \cdot f \cdot \tau} \quad (6.1)$$

With:

$$R_{xy}(\tau) = \sum_{t=0}^{T-\tau-1} x(t + \tau) \cdot y^*(t) \quad (6.2)$$

Where y^* is the complex conjugate of y (for real functions $y^* = y$).

Another relevant tool is the Power Spectral Density (PSD). The PSD describes how the power of a signal or time series is distributed along frequency. It is actually a particular case of the CPSD where the cross-correlation is calculated using the same signal and therefore obtaining the autocorrelation function, $R_{xx}(\tau)$. When the Fourier transform is applied to the autocorrelation, the PSD function $S_{xx}(f)$ is obtained:

$$S_{xx}(f) = \sum_{m=-\infty}^{\infty} R_{xx}(\tau) \cdot e^{-i \cdot f \cdot \tau} \quad (6.3)$$

With:

$$R_{xx}(\tau) = \sum_{t=0}^{T-\tau-1} x(t + \tau) \cdot x^*(t) \quad (6.4)$$

Where x^* is the complex conjugate of x (for real functions $x^* = x$).

The PSD has no complex part and allows a quick overview of the signal properties.

From all properties that can be obtained by using theory of signal analysis, two basic properties are used repeatedly in this work.

- **1st Basic property:**

This property is related with the use of the PSD to determine the variance of the time signal. The variance of a time signal composed by different harmonic parts can be determined through:

$$\sigma_x^2 = \int_0^{\infty} S_{xx}(f)df - \bar{x}^2 \quad (6.5)$$

If the studied function is a harmonic, single-frequency time function with an approximate form $x(t) = \hat{x} \cdot \sin(\omega \cdot t)$, its amplitude \hat{x} can be easily determined through the PSD function. If the time interval is big enough, it can be assumed that $\bar{x}(t) = 0$ and $\sigma_x^2 = \frac{\hat{x}^2}{2}$. In this case, and using the equation (6.2), the amplitude of the sinus-function can be determined as:

$$\hat{x} = \sqrt{2 \cdot \int_0^{\infty} S_{xx}(f)df} = \sqrt{2} \cdot \sigma \quad (6.6)$$

This property will be used mostly to determine the accelerations' amplitude coefficients.

- **2nd Basic property:**

Proceeding analogously, a similar property can be deduced from the CPSD. Given two harmonic, single-frequency time functions with the same frequency and an approximate form $x(t) = \hat{x} \cdot \sin(\omega \cdot t)$ and $y(t) = \hat{y} \cdot \sin(\omega \cdot t)$, expression (4.2.15) can be rewritten as:

$$\sigma_{xy}^2 = \int_0^{\infty} S_{xy}(f)df = \frac{\hat{x} \cdot \hat{y}}{2} \quad (6.7)$$

In this case there is no phase difference between the signals, and therefore the imaginary part of the CPSD is equal to zero. If the signals have a phase difference β , the result of the integral can be expressed as follows:

$$\int_0^{\infty} S_{xy}(f)df = \frac{\hat{x} \cdot \hat{y}}{2} \cdot \cos(\beta) - \left(\frac{\hat{x} \cdot \hat{y}}{2} \cdot \sin(\beta) \right) \cdot i \quad (6.8)$$

Expression (6.8) shows how both real and imaginary parts have a direct relation with the phase between the signals.

In the next particular case, given the signals:

- $x(t) = \hat{x} \cdot \sin(\omega_e \cdot t)$
- $y(t) = \hat{y} \cdot \sin(\omega_e \cdot t + \theta)$
- $z(t) = \hat{z} \cdot \sin(\omega_e \cdot t + \phi)$
- $w(t) = y(t) + z(t)$

The result of integrating the spectrum can be expressed as:

$$\int_0^{\infty} S_{xw}(f)df = \frac{\hat{x} \cdot (\hat{y} \cdot \cos(\theta) + \hat{z} \cdot \cos(\phi))}{2} - \left(\frac{\hat{x} \cdot (\hat{y} \cdot \sin(\theta) + \hat{z} \cdot \sin(\phi))}{2} \right) \cdot i \quad (6.9)$$

This expression is used later to identify the damping forces, as the measured force signal (which would be equivalent to $w(t)$) is the sum of the inertial plus the aerodynamic forces (which could be $y(t)$) and the mechanical plus the aerodynamic damping forces (which must then be $z(t)$). In that case, the acceleration (equivalent to $x(t)$) would be used as reference signal.

To simplify notation, expression (6.9) will be written as follows:

$$\int_0^{\infty} S_{xw}(f)df = Re_{CPSD_{xw}} - (Im_{CPSD_{xw}}) \cdot i \quad (6.10)$$

From the last expression obtained with Basic property 2, the phase angle between functions $x(t)$ and $w(t)$ at the excitation frequency can be found using simple trigonometry expressions in the complex plane:

$$\beta_{xw} = \arctan\left(\frac{Im_{CPSD_{xw}}}{Re_{CPSD_{xw}}}\right) \quad (6.11)$$

If a more general case shall be studied, the phase difference β can be expressed for each frequency in the domain. In that case, given two signals $X(t)$ and $Y(t)$ the phase difference function as a function of the frequency can be found using the next expression:

$$\beta_{XY}(f) = \arctan\left(\frac{\text{Im}(S_{XY}(f))}{\text{Re}(S_{XY}(f))}\right) \quad (6.12)$$

These properties will be used to distinguish the inertial forces from the damping forces in the measured force signals.

6.2 Assumed ideal conditions to solve the problem

This section exposes the assumptions about the studied system that were used as a guide to process the data; in other words, this section shows the steps that would lead from a measured ideal data to the non-stationary, aerodynamic coefficients. It is divided in four parts.

The first one (sections 6.2.1 and 6.2.2) explains the taken assumptions about the dynamics of the tests (bending and torsion) and the relation between them. Thus it sets the foundations for the second one (section 6.3), in which the concepts explained in section 6.1 are used to extract all the necessary information of the measured signals. The third section explains conceptually the main idea and procedure that allows finding the aerodynamic magnitudes. Finally, the information extracted from the signals is used to calculate the aerodynamic coefficients.

6.2.1 Dynamics of the bending case

In order to simplify the whole mechanism supported by the force sensors, it is assumed that it can be considered as a simple mass oscillating in the vertical plane. Therefore its equations of movement can be expressed as:

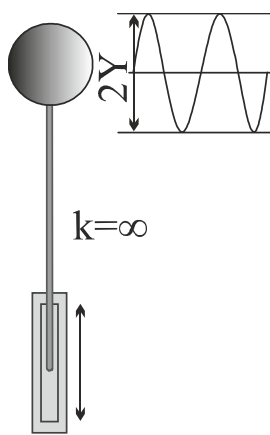


Figure 6.1: Oscillating mass as idealization of the problem.

$$y(t) = Y \cdot \sin(\omega_e \cdot t) \quad (6.13)$$

$$\dot{y}(t) = Y \cdot \omega_e \cdot \cos(\omega_e \cdot t) \equiv v \cdot \cos(\omega_e \cdot t) \quad (6.14)$$

$$\ddot{y}(t) = -Y \cdot \omega_e^2 \cdot \sin(\omega_e \cdot t) \equiv -a \cdot \sin(\omega_e \cdot t) \quad (6.15)$$

- "Y" is the oscillation amplitude, which is fixed by the distance to the center of the circular metallic discs at which the connecting rods are connected (see figure 4.1.7).

- " ω_e " can be expressed as $\omega_e = 2\pi f_e$, where f_e is the vertical excitation frequency. This frequency has a linear relation with the angular velocity of the metallic discs.

The movement, velocity and acceleration amplitudes are therefore "Y", "v" and "a" respectively. As a result, the inertial forces signal can be written as follows:

$$F_{b,i}(t) = -m \cdot \ddot{y}(t) = +m \cdot Y \cdot \omega_e^2 \cdot \sin(\omega_e \cdot t) \equiv +F_{b,i} \cdot \sin(\omega_e \cdot t) \quad (6.16)$$

The subscript “*b*” stands for “bending (test)”, while “*i*” stands for “inertial”.

The denotation “signal” will be used for all those variables that are time functions and therefore saved as vectors of discrete values.

At this stage the damping is assumed to be proportional to the velocity signal and opposed to the mass movement, therefore with opposite sign. Its signal can be written as:

$$D_{b,y}(t) = -C_y \cdot \dot{y}(t) = -C_y \cdot Y \cdot \omega_e \cdot \cos(\omega_e \cdot t) \equiv -D_{b,y} \cdot \cos(\omega_e \cdot t) \quad (6.17)$$

The damping signal as it is shown above has a phase difference of $\pi/2$ radians with the force and the acceleration signals. Theoretically only the damping signal is unknown, as the mass of the model and the pieces sustained above the force sensors can be known.

In an ideal case, the force sensors attached to the connecting rods would only measure the inertial forces and the damping signals in a case with no wind action. The measured signal would be therefore a sum of both signals and would be expressed as a unique one, which would have the next form:

$$F_{b,T}(t) = F_{b,i}(t) + D_{b,y}(t) = F_{b0}(t) + D_{b,y}(t) \equiv F_{b,T} \cdot \sin(\omega_e \cdot t + \beta) \quad (6.18)$$

Where the phase angle β is due to the phase difference between $F_{b,i}(t)$ and $D_{b,y}(t)$.

Here the equivalence $F_{b,i}(t) = F_{b0}(t)$ is introduced. The subscript “0” indicates that the signal proceeds from a test with no wind action. Due to the fact that a force signal composed exclusively by the inertial forces can only be obtained in this type of test (with no wind action), the subscript “0” will be used from now on and it will be assumed that, if this subscript follows a force signal, this signal will be an inertial force signal. Something similar happens with the damping signals: a signal $D_{b,y0}(t)$ proceeds from a test with no wind action and therefore represents exclusively the mechanical damping of the system.

Analogously, signals of the form $F_b(t)$ and $D_{b,y}(t)$ will indicate that they are composed by inertial and aerodynamic forces, and mechanical and aerodynamic damping respectively:

$$\begin{aligned} F_b(t) &= F_{b0}(t) + F_{b,a}(t) \\ D_{b,y}(t) &= D_{b,y0}(t) + D_{b,y,a}(t) \end{aligned} \quad (6.19)$$

Here the subscript “*a*” means “aerodynamic”. If the model was oscillating while being exposed to a wind action, the force transducers would also measure the aerodynamic forces. This would imply that the measured signal would be the sum of four forces:

$$\begin{aligned}
 F_{b,T}(t) &= F_{b0}(t) + D_{b,y0}(t) + F_{b,a}(t) + D_{b,y,a}(t) \\
 &= F_b(t) + D_{b,y}(t) \equiv F_{b,T} \cdot \sin(\omega_e \cdot t + \beta)
 \end{aligned}
 \tag{6.20}$$

In this case, after using the CPSD function two signals are obtained: one composed by the mechanical and the aerodynamic damping signals, and another one composed by the inertial and aerodynamic forces signals. In both cases the contribution of each of the forces to their sum cannot be superficially distinguished. The procedure to separate them is explained in sections 6.3 and 6.4.

6.2.2 Dynamics of the torsion case

In the torsion case the assumed situation is shown in figure 4.2.8. The equations of movement can be expressed in this case as follows:

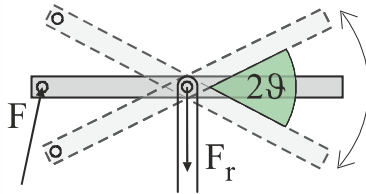


Figure 6.2: Simplified oscillating system in the torsion test

$$\varphi(t) = \vartheta \cdot \sin(\omega_e \cdot t) \tag{6.21}$$

$$\dot{\varphi}(t) = \vartheta \cdot \omega_e \cdot \cos(\omega_e \cdot t) \equiv w \cdot \cos(\omega_e \cdot t) \tag{6.22}$$

$$\ddot{\varphi}(t) = -\vartheta \cdot \omega_e^2 \cdot \sin(\omega_e \cdot t) \equiv -\alpha \cdot \sin(\omega_e \cdot t) \tag{6.23}$$

Here “ ϑ ” is the torsion oscillation angle, which is determined by the distance to the center of the circular metallic discs at which the connecting rods are connected (see Figure 4.7). The angle, angular velocity and angular acceleration amplitudes are therefore “ ϑ ”, “ w ” and “ α ” respectively.

In Figure 6.2 two forces are shown, “ F ” and “ F_r ”. The module of “ F ” is bigger due to the tilting of the connecting rods (see section 5.2.1)

The torsion case can be seen parallel to the bending case: here the moments take the place that forces had in the bending case, and the angular acceleration is used instead of the vertical acceleration to calculate the spectral functions (PSD and CPSD).

The inertial moments signal can be written as follows:

$$M_{t0}(t) = -\theta \cdot \ddot{\varphi}(t) = -\theta \cdot \vartheta \cdot \omega_e^2 \cdot \sin(\omega \cdot t) \equiv -M_{t0} \cdot \sin(\omega_e \cdot t) \tag{6.24}$$

The subscript “ t ” stands for “torsion (test)”, while “ 0 ” means that the moment signal was measured in a test with no wind action (see previous section, 6.2.1).

The damping is again assumed to be proportional to the angular velocity signal and opposed to the mass movement, therefore with opposite sign. Its signal can be written as:

$$D_{t,\varphi}(t) = -C_\varphi \cdot \dot{\varphi}(t) = -C_\varphi \cdot \vartheta \cdot \omega \cdot \cos(\omega_e \cdot t) \equiv -D_{b,\varphi} \cdot \cos(\omega_e \cdot t) \quad (6.25)$$

The damping signal as it is shown above has a phase difference of $\pi/2$ radians with the moment and the angular acceleration signals. As the mass moment of inertia of the model θ can be calculated, only the damping signal is theoretically unknown.

6.3 Use of spectral analysis in order to separate the system forces

Given the fact that the inertial and aerodynamic forces functions should have no phase difference with the acceleration function, the CPSD can be used in order to separate them from the damping forces using the 2nd basic property. Here a general example for a bending case will be presented.

The expected acceleration and forces in the oscillating system are described by the following expressions (here the acceleration vector is defined as positive when pointing down):

Acceleration: $\ddot{y}(t) = a \cdot \sin(\omega_e \cdot t)$

Inertial, aerodynamic forces: $F_b(t) = F_b \cdot \sin(\omega_e \cdot t)$

(6.26)

Mechanic, aerodynamic damping forces: $D_{b,y}(t) = -D_{b,y} \cdot \cos(\omega_e \cdot t)$

Total measured force: $F_{b,T}(t) = F_b(t) + D_{b,y}(t) = F_{b,T} \cdot \sin(\omega_e \cdot t + \beta)$

Given the acceleration $\ddot{y}(t)$ and the total measured force $F_{b,T}(t)$, two methods can be used in order to separate the forces and obtain the amplitude of their signals.

1. The first method use equation (6.9) from the 2nd basic property to separate the damping forces:

$$\int_0^\infty S_{F_{b,T}\ddot{y}}(f)df = \frac{a \cdot F_b}{2} - \left(\frac{a \cdot D_{b,y}}{2}\right) \cdot i \quad (6.27)$$

This result arises from the fact that $\ddot{y}(t)$ and $F_b(t)$ have no phase difference between them and that $\ddot{y}(t)$ and $D_{b,y}(t)$ have a phase difference of $-\pi/2$ radians. The phase

angle β between the signals $\ddot{y}(t)$ and $F_{b,T}(t)$ can be calculated now in the complex plane using the trigonometric expression (6.11):

$$\beta_{F_{b,T}\ddot{y}} = \arctan\left(\frac{Im_{CPSD_{xw}}}{Re_{CPSD_{xw}}}\right) = \arctan\left(\frac{D_{b,y}}{F_b}\right) \quad (6.28)$$

The obtained situation after using the CPSD and the integral of the spectrum is conceptually represented in next figure:

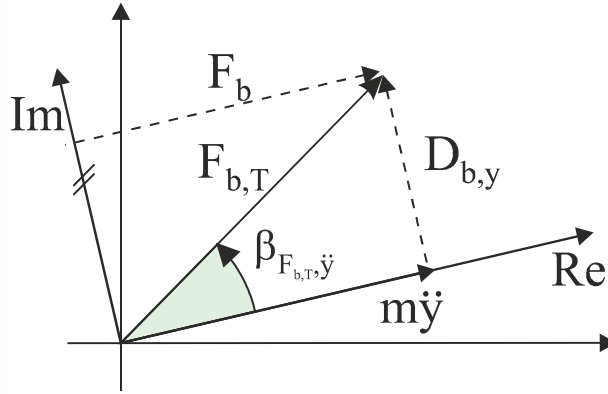


Figure 6.3: Phase angle between $F_{b,T}(t)$ and $\ddot{y}(t)$, and decomposition of $F_{b,T}(t)$ in inertial and aerodynamic forces ($F_b(t)$) and in damping forces ($D_{b,y}(t)$).

- The second method uses expression (6.12) to determine function $\beta(f)$, which shows the phase angle that corresponds to each frequency:

$$\beta_{F_{b,T}\ddot{y}}(f) = \arctan\left(\frac{Im(S_{\ddot{y}F_{b,T}}(f))}{Re(S_{\ddot{y}F_{b,T}}(f))}\right) \quad (6.29)$$

In this case the only wanted value of $\beta(f)$ is that one corresponding to the excitation frequency f_e . Once the phase angle is known, the wanted forces are found by multiplying the cosines or the sinus of the angle by the amplitude of the total measured force $F_{b,T}$, which is obtained through the variance property of the PSD shown in expression (6.6):

$$\text{Real part:} \quad F_b = F_{b,T} \cdot \cos(\beta_{F_{b,T}\ddot{y}}) \quad (6.30)$$

$$\text{Imaginary part:} \quad D_{b,y} = F_{b,T} \cdot \sin(\beta_{F_{b,T}\ddot{y}})$$

6.4 Conceptual proceeding to obtain the aerodynamic forces

The approach explained so far allows obtaining the amplitude of the inertial and the damping forces.

In order to obtain the aerodynamic coefficients, a distinction will be made between two types of data. The first type is formed by the only measurement (one per frequency) in which there is no wind acting on the bridge model during the tests, while the second one contains all those measurements in which, during the tests, there is wind acting with increasing velocity on the model. From the difference between a set of data measured with a certain wind velocity and the one with no wind action the aerodynamic coefficients will be obtained. In other words, the first type of data (measurement without wind) is subtracted to each different measurement of the second type (with wind action).

A conceptual representation of how the aerodynamic forces are determined in a bending test through this subtraction between sets of data is shown in Figure 6.4:

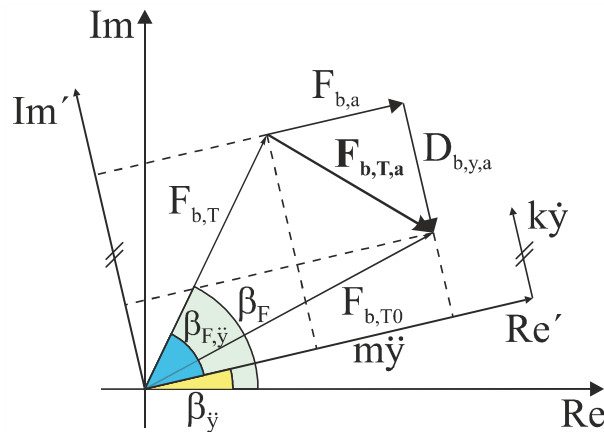


Figure 6.4: Conceptual determination of the aerodynamic force $F_{T,a}$, and its decomposition in F_a and D_a .

The steps that lead to the situation shown in Figure 6.4 are explained below with more detail using a general test case:

1. Firstly, a measurement of a situation with wind action is considered. The phase difference between the measured force signal and the acceleration signal can be expressed as follows:

$$\beta_{F\ddot{y}} = \beta_{F_{b,T}} - \beta_{\ddot{y}} \quad (6.31)$$

where $\beta_{F_{b,T}}$ and $\beta_{\ddot{y}}$ are the measured phase angles of the force and the acceleration respectively.

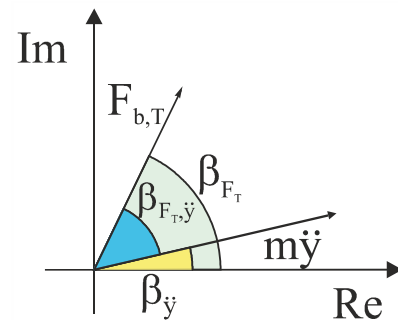


Figure 6.5: Total force and acceleration signals and angle between them

2. The damping vector, which is proportional to the velocity signal and thus orthogonal to the acceleration one, will be now used together with the acceleration vector in order to configure a new complex plane $Re' - Im'$, which will be rotated a certain angle respect to the original complex plane $Re - Im$.

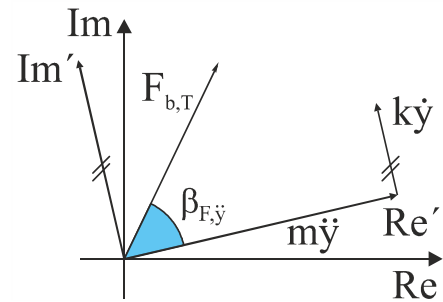


Figure 6.6: Determination of complex plane $Re' - Im'$

3. The angle $\beta_{F,y}$ determined in step 1 is now used as it has been previously explained (see equation (6.27)) to project the magnitude of the measured force signal " $F_{b,T}$ " on the new real and imaginary axis, $Re' - Im'$. The projection on the real axis corresponds to inertial and aerodynamic forces, while the projection on the imaginary axis corresponds to mechanical and aerodynamic damping. This process can also be done simply taking the real and imaginary parts of the CPSD between $F_{b,T}$ and \dot{y} (see expression (6.27)).

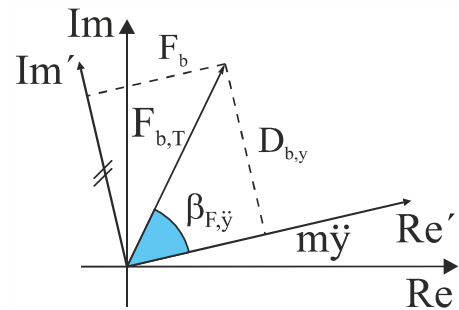


Figure 6.7: Projection of total force with wind action on the plane $Re' - Im'$

4. Now the same procedure is done for the case of no wind action, where the magnitude of the force is denoted as " $F_{b,T0}$ ". In this case, the projection in the real and the imaginary axis are respectively the inertial forces and the mechanical damping.

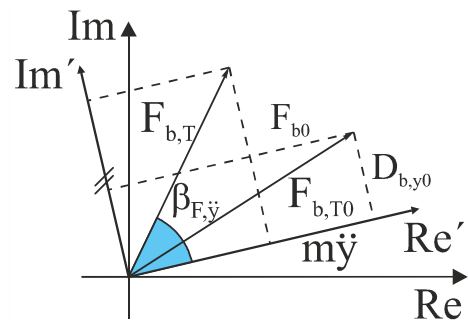


Figure 6.8: Projection of total force with no wind action on the plane $Re' - Im'$

$$F_{b,T}(t) = F_1 + F_2 + F_3 + F_4 \quad (6.33)$$

$$M_{b,T}(t) = (F_2 + F_4 - F_1 - F_3) \cdot a/2 \quad (6.34)$$

$$\ddot{y}_m(t) = \frac{(\dot{y}_1 + \dot{y}_2)}{2} \quad (6.35)$$

Before determining the aeroelastic coefficients, the difference between the oscillation amplitudes along the model due to the lack of stiffness must be considered. This phenomenon is corrected using the concepts explained in section 5.2.2 and the next expression:

$$\bar{Y} = \frac{1}{l} \int_0^l (Y_{extreme} + Y_{add.} \cdot \Phi(x)) dx = Y_{extreme} + Y_{add.} \cdot I_{y,nom} \quad (6.36)$$

Where: $Y_{add.} = Y_{middle} - Y_{extreme}$ (6.37)

$I_{y,nom}$ is the result of the normalized integral in expression (5.6) explained in section 5.2.2, which has as a result 0.64

According to Starossek's approach [17] and considering a purely bending state ($\varphi_0 = c'_{\varphi\varphi} = c''_{\varphi\varphi} = 0$) the aerodynamic forces yield:

$$L_y = \pi \cdot \rho \cdot b^2 \cdot (c'_{yy} + i \cdot c''_{yy}) \cdot \bar{Y} \cdot \omega_y^2 \cdot e^{i\omega_y t} \quad (6.38)$$

$$M_\varphi = \pi \cdot \rho \cdot b^3 \cdot (c'_{\varphi y} + i \cdot c''_{\varphi y}) \cdot \bar{Y} \cdot \omega_y^2 \cdot e^{i\omega_y t} \quad (6.39)$$

The aeroelastic coefficients are determined by the difference of the measured reactions with and without wind. Therefore the forces in the system with wind action must be balanced. Considering a general case in which there are bending and torsion movements, the obtained expressions would be:

$$\text{Without wind action:} \quad \frac{F_0}{L} + \hat{F}_s = 0 \quad \frac{M_0}{L} + \hat{M}_s = 0 \quad (6.40)$$

$$\text{With wind action:} \quad \frac{F}{L} + \hat{F}_s + \hat{L}_y = 0 \quad \frac{M}{L} + \hat{M}_s + \hat{M}_\varphi = 0 \quad (6.41)$$

The symbol “ $\hat{}$ ” means that the forces are referred to one meter length and therefore, in this case, do not need to be divided by the model length “ L ”. \hat{F}_s and \hat{M}_s correspond to the forces

and moments due to mass inertia and damping. The wind forces would therefore be given by the expressions:

$$\hat{L}_y = \frac{-F + F_0}{L} \quad \hat{M}_\varphi = \frac{-M + M_0}{L} \quad (6.42)$$

Going back to the bending case, if now the ‘‘Theodorsen’s forces’’ are taken into account, equations (6.38) and (6.39) are introduced in the expressions in (6.42), and the trigonometric decomposition shown in (6.30) is considered, it yields the expressions of the aerodynamic coefficients in Starossek’s notation:

$$c''_{yy} = \frac{-D_{b,y} + D_{b,y0}}{\pi \cdot \rho \cdot b^2 \cdot \bar{Y} \cdot \omega_y^2 \cdot L} \quad (6.43)$$

$$c'_{yy} = \frac{-F_b + F_{b0} + (\hat{F}_{Theo} \cdot L)}{\pi \cdot \rho \cdot b^2 \cdot \bar{Y} \cdot \omega_y^2 \cdot L} \quad (6.44)$$

$$c''_{\varphi y} = \frac{-D_{b,\varphi} + D_{b,\varphi0}}{\pi \cdot \rho \cdot b^3 \cdot \bar{Y} \cdot \omega_y^2 \cdot L} \quad (6.45)$$

$$c'_{\varphi y} = \frac{-M_b + M_{b0}}{\pi \cdot \rho \cdot b^3 \cdot \bar{Y} \cdot \omega_y^2 \cdot L} \quad (6.46)$$

Here \hat{F}_{Theo} stands for ‘‘Theodorsen’s force’’. Its development and calculation will be explained in section 7.5.3.

Expressions (6.43) to (6.46) can be easily translated to Scanlan’s notation by using the next equivalences:

$$H_{1,B}^* = \frac{\pi}{4} \cdot c''_{yy} \quad (6.47)$$

$$H_{4,B}^* = \frac{\pi}{4} \cdot c'_{yy} \quad (6.48)$$

$$A_{1,B}^* = \frac{\pi}{8} \cdot c''_{\varphi y} \quad (6.49)$$

$$A_{4,B}^* = \frac{\pi}{8} \cdot c'_{\varphi y} \quad (6.50)$$

These equivalences consider the fact that Scanlan's coefficients are referred to the model's total width (hence the subscript "B" in their expressions) while Starossek's coefficients are always referred to the half width of the model. Changing the width reference in the Scanlan's notation enables comparing the results in this work with those of previous works.

6.5.2 Torsion case

Proceeding analogously to the bending case and considering the different distribution of the reaction forces, the reaction forces can be calculated as follows:

$$F_{t,T}(t) = F_1 + F_2 + F_3 + F_4 \quad (6.51)$$

$$M_{t,T}(t) = (F_3 + F_4) \cdot a/2 \quad (6.52)$$

$$\ddot{\varphi}_m(t) = \frac{(\ddot{y}_1 - \ddot{y}_2)/2}{c/2} \quad (6.53)$$

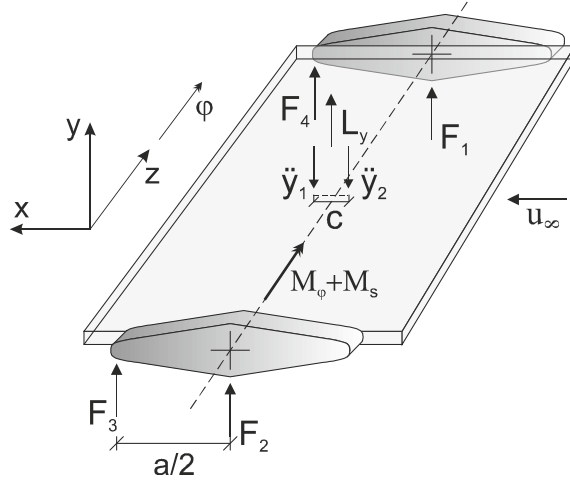


Figure 6.11: Location and positive direction of the torsion test magnitudes.

Before determining the aeroelastic coefficients, the difference between the oscillation angles along the model due to the lack of torsion stiffness must be considered. This phenomenon is corrected using the concepts explained in section 5.2.2 and the next expression:

$$\bar{\vartheta} = \frac{1}{l} \int_0^l (\vartheta_{extreme} + \vartheta_{add.} \cdot \Phi(x)) dx = \vartheta_{extreme} + \vartheta_{add.} \cdot I_{\varphi,nom} \quad (6.54)$$

Where: $\vartheta_{add.} = \vartheta_{middle} - \vartheta_{extreme}$ (6.55)

Here $I_{\varphi,nom}$ is the result of the normalized integral in expression (5.9) explained in section 5.2.2, which has as a result 0.67. Using Starossek's approach [17] and considering a purely torsion state ($y_0 = c'_{yy} = c''_{yy} = 0$), the aerodynamic forces are determined:

$$L_y = \pi \cdot \rho \cdot b^3 \cdot (c'_{y\varphi} + i \cdot c''_{y\varphi}) \cdot \varphi_0 \cdot \omega_\varphi^2 \cdot e^{i\omega_\varphi t} \quad (6.56)$$

$$M_\varphi = \pi \cdot \rho \cdot b^4 \cdot (c'_{\varphi\varphi} + i \cdot c''_{\varphi\varphi}) \cdot \varphi_0 \cdot \omega_\varphi^2 \cdot e^{i\omega_\varphi t} \quad (6.57)$$

Analogous to the bending case, introducing equations (6.56) and (6.57) in the expressions in (6.42), it yields the aeroelastic coefficients in Starossek's notation:

$$c''_{y\varphi} = \frac{-D_{t,y} + D_{t,y0}}{\pi \cdot \rho \cdot b^3 \cdot \bar{\vartheta} \cdot \omega_\varphi^2 \cdot L} \quad (6.58)$$

$$c'_{y\varphi} = \frac{-F_t + F_{t,0}}{\pi \cdot \rho \cdot b^3 \cdot \bar{\vartheta} \cdot \omega_\varphi^2 \cdot L} \quad (6.59)$$

$$c''_{\varphi\varphi} = \frac{-D_{t,\varphi} + D_{t,\varphi 0}}{\pi \cdot \rho \cdot b^4 \cdot \bar{\vartheta} \cdot \omega_\varphi^2 \cdot L} \quad (6.60)$$

$$c'_{\varphi\varphi} = \frac{-M_t + M_{t0} + (\widehat{M}_{Theo} \cdot L)}{\pi \cdot \rho \cdot b^4 \cdot \bar{\vartheta} \cdot \omega_\varphi^2 \cdot L} \quad (6.61)$$

In this case the moment due to the acceleration of the surrounding air mass \widehat{M}_{Theo} has also been considered. Once again, these coefficients can be translated to the Scanlan's notation:

$$H_{2,B}^* = \frac{\pi}{8} \cdot c''_{y\varphi} \quad (6.62)$$

$$H_{3,B}^* = \frac{\pi}{8} \cdot c'_{y\varphi} \quad (6.63)$$

$$A_{2,B}^* = \frac{\pi}{16} \cdot c''_{\varphi\varphi} \quad (6.64)$$

$$A_{3,B}^* = \frac{\pi}{16} \cdot c'_{\varphi\varphi} \quad (6.65)$$

The different deck width has also been considered in this translation expressions.

7 Study case: solution algorithm applied to the Simone-de-Beauvoir footbridge in Paris

7.1 Introduction

In section 5.2 the main correction algorithms that are necessary to obtain a data clean from the most important noise and distortions have been presented. In section 5.3 some concepts and ideas about signal filtering have led to a filter type choice that will be the basis for the oncoming determination of the used filter. In section 6.1 the basic necessary theory of spectral analysis has been explained in order to give a background for section 6.2, where the most important assumptions have been exposed and a solution approach in form of different steps has been presented.

This section presents the steps, operations and algorithms that have been actually carried out during and after the testing of the Simone-de-Beauvoir footbridge model in order to obtain the final results presented in this work. As a result, several references to previously explained concepts will be used all along this section. This section is also divided in a few subsections that describe chronologically most of the decisions, definitions and parameters used to determine the aerodynamic coefficients.

Firstly some aspects relative to mechanic and physic properties of the test rig are considered in order to minimize the influence that stationary and mechanic effects may have in the measurements (section 7.2). Afterwards the actual parameters that define the test duration, the excitation frequency and the measuring event will be determined and justified (section 7.3).

Secondly, after the measurements have been actually done, the operations to obtain the necessary test magnitudes – such as forces, moments and accelerations at middle section – are exposed (section 7.4.2). A filter will be determined in order to suppress the information of unwanted frequencies by filtering the signals of the defined test magnitudes, which will be then saved in a more ordered, comprehensible way (section 7.4.3).

Finally, the amplitudes of the magnitude's signals will be determined through spectral analysis (section 7.5.1), some effects like the additional deflection due to the lack of stiffness and the acceleration of the surrounding air will be considered and quantified (sections 7.5.2 and 7.5.3), and the aerodynamic coefficients will be calculated (section 7.5.4). The results and commentaries about this work are found in section 0.

7.2 Considerations previous to the measurements

In order to measure the forces to which the model is submitted, four force transducers are used. Each of them is located in the inferior part of the connecting rods (see Figure 4.7). The main characteristics of the force transducers can be found in section 4.3.3 and in the annex 11.3. As they are located in the rods, they will measure not only the inertial and damping forces of the model, but also those forces of the several connecting elements, such as the

model holder and the vertical guide (see Figure 4.8). The mass of all those elements (included the one of the connecting rods) was previously measured as a control value.

Element	Mass
Connecting rods (x4)	$1.09+1.165+1.14+1.17 = 4.56$ kg
Vertical guides (x2)	$1.06 + 0.84 = 1.9$ kg
Model holders (x2)	$0.59+0.65= 1.24$ kg
Bridge model	21.77 kg
TOTAL	29.47 kg

Table 7.1: Masses of elements above the force transducers

Three accelerometers were used during the tests. Two of them were located in the middle section with a distance between them of 14 cm and, consequently, both had a horizontal distance of 7 cm respect to the geometric center of the section. The third one was located always in the extreme section: in the bending case it was in the vertical middle plane, while in the torsion case it was at a distance of 8.6 cm respect to it. This way, additional deflections due to insufficient stiffness could be considered.

Before starting each series of measurements the pressure and the temperature were measured near the model in order to determine the air density according to section 4.4.2 and to equation (4.1). Besides, the motor of the test rig had been turned on and working for 30-45 minutes, which implies that the model had been oscillating at a frequency higher than 2 Hz during that time. This was done in order to obtain constant damping.

7.3 Setting the measurement parameters

7.3.1 Amplitude, excitation frequency and wind velocities

Before the tests exposed in this work, several tests were carried out varying all test parameters in order to study how they affected to the measured data and to find which ones would take to the optimal results. Thus different combinations of excitation frequencies, oscillation amplitudes and wind velocity configurations were proved and some experience could be acquired from the results.

For example, it was appreciated that the lower the excitation frequencies were, the higher the dispersion in the measured values was, and the more importance the unavoidable noises and distortions got. Therefore higher frequencies were automatically preferred to lower ones. However, higher frequencies also made the model more unstable, endangering the whole model and risking a possible breakdown (the inertial forces experimented by the model are proportional to the square of its oscillation frequency). This effect could be reduced by reducing the oscillation amplitude, which linearly reduces the inertial forces. This reduction did not only allow testing higher excitation frequencies, but also widened the range of frequencies that could be tested. However, the experience acquired showed that small oscillation amplitudes gave less smooth results than the big ones. The final chosen amplitude

value was big enough to give relatively smooth results, but small enough to prove a wide enough range of excitation frequencies.

A few reference and clarifying values about the used amplitudes and the frequencies they allowed to test are shown in the next table:

Series of essays	Amplitude	Range of excitation frequencies f_e
First series	33.5 mm	Approx: 0 – 2.75 Hz
Second series	13.5 mm	Approx: 0 – 3.50 Hz
Final series	29.5 mm	Approx: 0 – 3.00 Hz

Table 7.2: Range of reachable frequencies for different oscillating amplitudes.

Regarding to the wind velocity, as the aerodynamic coefficients are expressed in function of the reduced velocity $u_{red,B} = u_{\infty}/(B \cdot f_e)$, the undisturbed wind velocities u_{∞} were chosen in accordance to the excitation frequency of each series of tests, and in order to obtain sufficiently complete coefficient curves: this means, using a discretization precise enough so that possible deviations in the curves due to error propagation or temporary abnormalities during the testing were not attributed to a real tendency of the aerodynamic curve.

Finally, in the first measurements it was appreciated a difference in the results for the same reduced velocities when different excitation frequencies were used. Therefore the final measurement is compounded by three series of tests for each case, bending and torsion (six series in total). Each of these six series has one excitation frequency, and 31 different undisturbed velocity values. Due to the fact that each series has a different excitation frequency (3 different frequencies for bending tests, the same ones for torsion tests), different wind velocities are used in order to obtain aerodynamic coefficients with the same reduced velocity coordinates.

The next table shows the chosen frequencies and the corresponding wind velocities that, at oscillation amplitude of 29.5 mm, were used to obtain the wanted $u_{red,B}$ values. The range of values of $u_{red,B}$ expands from 0 to 15 (with 31 values in between) in order to stay in the non-stationary region and to make the results of this work comparable with the ones from other sources:

$U_{red,B}$ []	Frequency [Hz]		
	2.50	2.75	3.00
0	0	0	0
0,5	0,41	0,45	0,49
1	0,82	0,9	0,99
1,5	1,23	1,36	1,48
2	1,64	1,81	1,97
2,5	2,06	2,26	2,47
3	2,47	2,71	2,96
3,5	2,88	3,16	3,45
4	3,29	3,62	3,95
4,5	3,7	4,07	4,44
5	4,11	4,52	4,93
5,5	4,52	4,97	5,43
6	4,93	5,43	5,92
6,5	5,34	5,88	6,41
7	5,75	6,33	6,9
7,5	6,17	6,78	7,4
8	6,58	7,23	7,89
8,5	6,99	7,69	8,38
9	7,4	8,14	8,88
9,5	7,81	8,59	9,37
10	8,22	9,04	9,86
10,5	8,63	9,49	10,36
11	9,04	9,95	10,85
11,5	9,45	10,4	11,34
12	9,86	10,85	11,84
12,5	10,28	11,3	12,33
13	10,69	11,75	12,82
13,5	11,1	12,21	13,32
14	11,51	12,66	13,81
14,5	11,92	13,11	14,3
15	12,33	13,56	14,8

Table 7.3: Undisturbed wind velocities at given frequencies in order to obtain the wanted reduced velocities.

Table 7.3 shows the $u_{red,B}$ wanted values. However, due to technical inaccuracies, only close values to those could be achieved. For example, in the case of the excitation frequencies the real frequencies that could be achieved in the bending tests were 2.51Hz, 2.75 Hz and 2.99 Hz (instead of the values exposed in the table). Something similar happened while setting the wind velocities in the wind tunnel, as it is considerably difficult to set exact wind velocity values. The real wind velocity values were however measured and averaged to obtain the real value of $u_{red,B}$ at which the measuring event took place. This was the value taken into account when representing the aerodynamic coefficients.

7.3.2 Number of values

As it was commented in section 4.4.4, three different parameters can be used in order to determine a measuring event and its corresponding number of values.

The first parameter used in this case was the sample rate. The sample rate ascended from an initial value of 500 Hz to a definitive value of 1 kHz. This was due, on one hand, to the habit in this department (“*Institute of steel construction - RWTH Aachen*”) of using a similar sample rate in other experiments with the same measuring equipment and obtaining good results and, on the other hand, to the presence of unavoidable noise derived from construction reasons (friction between parts, vibration of the belts which connect the motor to the model structure,...). This noise made necessary a higher sample rate in order to get the complete waves of the noise signal, which makes more effective the filtering process aimed to its removal.

The second parameter was the number of values. Firstly, the time extension of the measurement should be long enough so that approximately 150-200 cycles occur in each measurement in order to improve the later calculation of the power spectral density. Secondly, as the posterior analysis of the measured data occurs in the frequency domain, functions as the power spectral density (PSD) and the cross power spectral density (CPSD) would be applied to the data values, which implied using the Fast Fourier Transform (FFT) in the middle calculations. Therefore a value of the form 2^N was to be chosen, as the FFT deletes all the additional values over the 2^N th value (as long as they do not reach the 2^{N+1} th one). This 2^N -form value would however not be the definitive one, as after applying the filter to the measured values a transition, not constant zone arises at the beginning of the filtered signal (see section 5.3). The time this transition zone needs to get stable depends on the parameters of the filter and can vary between 5 and 15 seconds approximately. The chosen filter has actually two of those transition zones (see section 7.4.3). In order to optimize the number of values, these transition zones were observed and their duration was found to be around of 6 seconds in each of them. Therefore an additional number of 15000 values (15 seconds) was added to the 2^N -form value.

As a result, considering a sample rate of 1 kHz and the fact that the chosen frequencies expand from 2.5 to 3 Hz, a measuring time between 1 and 2 minutes is required to measure approximately 150-200 cycles, and therefore the number of values that better accomplish the required conditions yields from the N-value $N=16$, which results into $2^{16}=65536$ values. This number must still be enlarged with the additional 15000 values to avoid the transition zones, which added to the original choice of 2^{16} ensures that the FFT will be done using 2^{16} values.

In conclusion, the final measuring process parameters are:

- Sample rate: 1000 Hz
- Number of Values: $65536 + 15000 \approx 80000$ values
- Measuring time: 80 seconds

7.4 Processing the measured data

7.4.1 Situation before processing the data

The measured data is automatically saved in three different folders, each one for a specific excitation frequency (2.5Hz, 2.75Hz and 3Hz). Each folder contains 31 files corresponding to the 31 measurements per frequency, from $u_{red,B} = 0$ until $u_{red,B} = 15$ with increments of $\Delta u_{red,B} = 0.5$. There are 6 folders in total (3 for bending case, 3 for torsion case). These 6x31 sets of data will be processed using two different algorithms: one in the bending tests and another one in the torsion tests. In both cases, the data will be saved in matrixes of magnitudes (a matrix for forces, another for accelerations ...) of 3x31 elements: 3 different excitation frequencies per 31 different wind velocities.

The theoretical assumptions and concepts that justify these algorithms have been explained in section 6.2; therefore the following sections are aimed exclusively to show the exact steps and operations that will lead from a measuring event to the final results.

7.4.2 Defining test magnitudes

7.4.2.1 Bending case

The test magnitudes are obtained by carrying out a group of operations with the still unmodified measured signals. Operations to define the magnitudes are therefore made before any kind of filtering or data processing, and give as a result a new group of vectors or signals with the same length as the original ones. The values of these magnitudes were calculated at each of the three excitation frequencies and for the previously determined 31 wind velocities, which were also measured during each test and its average value saved.

Analogously to Figure 6.10, Figure 7.1 shows approximately the points in which the forces and the accelerations were measured in the bending tests. It also shows the orientation in which the measured magnitudes were considered positive and, consequently, the resulting positive orientation of the aerodynamic forces.

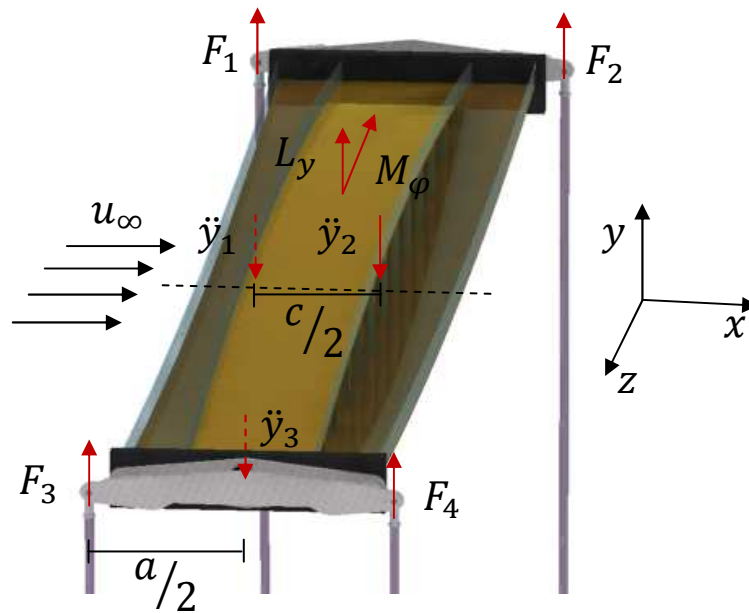


Figure 7.1: Location and positive orientation of the measured forces and accelerations in the bending test

Using the notation in Figure 7.1 and in accordance with the given coordinate system and the vectors' orientation, the next magnitudes were defined as follows (see section 6.5.1):

Force Signal:
$$F_{b,T}(t) = F_1 + F_2 + F_3 + F_4 \quad (7.1)$$

Moment Signal:
$$M_{b,T}(t) = (F_2 + F_4 - F_1 - F_3) \cdot \frac{a}{2} \quad (7.2)$$

Acceleration at middle section:
$$\ddot{y}_m(t) = \frac{\ddot{y}_1 + \ddot{y}_2}{2} \quad (7.3)$$

Acceleration at extreme section:
$$\ddot{y}_e(t) = \ddot{y}_3 \quad (7.4)$$

The result of applying expressions (7.1) to (7.4) is a group of four vectors that show the value of the defined magnitudes at every measured time step.

The vertical accelerations have no bending subscript because they are only defined and used in the bending tests.

7.4.2.2 Torsion case

Analogously to Figure 6.11, Figure 7.2 shows approximately the points in which the forces and the accelerations were measured in the torsion tests. It also shows the orientation in which the measured magnitudes were considered positive and, consequently, the resulting positive orientation of the aerodynamic forces.

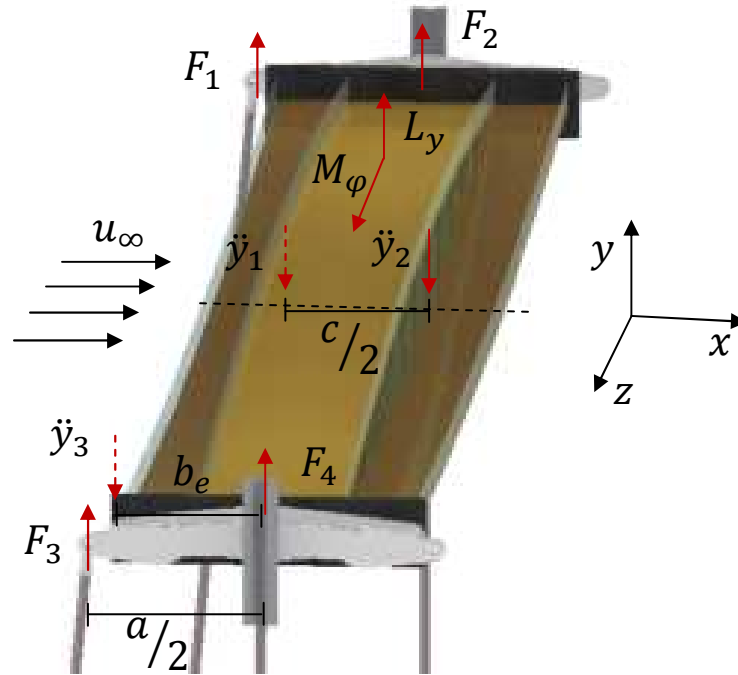


Figure 7.2: Location and positive orientation of the measured forces and accelerations in the torsion test

Using the notation in Figure 7.2 and in accordance with the given coordinate system and the vectors' orientation, the next magnitudes were defined as follow (see section 6.5.2):

$$\text{Force Signal:} \quad F_{t,T}(t) = F_1 + F_2 + F_3 + F_4 \quad (7.5)$$

$$\text{Moment Signal:} \quad M_{t,T}(t) = (-F_1 - F_3) \cdot \frac{a}{2} \quad (7.6)$$

$$\text{Torsion acceleration at middle section:} \quad \ddot{\varphi}_m(t) = \frac{\ddot{y}_1 - \ddot{y}_2}{2 \cdot c} \quad (7.7)$$

To define the torsion acceleration at the extreme section the notation in Figure 7.3 has been used.

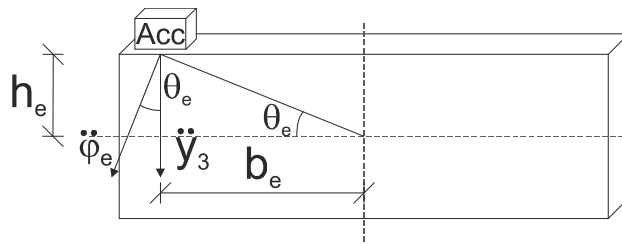


Figure 7.3: Decomposition of the torsion acceleration of the accelerometer located on the plate at the extreme of the bridge model.

Torsion acceleration at extreme section:
$$\ddot{\varphi}_e(t) = \frac{\dot{y}_3}{\cos(\vartheta_e) \cdot \sqrt{h_e^2 + b_e^2}} \quad (7.8)$$

There is a difference between the magnitudes defined here according to Figure 7.2, and those defined in section 6.5.2 according to Figure 6.11. Watching both figures it can be appreciated that the inflow comes from different directions. In this case it comes from the site at which the connecting rods are connected. This has important consequences relative to sign criteria, as the axis z changes its direction. In section 6.5.2 the magnitudes were defined in a way that all of them had almost the same phase displacement (they are different because of the damping forces). However, the way magnitudes are defined in this case, the force signal will have an additional phase displacement of π radians respect to the moment and torsion acceleration signals. As a result, when the CPSD is used to separate the damping vertical forces (2nd basic property in section 6.1) the obtained coefficients will have the opposite sign. Next figure summarizes this explanation:

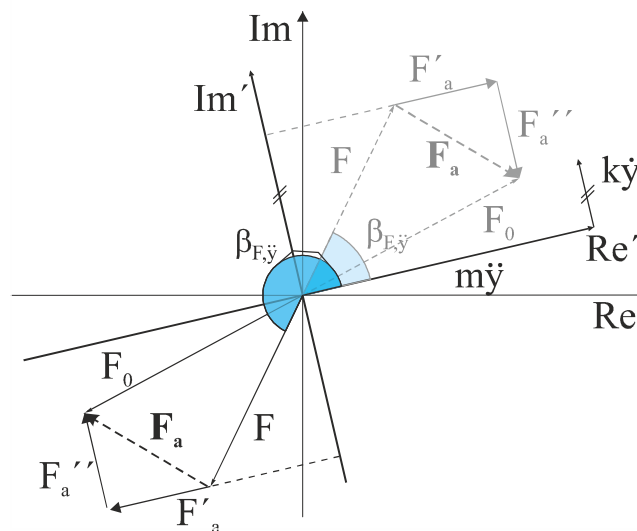


Figure 7.4: Change of sign of the forces coefficients after using the CPSD.

As it can be seen in Figure 7.4, the different orientation of the aerodynamic forces is due to the nature of the CPSD function and not to some physical reality, and thus can lead to confusion when trying to understand the experiment results. Therefore, this effect will be considered when describing and comparing the results in sections 8.3.1 and 8.3.2 by changing the sign of the aerodynamic force coefficients (the moment coefficients must not be changed) before their representation.

The result of applying expressions (7.5) to (7.8) is a group of four vectors that show the value of the defined magnitudes at every measured time step.

NOTE: The torsion accelerations have no torsion subscript because they are only defined and used in the torsion tests.

7.4.3 Filtering the data

As explained in section 5.3, the filtering of the signal results into a cleaner, smoother result of the spectral functions and enables an overview of the data values, which is useful to detect unexpected phenomena and possible early mistakes like technical problems during the measurement or sign-criteria related mistakes.

Section 5.3 also exposes the arguments that led to choose the band-pass filter to filter the signals. The effect of the different filter parameters such as the filter order and the slope between the band-pass and the stop-band on the filtered signal were studied before setting the definitive filter. Given the fact that the excitation frequency is much lower than that from noise and distortion, a high filter order will not be required.

The filter response was determined through the function “`fdesign.bandpass`” of MATLAB. The chosen filter was a band-pass filter of order 4 with a bandwidth of 0,5Hz (this band width was centered at the excitation frequency determined with the PSD, not at the theoretical one). It was designed by fixing the filter’s order, the cutoff frequency for the point 3dB below the passband value for the first cutoff ($f_e - 0,25\text{Hz}$) and the cutoff frequency for the point 3dB below the passband value for the second cutoff ($f_e + 0,25\text{Hz}$). The used filter design method was the Butterworth design, as it presents an almost inexistent ripple (a characteristic not offered by other methods, like the chebyshev and the elliptic design methods) and a steep transition between passband and stopband.

As exposed in section 5.3, some filtering implementations can provoke a phase displacement between the original signal and the filtered one. Even though this effect should not affect the relative phase between the test magnitudes (because they are measured at the same excitation frequency and would therefore have the same phase displacement), a zero-phase digital filter was used in order to avoid any phase displacement between the signals.

The filter implementation was determined by using the function “`filtfilt`” from MATLAB ([20], [21]). This function performs a zero-phase digital filtering by processing the input data in both forward and reverse directions: after filtering the data in the forward direction, “`filtfilt`” reverses the filtered sequence and runs it back through the filter. The result is a zero-phase distortion, a filter transfer function that equals the squared magnitude of the original filter transfer function and a filter order that is double the order of that specified with the “`fdesign.bandpass`” function. These facts have two main consequences, apart from the evident zero-phase displacement. Firstly, the filter effect will be equivalent to that of a filter with order 8. This is actually more similar to the wanted filter order, and thus a filter order of 4 was set in the “`fdesign.bandpass`” function (higher filter orders improve only slightly the result and are therefore not necessary). A lower filter order (2 in the “`fdesign.bandpass`” function, 4 after the “`filtfilt`” implementation) worked also well for most of the cases, but gave unsatisfactory results for a few signals. Secondly, this forward and reverse filtering implies the existence of two transition zones of the same length: one at the beginning of the signal, the other one at the end. However, “`filtfilt`” minimizes these transients by matching initial conditions, so that the values that must be deleted from the signal are not too many. With the parameters used until now, both transition zones had a duration of approximately 6 seconds each one, which implies that around 12000 values should be deleted (thus the 15000 additional number of values).

More information about the filter parameters and coefficients can be found in annex 11.2.

7.5 Calculating the non-stationary, aeroelastic coefficients

7.5.1 Amplitudes of the magnitude's signals

The first step after filtering the data is calculating the exact excitation frequency at which the test has been carried out. This is done in order to check that the real excitation frequency is close enough to the chosen one and, in this case, to repeat the filtering process using the calculated frequency as center of the bandwidth.

Afterwards the power spectral density (PSD) of the accelerations was calculated: the vertical accelerations in the bending case and the torsion accelerations in the torsion case. Assuming that the acceleration signals can be described as $\ddot{y}(t) = a \cdot \sin(\omega_e \cdot t)$ in the first case and as $\ddot{\varphi}(t) = \alpha \cdot \sin(\omega_e \cdot t)$ in the second one, their amplitudes can be calculated using the 1st basic property of section 6.1:

$$a_m = \sqrt{2 \cdot \int_0^{\infty} S_{\dot{y}_m \dot{y}_m}(f) df} \quad (7.9)$$

$$a_e = \sqrt{2 \cdot \int_0^{\infty} S_{\dot{y}_e \dot{y}_e}(f) df} \quad (7.10)$$

$$\alpha_m = \sqrt{2 \cdot \int_0^{\infty} S_{\dot{\varphi}_m \dot{\varphi}_m}(f) df} \quad (7.11)$$

$$\alpha_e = \sqrt{2 \cdot \int_0^{\infty} S_{\dot{\varphi}_e \dot{\varphi}_e}(f) df} \quad (7.12)$$

Using as reference equation (6.27), the vertical acceleration is used in the bending tests to separate the inertial and aerodynamic part from the damping part in the force and moment signals. This will be done by calculating the CPSD between $F_{b,T}$ and \ddot{y}_m or $M_{b,T}$ and \ddot{y}_m in the bending tests, and between $F_{t,T}$ and $\ddot{\alpha}_m$ or $M_{t,T}$ and $\ddot{\alpha}_m$ in the torsion tests, where the all this signals have been defined in sections 7.4.2.1 and 7.4.2.2:

Bending tests

$$F_b = \text{real} \left(2 \cdot \frac{\int_0^\infty S_{F_b,T\ddot{y}_m}(f) df}{\alpha_m} \right) \quad (7.13)$$

$$D_{b,y} = \text{imag} \left(2 \cdot \frac{\int_0^\infty S_{F_b,T\ddot{y}_m}(f) df}{\alpha_m} \right) \quad (7.14)$$

$$M_b = \text{real} \left(2 \cdot \frac{\int_0^\infty S_{M_b,T\ddot{y}_m}(f) df}{\alpha_m} \right) \quad (7.15)$$

$$D_{b,\varphi} = \text{imag} \left(2 \cdot \frac{\int_0^\infty S_{M_b,T\ddot{y}_m}(f) df}{\alpha_m} \right) \quad (7.16)$$

Torsion Tests

$$F_t = \text{real} \left(2 \cdot \frac{\int_0^\infty S_{F_t,T\ddot{\phi}_m}(f) df}{\alpha_m} \right) \quad (7.17)$$

$$D_{t,y} = \text{imag} \left(2 \cdot \frac{\int_0^\infty S_{F_t,T\ddot{\phi}_m}(f) df}{\alpha_m} \right) \quad (7.18)$$

$$M_t = \text{real} \left(2 \cdot \frac{\int_0^\infty S_{M_t,T\ddot{\phi}_m}(f) df}{\alpha_m} \right) \quad (7.19)$$

$$D_{t,\varphi} = \text{imag} \left(2 \cdot \frac{\int_0^\infty S_{M_t,T\ddot{\phi}_m}(f) df}{\alpha_m} \right) \quad (7.20)$$

F and D_y (whether in bending or torsion tests) are the inertial and aerodynamic vertical forces and the vertical damping forces respectively. M and D_φ are the inertial and aerodynamic moment and the torsion damping forces respectively.

In both cases the function “*cpsd*” (Cross Power Spectral Density) of MATLAB was used ([22],[23],[24]); in the first case using the same signal in both inputs to obtain the PSD, while in the second case using two different signals to obtain the CPSD.

If the force and acceleration signals proceed from a test in which there was no wind action, the subscript “0” will be added to the force, moment and damping coefficients. These coefficients will then represent the magnitudes of a test without wind action: this means, the inertial forces and moments, and the mechanic damping. They will be subtracted to the coefficients proceeding from tests with wind action in order to obtain the aerodynamic forces, moments and damping values.

The next equations show the concept of this proceeding:

No wind action during tests:	Wind action during tests:	Subtraction:
$F_{T0} = F_{i0} + D_{y0}$	$F_T = F_{i0} + F_a + D_{y0} + D_{y,a}$	$F_T - F_{T0} = F_a + D_{y,a}$
$M_{T0} = M_{i0} + D_{\varphi0}$	$M_T = M_{i0} + M_a + D_{\varphi0} + D_{\varphi,a}$	$M_T - M_{T0} = M_a + D_{\varphi,a}$

(7.21)

Here “*i*” stands for “inertial”, and “*a*” for “aerodynamic”.

7.5.2 Additional deflection due to lack of stiffness

Due to the fact that the bridge model is not perfectly rigid, the middle section is expected to have higher accelerations and deflection values than the extreme section. In order to take this phenomenon into account an additional accelerometer \ddot{y}_3 was placed in the extreme model section as Figure 7.1 and Figure 7.2 show.

In the bending test, assuming that the movement equations are described by expressions (6.13) to (6.15), the displacements in the middle and extreme sections can be calculated as follows:

$$Y_{MS} = \frac{a_m}{\omega^2} \quad (7.22)$$

$$Y_{ES} = \frac{a_e}{\omega^2} \quad (7.23)$$

Here a_m and a_e are the accelerations in the middle and the extreme section respectively as they have been defined in equations (7.9) and (7.10), and Y_{MS} and Y_{ES} are the deflections in middle and extreme section respectively. The additional deflection in middle section can be therefore calculated as:

$$Y_{ADD} = Y_{MS} - Y_{ES} \quad (7.24)$$

The additional deflection values ranged from 0.18 cm at an oscillating frequency of 2.5Hz to 0.25 cm at 3Hz, both cases with an oscillation amplitude of 2.95 cm.

The corresponding value of the additional deflection is then taken into account as explained in section 5.2.2. For this reason, the deflection that will be considered in future expressions will be the following one:

$$\bar{Y} = Y_{ES} + 0.64 \cdot Y_{ADD} \quad (7.25)$$

The expressions for the deflections in the torsion case can be determined proceeding analogously. Although Hortmanns [1] proved that the effect of the additional deflection in the torsion case can be neglected, they will be also calculated in this work. The used expressions are:

$$\vartheta_{MS} = \frac{\alpha_m}{\omega^2} \quad (7.26)$$

$$\vartheta_{ES} = \frac{\alpha_e}{\omega^2} \quad (7.27)$$

Here α_m and α_e are the torsion accelerations in the middle and the extreme section respectively as they have been defined in equations (7.11) and (7.12), and φ_{MS} and φ_{ES} are the deflections in middle and extreme section respectively. The additional deflection in middle section can be therefore calculated as:

$$\vartheta_{ADD} = \vartheta_{MS} - \vartheta_{ES} \quad (7.28)$$

The additional deflection values ranged from 0.0113 radians at an oscillating frequency of 2.5Hz to 0.0182 radians at 3Hz for an oscillation angle of 0.152 radians. This means that, in the middle section, a point located at the extreme of the section will have an additional vertical displacement of approximately 0.3 cm.

In this case the order of magnitude of the additional deflections and displacements in the middle section in bending and torsion cases is the same: a deflection in middle section approximately a 10% bigger than the one in extreme section, which in both cases implies an additional vertical displacement of approximately 2,5 mm. This means that the effect of the lack of stiffness cannot be neglected in the torsion case. The fact that Hortmanns [1] stated the opposite might well be due to the fact that the bridge models he used in his tests were of a different nature to the one used in this work: Hortmanns used a 6x3x2 cm (WidthxHeightxThickness) metal core as bridge axis, which provided enough stiffness, and different light covers which gave the desired geometry to the model sections. The rectangular form of this covers probably conferred enough torsion stiffness to the model as to neglect the additional torsion deflection.

In this work the additional torsion deflection will be taken into account as explained in section 5.2.2. For this reason, the torsion deflection that will be considered in future expressions will be the following one:

$$\bar{\vartheta} = \vartheta_{ES} + 0.67 \cdot \vartheta_{ADD} \quad (7.29)$$

7.5.3 Aerodynamic force of the surrounding air

In section 2.1.1 the concept of the aerodynamic force and moment due to the surrounding air was introduced. They can be expressed using the accelerations signals as follows:

$$L_{\ddot{y}}(t) = -\frac{\pi \cdot \rho}{4} \cdot B^2 \cdot \ddot{y}_m(t) \quad (7.30)$$

$$M_{\ddot{\varphi}}(t) = -\frac{\pi \cdot \rho}{128} \cdot B^4 \cdot \ddot{\varphi}_m(t) \quad (7.31)$$

Given the fact that these expressions were first presented by Theodorsen [18], they will be referred to as “Theodorsen’s forces” in this work.

The Theodorsen’s forces are linearly dependent on the accelerations of the model, which are mostly function of the excitation frequency and very slightly dependent on the velocity of the wind acting on the model. This implies that, given an excitation frequency, the Theodorsen’s forces will remain almost constant for all the different wind velocities that will act on the bridge (because these forces are linearly dependent on the accelerations in middle section, which grow slightly but are mostly constant). As a result, coefficients H_4^* and A_3^* , which correspond to the force and moment parts respectively, will no longer evolve along the $y = 0$ axis, but along the constant value of the Theodorsen’s forces.

The amplitudes of the signals can be calculated using the variance of the PSD signal as in expression (6.6):

$$\hat{F}_{Theo} = \sqrt{2 \cdot \int_0^{\infty} S_{L_{\ddot{y}}L_{\ddot{y}}}(f) df} \quad (7.32)$$

$$\hat{M}_{Theo} = \sqrt{2 \cdot \int_0^{\infty} S_{M_{\ddot{\varphi}}M_{\ddot{\varphi}}}(f) df} \quad (7.33)$$

The Theodorsen’s forces have dimensions of force per unit length and are consequently denoted with the symbol “ $\hat{\quad}$ ”. Therefore they will be multiplied by the model length L

before being added to the other calculated coefficients, which are already referred to the model length. The result will be afterwards normalized and translated to Scanlan's notation.

7.5.4 Calculating the aerodynamic coefficients

Once the amplitude of the magnitudes and the additional deflections have been determined, the aerodynamic coefficients can be calculated. The variables obtained until now are:

	Variables		Description	Extension (of each Var.)		
Signals (values vectors)	Bending Test	$F_{b,T}(t), M_{b,T}(t), \dot{y}_m(t), \dot{y}_e(t)$	Signals (vectors of values) of the magnitudes defined using the enclosed expressions:	(6.3.1) to (6.3.4)	- 3 excitation frequencies (f_e) - 31 different wind velocities - 80000 values per measurement	3x31x80000
	Torsion Test	$F_{t,T}(t), M_{t,T}(t), \dot{\phi}_m(t), \dot{\phi}_e(t)$		(6.3.5) to (6.3.8)		3x31x80000
Coefficients without wind action	Bending Test	$F_{b0}, D_{b,y0}, M_{b0}, D_{b,\varphi0}, \alpha_{m0}, \alpha_{e0}$	Amplitudes of the signals measured with no wind action: thus inertial and mechanic parts. Besides, amplitudes of:	Vertical accelerations without wind.	- 3 excitation frequencies (f_e) (the first wind velocity of each f_e , which corresponds to the value $u_\infty = 0$)	3
	Torsion Test	$F_{t0}, D_{t,y0}, M_{t0}, D_{t,\varphi0}, \alpha_{m0}, \alpha_{e0}$		Torsion accelerations without wind.		3
Coefficients with wind action	Bending Test	$F_b, D_{b,y}, M_b, D_{b,\varphi}, \alpha_m, \alpha_e$	Amplitudes of the signals measured with wind action: inertial, mechanic and aerodynamic parts. Besides, amplitudes of:	Vertical accelerations with wind.	- 3 excitation frequencies (f_e) - 30 different wind velocities (only $u_\infty = 0$ excluded).	3x30
	Torsion Test	$F_t, D_{t,y}, M_{t,b}, D_{t,\varphi}, \alpha_m, \alpha_e$		Torsion accelerations with wind.		3x30
Theodorsen forces	Bending Test	\hat{F}_{Theo}	Inertial forces of the surrounding air mass due to:	Vertical acceleration	- 3 excitation frequencies (f_e) - 31 different wind velocities	3x31
	Torsion Test	\hat{M}_{Theo}		Torsion acceleration		3x31

Table 7.4: Variables and magnitudes obtained after applying the solution algorithm explained in section 5.

At this point, all the necessary variables and magnitudes have been calculated and are available for the calculation of the aerodynamic coefficients.

These coefficients are finally obtained using expressions (6.43) to (6.46) in the bending case and (6.58) to (6.61) in the torsion case.

They are later translated to Scanlan's notation by using expressions (6.47) to (6.50) in the bending case and (6.62) to (6.65) in the torsion case.

8 Results and commentaries

8.1 Introduction to the analysis of the results

Once all coefficients have been calculated, they are represented as function of the reduced velocity. In order to calculate the real reduced velocity $u_{red,B}$ at which the measurement took place, expression (2.21) was used. In each measured event the undisturbed wind velocity u_∞ was measured and averaged to that end. The real excitation frequency f_e transmitted by the motor during the measurement was determined by finding the ordinate of the peak value in the PSD function of a force signal (any signal measured at the same excitation frequency can be equally used). By calculating these two variables, more realistic values of the reduced velocities that correspond to the coefficients were obtained.

In order to understand the curves of the resultant coefficients, it is essential to know how the coefficients were defined. A visual representation of their definition can be found in section 6.4. However, the best way to understand in which direction they are positive is looking directly at their equations (see expressions (6.43) to (6.46) for the bending case and (6.58) to (6.61) for the torsion case, both in section 6.5). As it can be seen there, the forces and moments proceeding from tests without wind action (the inertial and mechanical parts) have positive sign, while those proceeding from tests with wind action (the ones that contain the aerodynamic information) have a negative sign. This means that the magnitudes measured with aerodynamic effects are subtracted to those without them. Let's now take a force coefficient as an example. Then a positive coefficient will mean that the inertial forces (measured in tests without wind action) are bigger than the forces measured in a test with wind action, which implies that the aerodynamic forces are "making the inertial forces smaller". This can be therefore understood, as the aerodynamic effects due to the wind action are reducing the system total stiffness and thus the oscillation natural frequency.

The most important coefficients are the ones relative to the aerodynamic damping, which are H_1^* in the bending case and A_2^* in the torsion case. These aerodynamic coefficients are directly related with the stability conditions, as those exposed in equations (1.14), (1.15), (3.4) and (3.9). In these cases it is stated that instability can only be given if the aerodynamic damping is negative. If that happens, the damping forces measured with wind action will be smaller than those measured without wind action, as the aerodynamic damping will reduce the module of the mechanical one, and the damping coefficient will be consequently positive. The next expression shows conceptually this idea:

$$D_{Coeff} = -D + D_0 = -(D_a + D_0) + D_0 = -D_a \quad (8.1)$$

Where D_{Coeff} is the damping coefficient, D is the damping measured in a test with wind action, D_0 is the damping measured in a test without wind action and D_a is the aerodynamic damping. As it can be seen, a negative aerodynamic damping D_a will result into a positive aerodynamic coefficient D_{Coeff} , which means that there will be risk of galloping oscillations.

Finally, the bridge section will be endangered with flutter oscillations if two conditions are fulfilled at the same time. The first one is that bending and torsion natural frequencies get closer to each other; this means, the torsion natural frequency decreases and the bending natural frequency increases. The second one is that there must be a negative aerodynamic damping, especially in the torsion oscillations. This is, however, not an issue of this work.

In the next sections the resulting bending aerodynamic coefficients will be firstly exposed and commented and secondly compared with results from other works. The same will be done afterwards with the resulting torsion aerodynamic coefficients.

8.2 Bending aerodynamic coefficients

8.2.1 Results and commentaries

This section is aimed to show the obtained bending aerodynamic coefficients and comment which meaning their evolution has. For the first general exposition of the coefficients, the results of the three different excitation frequencies used in the bending tests have been averaged. The differences between the results of each single frequency will be exposed afterwards if necessary, and in any case in the annex. Besides, the fact that the coefficients were determined using discrete values of the reduced velocity results into unnatural, sharp-pointed curves, which had to be smoothed by using polynomial curve fitting. The fitting was done through 7th degrees polynomials fitted with mean squares. Therefore the function “polyfit” from MATLAB was used. The coefficients of the polynomials can be found in annex 11.2.

The evolution of the bending aerodynamic coefficients after averaging and determining the splines is shown in the next image:

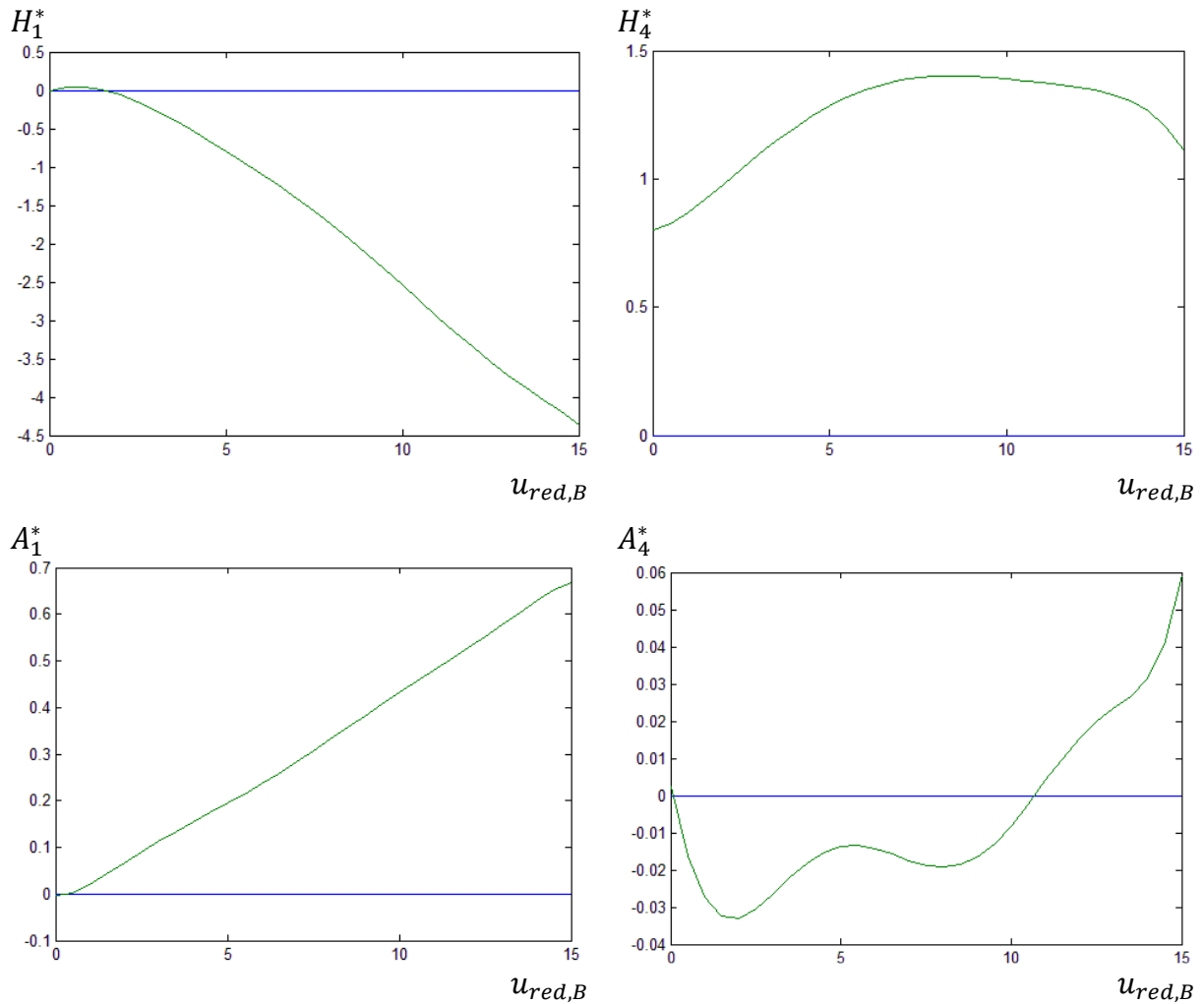


Figure 8.1: Calculated bending aerodynamic coefficients

In the bending tests, the model's susceptibility to bending galloping is studied. Therefore only coefficients H_1^* and H_4^* will be analyzed with detail, as they describe the phenomena related with vertical damping and forces.

Coefficient H_1^* corresponds to the vertical aerodynamic damping forces. As it can be seen in Figure 8.1, the coefficient is negative and even gets more negative for higher wind velocities. This means that bending galloping oscillations cannot be given in this bridge section. As it was said before, a necessary condition for the existence of galloping is a negative aerodynamic damping: in this case, the aerodynamic damping is positive and even gets bigger for higher wind velocities, which makes the aerodynamic damping coefficient decrease when wind velocities grow.

On the other hand, coefficient H_4^* grows until a reduced velocity value of approximately 8, where it stops growing and starts to decrease slightly. The positive coefficient in this case means that the aerodynamic forces reduce the bending stiffness of the system and thus also its bending natural frequency.

8.2.2 Comparison with results of other authors

Comparisons will be done mostly with two other works: the first one is called “*Étude aérodynamique de la passerelle Bercy-Tolbiac Paris*” and is an internal study of the RWTH that was carried out ten years ago in the same wind tunnel, with the same test rig and with the same bridge model. However, there is no documentation about which method or algorithm was used to determine the coefficients. That work will be called here “Internal study” to simplify notation. The second work is “*Zur Identifikation und Berücksichtigung nichtlinearer aeroelastischer Effekte*“ from Hortmanns ([1]). This one was also done in the same wind tunnel and with the same test rig, but the used bridge models consisted exclusively on rectangular sections with different B/d ratios. Therefore comparisons with Hortmanns’ results cannot be taken in such a rigorous way as the comparisons made with the results of the internal study, as section geometry is a determinant factor in the section’s response.

As it can be seen in Figure 8.2, the curve of the coefficient H_1^* found on this work matches the one determined by the internal study.

These results can be also compared with the ones from Hortmanns, even when the sections in both tests are quite different. As the bridge model in this work has a ratio $B/d = 0.329/0.1096 \approx 3$, the results could be compared with the rectangular sections of Hortmanns with ratios $B/d = 2.8$ and $B/d = 3.5$. In the first case, the values from Hortmanns are smaller, and the curve starts to aim to the positive zone after the value $u_{red,B} \approx 15$. In the second one the curves have the same shape, although the values from Hortmanns get more negative sooner. It may be that, the same way the B/d ratio of this work is found between the two studied by Hortmanns, the curve determined here is a “between-case” as well.

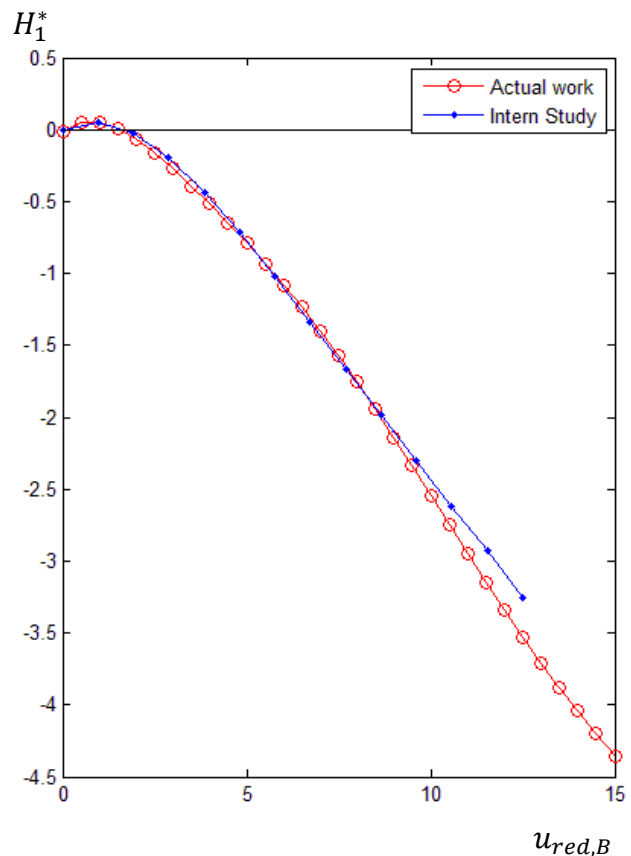


Figure 8.2: Comparison between coefficients H_1^* from this work and from the internal study.

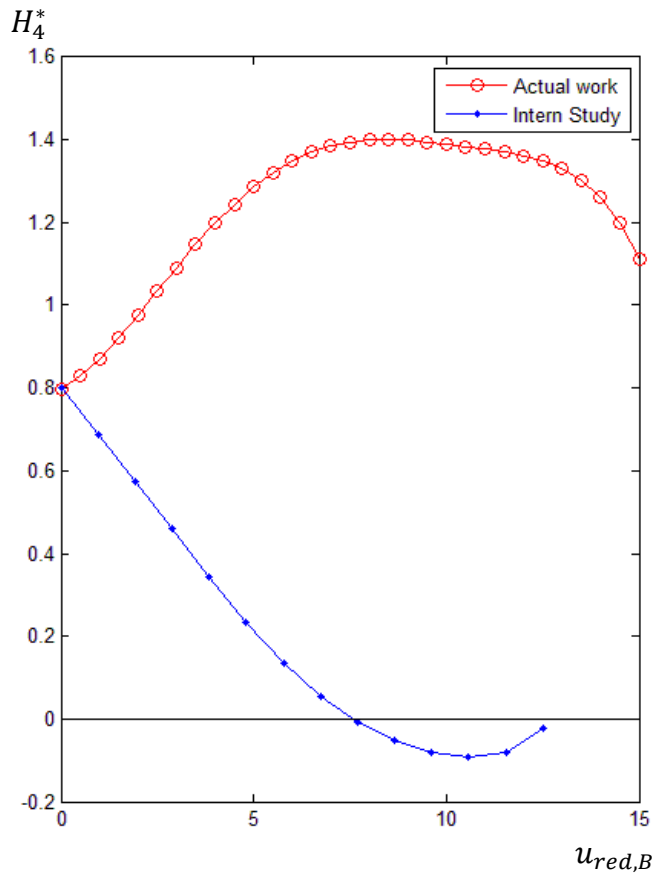


Figure 8.3: Comparison between coefficients H_4^* from this work and from the internal study.

Coefficients H_4^* are, however, not as similar as in the previous case.

Both start at a value of 0.8, which corresponds to the part of the Theodorsen's force. However, while the results found in the internal study show a decreasing curve that starts to increase after the value $u_{red,B} \approx 10$, the curve determined in this work has the opposite trajectory. The curve determined in the internal study shows that the bending stiffness gets higher at first with higher velocities (even gets higher than the one without wind action in a little region), but starts to decrease afterwards. However, the results of this work show that the bending stiffness decreases from the beginning and, after staying almost constant for some reduced velocity values, starts to grow again.

As both curves have the same shape, a thought comes to head that sign mistakes proceeding from the spectral analysis may be the cause for the mismatching between the results.

The results obtained by Hortmanns [1] approximately share the same shape and tendencies as those of the internal study, even though the comparison is made between a rectangular section of ratio $B/d=2.8$ or $B/d=3.5$ and the bridge model used in this work. It can be then said, that the results obtained by Hortmanns do not match the results of this work neither.

The algorithm used in this work was carefully checked in order to find possible mistakes that could lead to an inversion of the H_4^* curve. However, the force was defined in this work to be "in phase" with the acceleration: this means that, whichever the orientation of the angle used in spectral analysis was, the force would always be obtained using the cosine of a small angle, and thus resulting in positive values. This can be better understood observing Figure 6.4: as it can be seen, either if the angles $\beta_{F,y}$ or $\beta_{y,F}$ are used, the cosine will always be positive. The resulting aerodynamic force is also defined in a way that a positive result implies a reinforcement of the movement (see Figure 6.9 and point 5 in section 6.4). As a result, it can be said that either the results are different, or that no mistake has been found so far.

The other 2 coefficients (A_1^* and A_4^*) are compared with the ones obtained in the internal study in the next images:

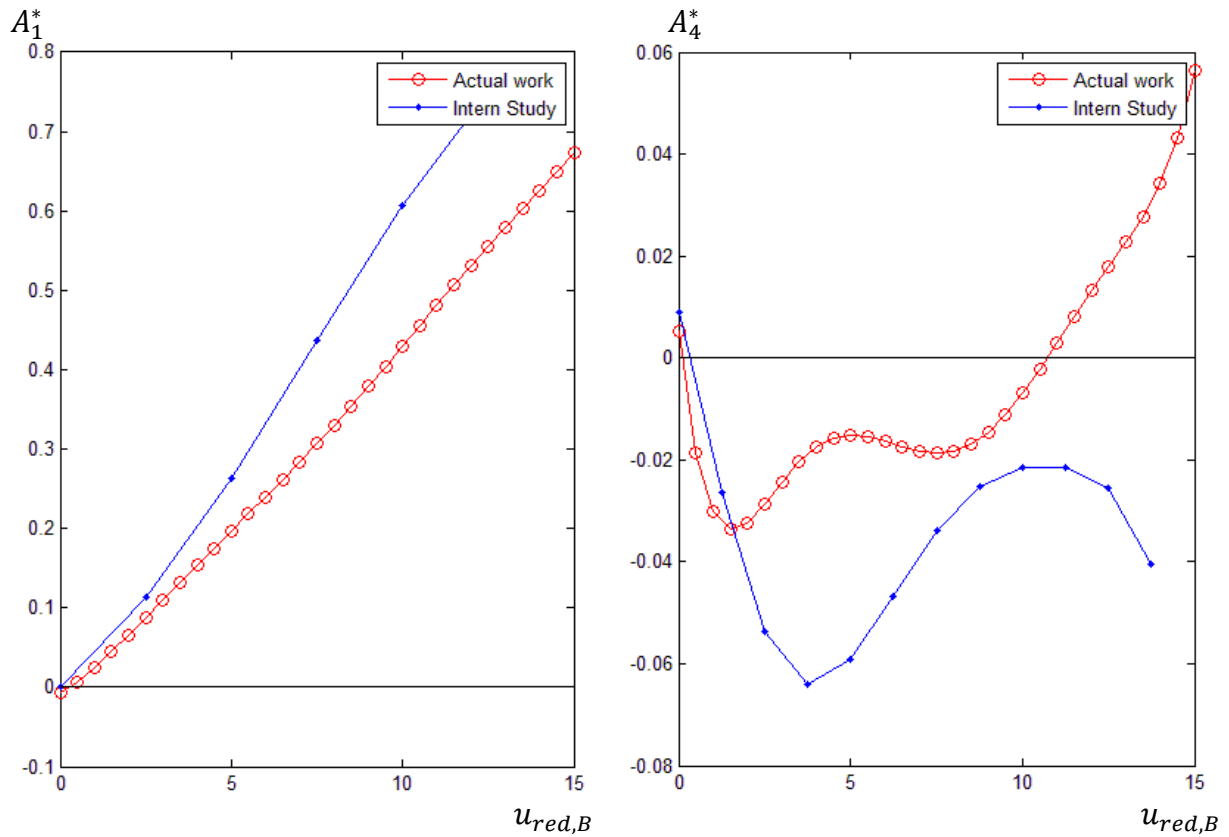


Figure 8.4: Comparison between coefficients A_1^* and A_4^* obtained in this work and those of the internal study.

8.3 Torsion aerodynamic coefficients

8.3.1 Results and commentaries

To show the obtained torsion aerodynamic coefficients, the same process as the one used in the bending case is used (averaging of the coefficients and 7th grade polynomial fitting). It is important to remember that the sign of coefficients H_2^* and H_3^* has been changed before their representation as it was explained in section 7.4.2.2.

Next figure shows the aerodynamic coefficients found with the torsion tests:

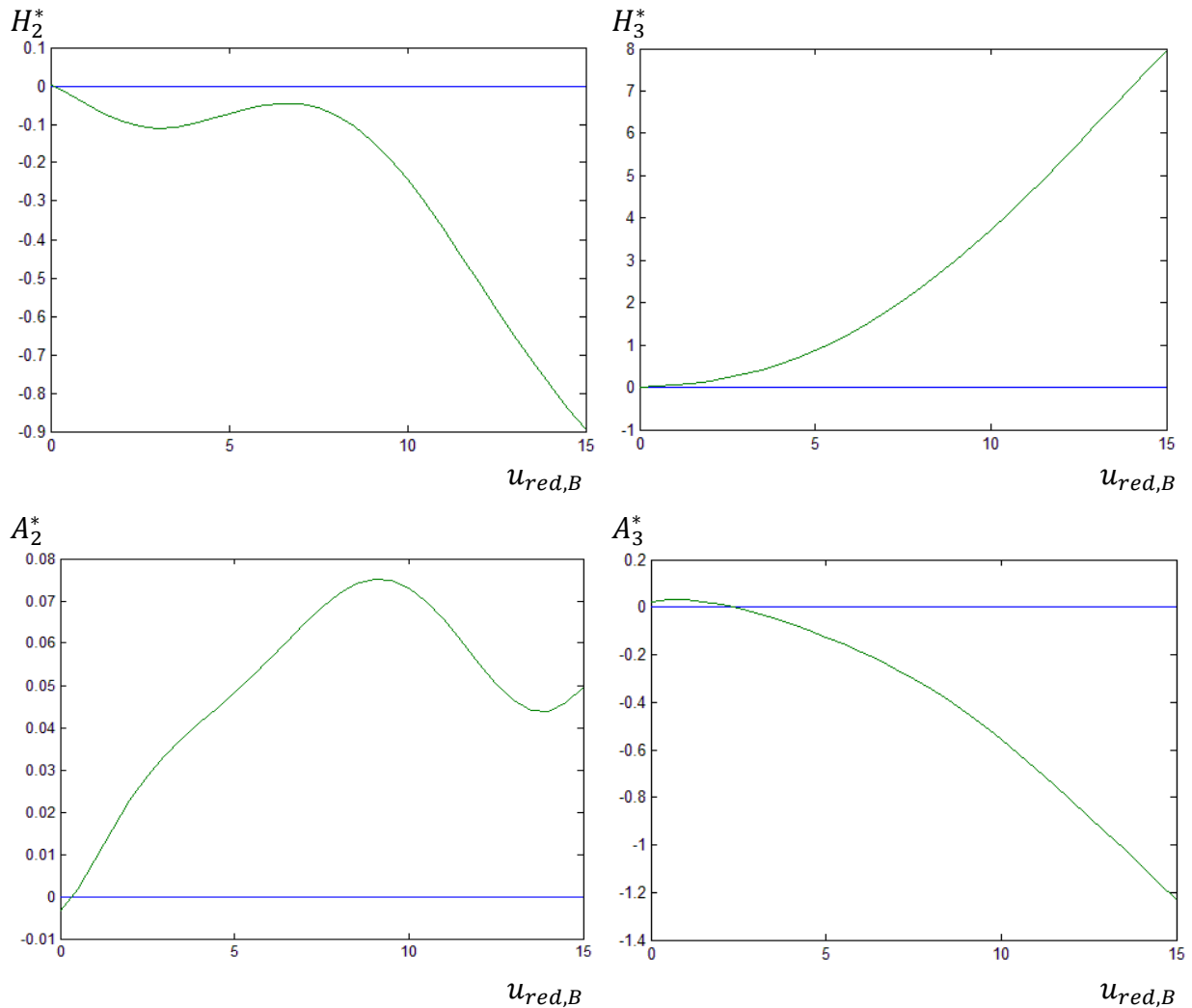


Figure 8.5: Calculated torsion aerodynamic coefficients

In the torsion tests, the model's susceptibility to torsion galloping is studied. Therefore only the coefficients A_2^* and A_3^* will be analyzed with detail, as they describe the phenomena related with moments and torsion damping.

Coefficient A_2^* corresponds to the torsion aerodynamic damping forces. The fact that it doesn't start at point (0,0) in Figure 8.5 is due exclusively to the polynomial fitting.

As it can be seen in the same figure, the coefficient takes growing, positive values from the beginning until $u_{red,B}$ values close to 10, where they start to decrease. At the last $u_{red,B}$ values the coefficient seems to change its tendency again. However, more values at higher $u_{red,B}$ would be necessary to confirm this. It can be also appreciated that, for all wind velocities, A_2^* values are in general close to zero. In any case, it can be assumed that coefficient A_2^* takes only positive values, which implies that the bridge section is endangered with torsion galloping oscillations (see section 8.1).

On the other hand, coefficient A_3^* shows in general a decreasing tendency, which makes its values negative for most wind velocities. The negative coefficient in this case means that the

aerodynamic forces increase the torsion stiffness of the system and thus its torsion natural frequency.

8.3.2 Comparison with results of other authors

Figure 8.6 shows a comparison between the A_2^* curve found in this work and the one found in the internal study. As it can be seen, the results differ in magnitude but not in meaning. In both cases, the results mean that the section can present unstable torsion oscillations, even though the risk is higher in the results of the internal study. It is also important to notice the shape of the curve obtained in this work. It can be observed that for the last $u_{red,B}$ values, the curve changes its tendency twice. The remaining question is then if the curve keeps on growing and therefore presenting a higher probability of instability, or on the contrary, it changes its tendency again.

If the results are now compared with those of Hortmanns (who only tested rectangular sections), the conclusion is similar: In Hortmanns study, all sections and therefore all B/d ratios presented positive A_2^* curves, which implied that all sections could present torsion galloping. Again, that result agrees with the one of this work in meaning, though the curves of Hortmanns present a more pronounced slope.

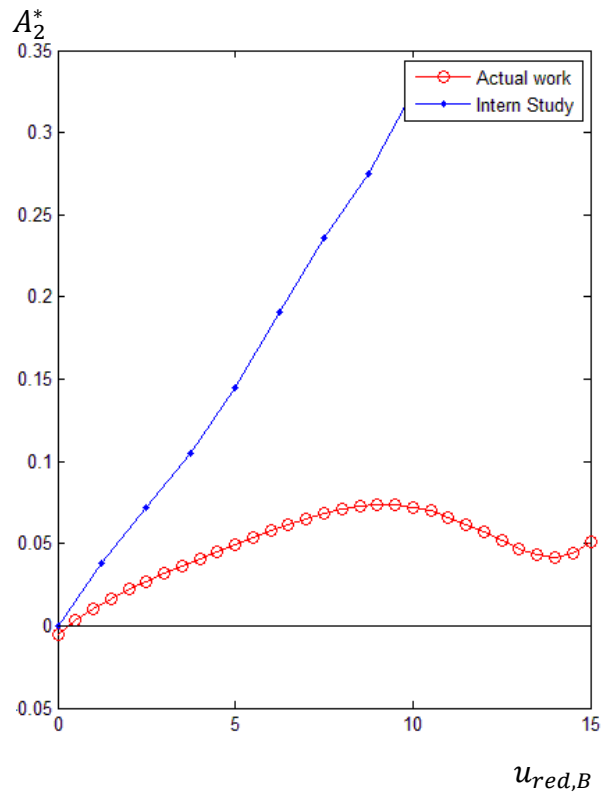


Figure 8.6: Comparison between coefficients A_2^* from this work and from the internal study

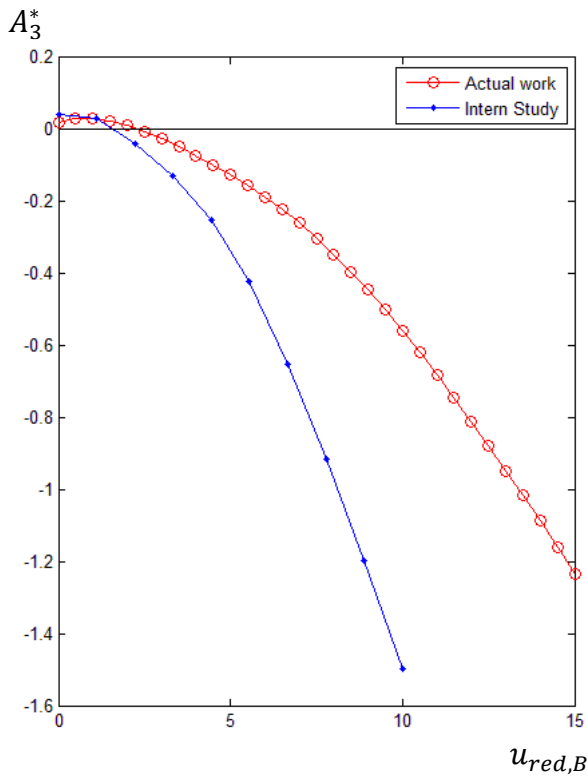


Figure 8.7: Comparison between coefficients A_3^* from this work and from the internal study

Similarly to the case of A_2^* , the curve of coefficient A_3^* matches enough the one determined in the internal study. The tendency is almost identical in both cases, although the values obtained in the internal study are smaller than those of this work (more negative).

The results obtained by Hortmanns show how for low B/d ratios (until 3 approximately) the curves match well the curves determined in this work and, consequently, those of the internal study too. However, it seems that, when the B/d ratios become bigger, the curves stay longer in the positive region before starting to get negative. For yet bigger ratios the tendency becomes the opposite, and the curve values become positive and tend to get even bigger (more positive). However, the ratios in which this phenomenon happens are bigger than approximately 3.5, so they are not suitable for comparisons with the results of this work.

The results of the other two coefficients (H_2^* and H_3^*) are also compared with the internal study:

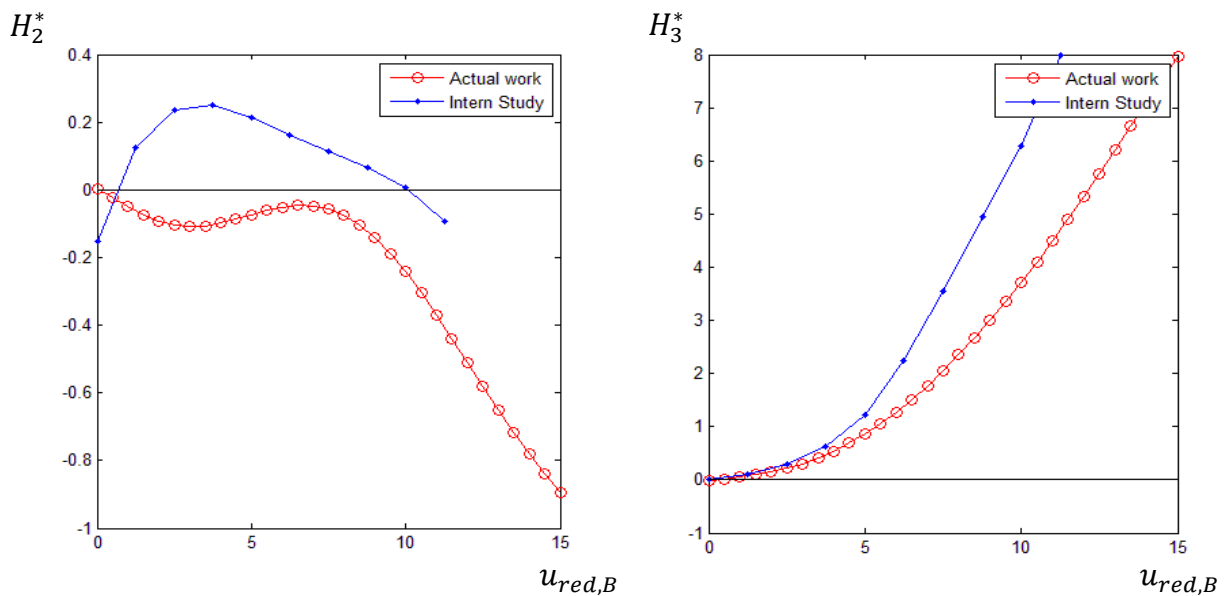


Figure 8.8: Comparison between coefficients H_2^* and H_3^* obtained in this work and those of the internal study.

8.4 Recommendations to improve the quality of the results

This section is aimed to comment some aspects that were found to have a relative big impact in the resulting coefficients and that could only be considered by observing the curves of the results. It also recommends which are the parameters that led to optimal results in this work. These recommended parameters were already implemented in the study case of the Simone-de-Beauvoir footbridge.

The first important consideration deals with the choice of the measurement parameters (as in section 4.4). Normally the resulting aerodynamic coefficients are presented as function of $u_{red,B}$, whose expression can be seen in equation (2.21). According to this equation, the reduced velocity is directly proportional to the undisturbed wind velocity and inversely proportional to the excitation frequency. Therefore it is logic thinking that any excitation frequency may be used as long as the undisturbed wind velocity is also changed appropriately to obtain the desired values of $u_{red,B}$. In this work this has been proven not to be such a simple question. In the first tests carried out to calibrate the measurement parameters, different excitation frequencies were used. They ranged between frequencies of 1.75Hz and 2.75Hz approximately. It could be observed that, in general, lower frequencies presented more dispersion in the results. Next figure illustrates this fact:

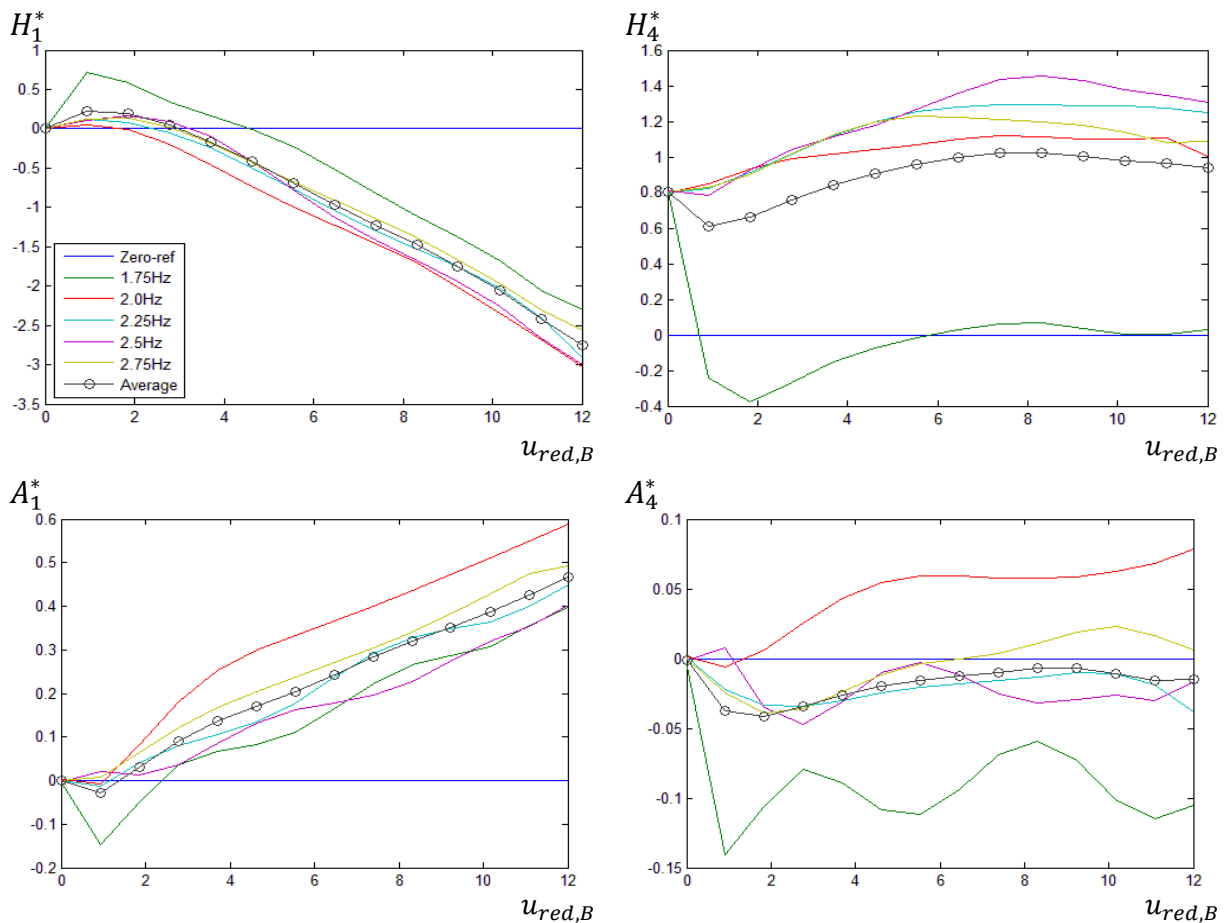


Figure 8.9: Bending aerodynamic coefficients obtained with different excitation frequencies.

It can be seen that, in general, results obtained with excitation frequencies 1.75Hz and 2.0Hz present the curves furthest away from the average curve (which is actually strongly influenced by these two curves, being coefficient H_4^* an extreme case). It is important mentioning that exactly the same algorithm was used for all frequencies, and therefore the differences in the results can only be attributed to additional phenomena occurring when lower frequencies are used. These phenomena may be due to additional distortions in the measurements, to mechanic reasons, as lower frequencies imply lower velocities that may change the nature of the mechanical damping, or even to aeroelastic phenomena. In any case, most authors who present self-calculated aerodynamic coefficients do not indicate which frequencies they used to determine them, probably because it is supposed to be irrelevant. In this work it has been proven that the choice of the excitation frequency is not an irrelevant issue, as lower frequencies present worse results, which may lead to fatal consequences if coefficients are determined using only one low excitation frequency. So after observing the results of this work, in order to minimize risks and obtain the best possible results when determining aerodynamic coefficients, it is recommended to use the maximum achievable excitation frequencies (only limited by model stability and breakdown risk) and, if it is possible, carry out various tests with different frequencies.

Something similar occurs with the chosen amplitude for the model's oscillation. In theory, small amplitudes are preferred to large ones, as the physical phenomena being measured pretends to simulate the beginning of galloping oscillation, and therefore a state in which oscillations still present small amplitudes. They also allow carrying out tests with higher excitation frequencies, as small amplitudes do not cause large inertial forces that could damage the model. Therefore, they seem to be the best choice when setting the oscillation amplitude of the tests. However, when tests were carried out with the minimum oscillation amplitude allowed by the test rig (0.0135m), the obtained results also presented relative high distortions, although smaller than in the case of low excitation frequencies:

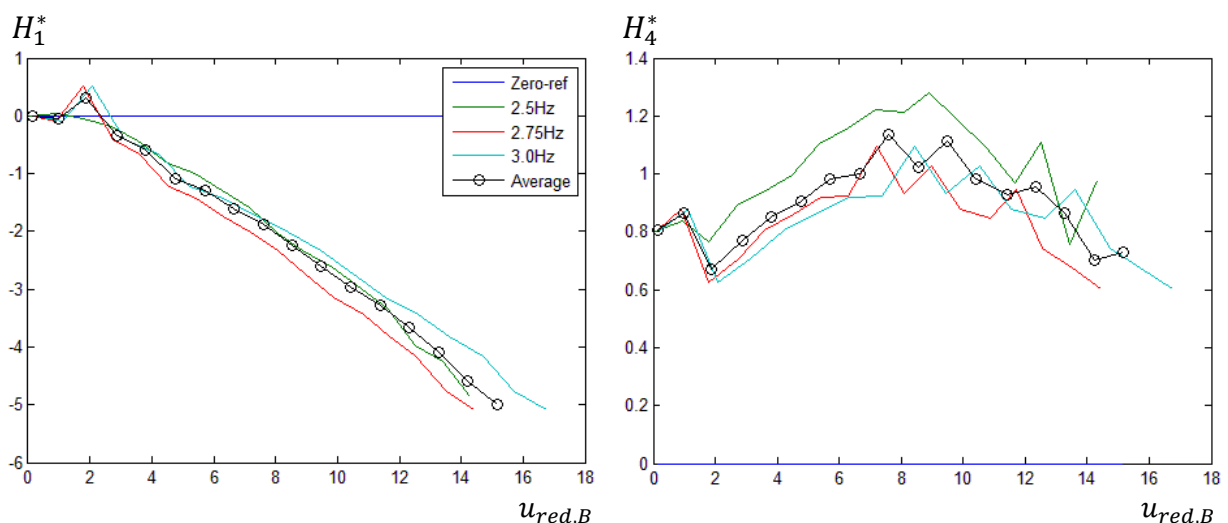


Figure 8.10: Aerodynamic coefficients H_1^* and H_4^* obtained with minimum oscillation amplitude 0.0135m.

As a result, although small oscillation amplitudes are recommended, they must be chosen in a way that, being as small as possible, they do not cause excessive distortions in the results.

Next figure shows coefficients H_1^* and H_4^* determined with the frequencies and oscillation amplitude chosen in this work (2.5Hz to 3Hz and 0.0295m respectively):

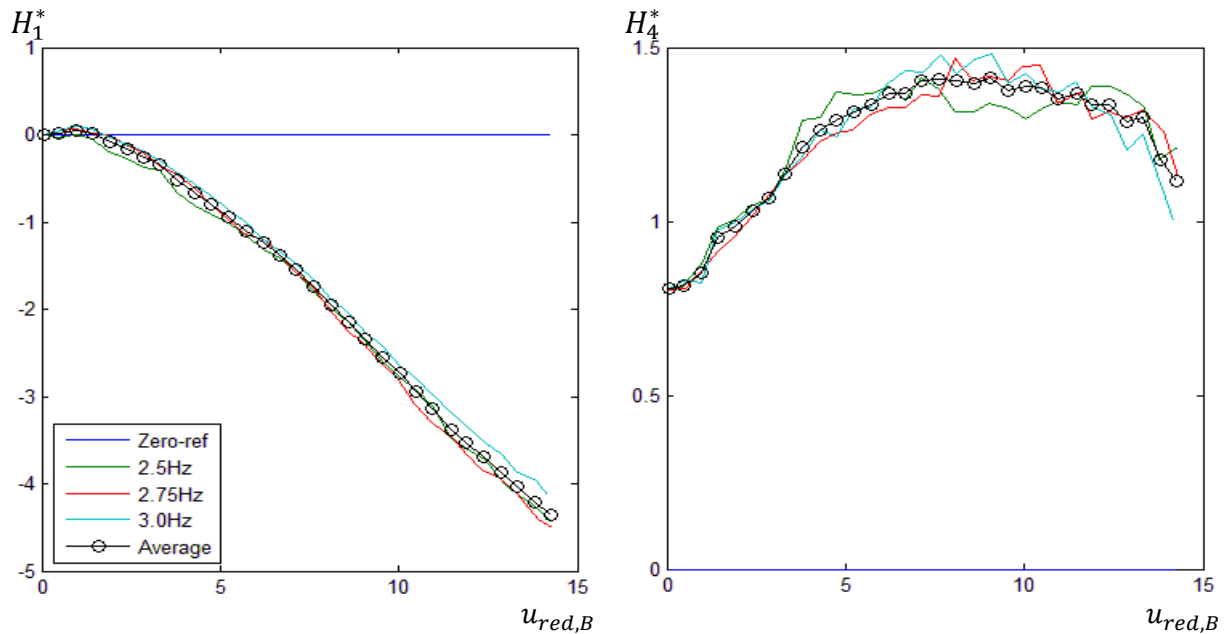


Figure 8.11: Aerodynamic coefficients H_1^* and H_4^* obtained with the recommended parameters.

Finally, in section 5.2.3 the problem relative to the phase displacement between sensors has been mentioned. In this work this phase was taken as negligible because the observed peaks of the different sensors were not further than 0.005 seconds from each other (which in a measurement at 2.5Hz corresponds to a 1% of an oscillation period). It is to prove, if this phase displacement has a real influence in the results and, if it does, in which grade it can impact on the spectral analysis.

9 Conclusions

This work has explained how to determine non-linear, non-stationary aeroelastic coefficients using the forced oscillations method. All procedures, from the measurement of the wind action on the model to the calculation of the coefficients using spectral analysis have been explained with enough detail and thus allowing the reader to have a critical view of every step that has been carried out.

Throughout this algorithm, different aspects have been observed and have led to some important conclusions when determining the aerodynamic coefficients.

For example, it has been proven that high frequencies are preferable to low ones when executing the experiments in order to reduce dispersion in the results. Analogously, it has been seen that the smallest oscillation amplitudes, although possibly representing better the studied problem, may lead to excessive distortion that may excessively worsen the results. In any case, it has been concluded that the apparently simple definition of the reduced velocity does not imply that any excitation frequency can be used indifferently.

When filtering the measured data, the zero-phase filter methods have proven to be the most adequate for this case, as they leave all phase information intact. The band-pass filter design is especially appropriate for this case, as the wanted phenomena occur at a punctual frequency value, and therefore the information corresponding to other frequencies is to be removed.

Spectral analysis tools, although being relatively simple, allow a huge capacity of visualization, understanding and information extraction of the measured magnitudes. Therefore their use is highly recommended to separate, with remarkable simplicity, the different forces and moments that play an important role during the model oscillation.

Through comparison with results of other authors, this algorithm has proved its plausibility when determining non-stationary, aerodynamic coefficients.

However, there are some facts to be considered in future works.

Firstly, the wind tunnel in which the tests of this work were carried out is assumed to present an approximated turbulence grade of $I_u \approx 7\%$. The effect of turbulence in galloping oscillations is in general not clear. Different authors have stated some conclusions about which role turbulence plays, though some of the results seem to be contradictory. Therefore turbulence should be a subject of larger research in the future. The algorithm presented in this work could be used to this end by designing experiments in which the same section (either a bridge section or a rectangular profile) was tested for different turbulence grades. This way the influence of turbulence in galloping instability could be studied by observing the resulting aerodynamic coefficients.

Another aspect to consider is the difference between the results obtained with different measuring methods, especially between those obtained with the free oscillation method and those resulting from the forced oscillation method. The latter one, which is the one used in this work, forces the center of mass to coincide with the center of rotation of the section, which in reality suffers a small displacement during the model's oscillations. The influence of this displacement on the results should be studied in order to check if it is negligible.

Finally, the influence that the phase displacement between the force sensors may have in the resulting coefficients should be studied in order to check if the assumption of its negligibility made in this work is acceptable. A possible mistake should be also searched in the determination of coefficient H_4^* , as its evolution is contrary to that shown by different authors.

Using the algorithm exposed in this work, different bridge sections can be tested with different oscillation amplitudes and inflow attack angles. It is also a useful tool to study the influence that different parameters, design characteristics and boundary conditions may have in a bridge propensity to galloping oscillations, as the effects will be reflected in the aerodynamic coefficients.

And by determining the non-stationary, aerodynamic coefficients of a bridge section, perhaps potential disasters, like the one suffered by the Tacoma Narrows Bridge, will be easier to prevent, thus avoiding the risk of lives and of baseless fear of a construction technology that gets every day more impressive, but not necessarily more insecure.

10 Bibliography

- [1] Hortmanns M.; Zur Identifikation und Berücksichtigung nichtlinearer aeroelastischer Effekte; Aachen 1997; Stahlbau – RWTH Aachen; Heft 34; Shaker Verlag.
- [2] Scanlan R.H., Simiu E.; Wind effects on structures; 1978; Wiley&Sons; New York.
- [3] Reid S.; Wind actions and responses of steel Chimneys; <http://www.scribd.com/doc/38991705/Wind-Actions-and-Responses-of-Steel-Chimneys>.
- [4] Bleich Fr.; Dynamic instability of truss-stiffened suspension bridges under wind action; 1949; ASCE; Transactions; 114; Paper No. 2385.
- [5] Den Hartog J.P.; Mechanische Schwingungen, 1936, Springer Verlag, Berlin.
- [6] Höffer R.; Rechenmodelle für Bewegungsinduzierte Windkraftgrößen auf Brückenüberbauten; 1995; SFB Berichte Nr.27.
- [7] Klöppel K., Thiele F.; Modellversuche im Windkanal zur Bemessung von Brücken gegen die Gefahr winderregter Schwingungen; 1967; Der Stahlbau;36. Jg.; Heft 12.
- [8] Novak M.; Aeroelastic galloping of prismatic bodies; 1969; Journal of the Engineering Mechanics Division; 6394.
- [9] Novak M., Davenport A.G.; Aeroelastic instability of prisms in turbulent flow; 1970; Journal of the Engineering Mechanics Division; 7076.
- [10] Novak M.; Galloping oscillation of prismatic structures; 1972; Journal of the Engineering Mechanics Division; 8692.
- [11] Novak M., Tanaka H.; Effect of turbulence on galloping instability; 1974; Journal of the Engineering Mechanics Division; 10338.
- [12] Parkinson G.V., Smith J.D.; The square prism as an aeroelastic non-linear oscillator; 1964; Quarterly Journal Mechanics and Applied Mathematics; Vol.XVII; Part 2.
- [13] Sakata H.; A study of suspension bridge with shallow box-type suspended structure; Tokio 1971; Proceedings of the Third International Conference on Wind Effects on Buildings and Structures; Part IV.
- [14] Scanlan R.H., Sabzebari A.; Experimental aerodynamic coefficients in the analytical study of suspension bridges; 1969; Journal Mechanical Engineering Science; Vol. 41-44.

- [15] Scanlan R.H., Tomko J.J; Airfoil and bridge deck flutter derivatives; 1971; Journal of the Engineering Mechanics division; 8609.
- [16] Scanlan R.H.; State-of-the-art methods for calculating flutter, vortex-induced, and buffeting response of bridge structures; 1981; Report No. FHWA/RD-80/050.
- [17] Starossek U.; Brückendynamik, Winderregte Schwingungen von Seilbrücken; 1992; Vieweg & Sohn Verlagsgesellschaft mbH, Braunschweig; Wiesbaden; ISBN 3-528-08881-8.
- [18] Theodorsen Th.; General theory of aerodynamic instability and the mechanism of flutter; 1934; Washington D.C.; NACA Report 496.
- [19] Th. v. Kármán; Über den Mechanismus des Widerstandes den ein bewegter Körper in einer Flüssigkeit erfährt; Nachrichten der Königlichen Gesellschaft der Wissenschaften, Göttingen 1991.
- [20] Mitra, S.K., *Digital Signal Processing, 2nd ed.*, McGraw-Hill, 2001.
- [21] Gustafsson, F., Determining the initial states in forward-backward filtering, *IEEE Transactions on Signal Processing*, April 1996, Volume 44, Issue 4
- [22] Rabiner, L.R., and B. Gold. Theory and Application of Digital Signal Processing, Englewood Cliffs, NJ: Prentice-Hall, 1975
- [23] Welch, P.D. "The Use of Fast Fourier Transform for the Estimation of Power Spectra: A Method Based on Time Averaging Over Short, Modified Periodograms." *IEEE Trans. Audio Electroacoust.*, Vol. AU-15 (June 1967)
- [24] Oppenheim, A.V., and R.W. Schaffer. Discrete-Time Signal Processing, Upper Saddle River, NJ: Prentice-Hall, 1999
- [25] Ruscheweyh H.; Dynamische Windwirkungen an Bauwerken; 1982; Bauverlag GmbH Wiesbaden, Berlin; Band 1 und 2; ISBN 3-7625-2007-0.
- [26] DIN 1055, Teil 40; Lastannahmen für Bauwerke, Windwirkungen auf Bauwerke; Normenausschuß Bauwesen im DIN, Deutsches Institut für Normung e.V., Mai 1989.
- [27] Eurocode EC 1; Basis of Design and Actions on Structures; Part 2.4: Wind Actions; CEN/TC 250/SC3; 1992; ENV 1993-1-1.
- [28] http://en.wikipedia.org/wiki/Tacoma_Narrows_Bridge_%281940%29
- [29] http://en.wikipedia.org/wiki/Aeroelastic_flutter#Flutter
- [30] <http://www.me-systeme.de/sensorik/kraftsensoren/index.html>

11 ANNEX

11.1 7th degree polynomial coefficients:

Bending Coefficients

	x^7	x^6	x^5	x^4	x^3	x^2	x^1	x^0
H_1^*	-3,06E-07	1,22E-05	-0,00014421	-8,49E-05	0,01381032	-0,1179605	0,15550134	-0,00877308
H_4^*	-1,37E-07	6,33E-06	-0,0001275	0,00155179	-0,01223064	0,04783182	0,03169995	0,79941583
A_1^*	-1,91E-07	1,05E-05	-0,00022774	0,00249549	-0,01434763	0,04118597	-0,00726518	-0,00198547
A_4^*	1,19E-07	-5,28E-06	8,14E-05	-0,00042513	-0,00107702	0,01725821	-0,04569534	0,00245898

Torsion Coefficients

	x^7	x^6	x^5	x^4	x^3	x^2	x^1	x^0
H_2^*	4,98E-08	-4,66E-06	0,00015298	-2,23E-03	0,0138764	-0,02562185	-0,03656393	0,00252003
H_3^*	-1,72E-07	7,89E-06	-0,00013333	0,00086421	0,00016289	0,01714681	0,03728179	-0,00565577
A_2^*	8,12E-08	-4,40E-06	9,10E-05	-0,00090268	0,00441774	-0,00918641	-0,00641008	0,0033353
A_3^*	-5,00E-08	1,95E-06	-2,06E-05	-6,90E-05	0,00249726	-0,02031459	0,02561911	0,02272945

11.2 Filter information

The filter was design using MATLAB functions “fdesign.bandpass”, “design” and “filtfilt”.

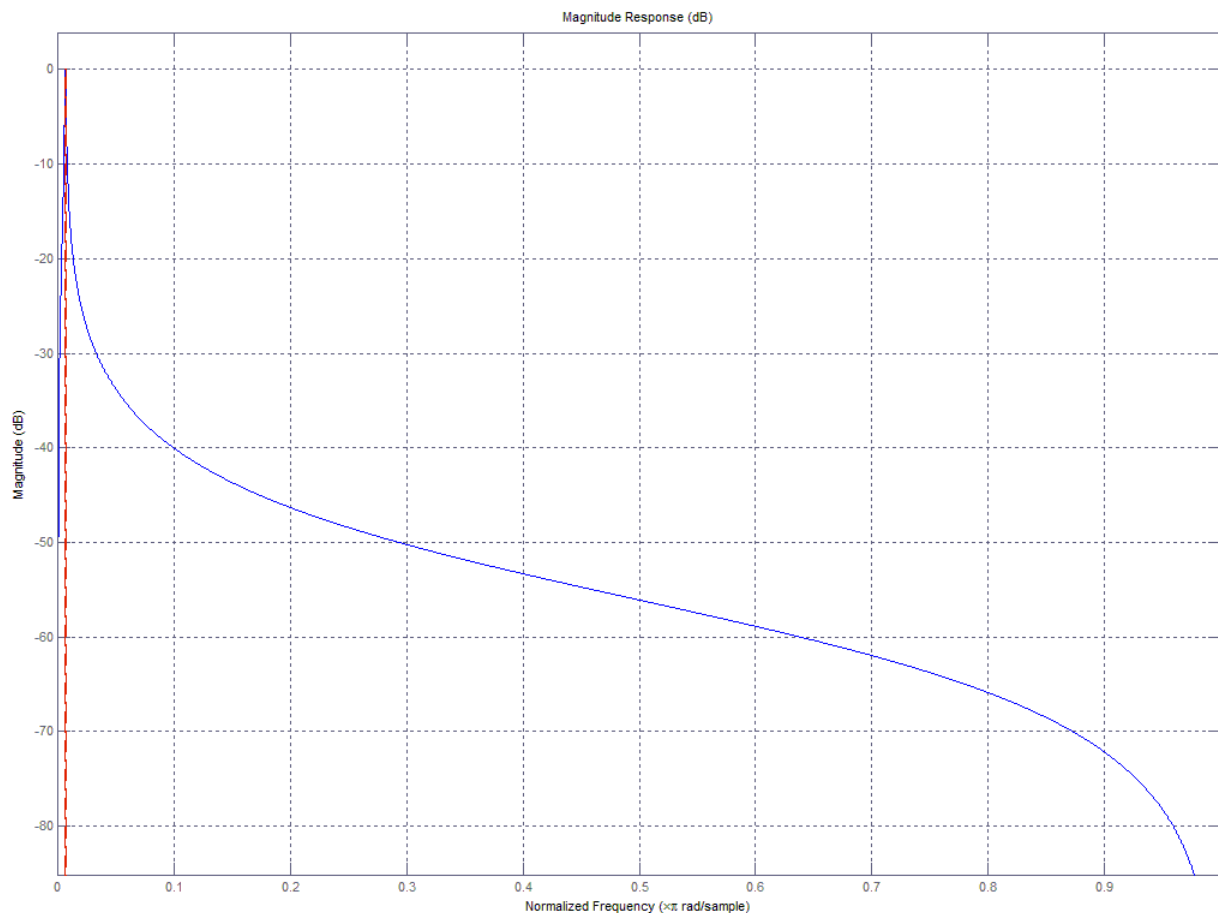
The script used to design it is written below:

```
FilterGrad=2; % Filtergrad
SampleRate=1000;% Sample Rate
Datfreq=2.5101;
h=fdesign.bandpass('N,F3dB1,F3dB2',FilterGrad,(Datfreq*0.25)/(SampleRate/2),
    (Datfreq+0.25)/(SampleRate/2));
Hd=design(h,'Butter');
"Filtered-Signal"=filtfilt(Hd.sosMatrix,Hd.ScaleValues,"Original-Signal")
```

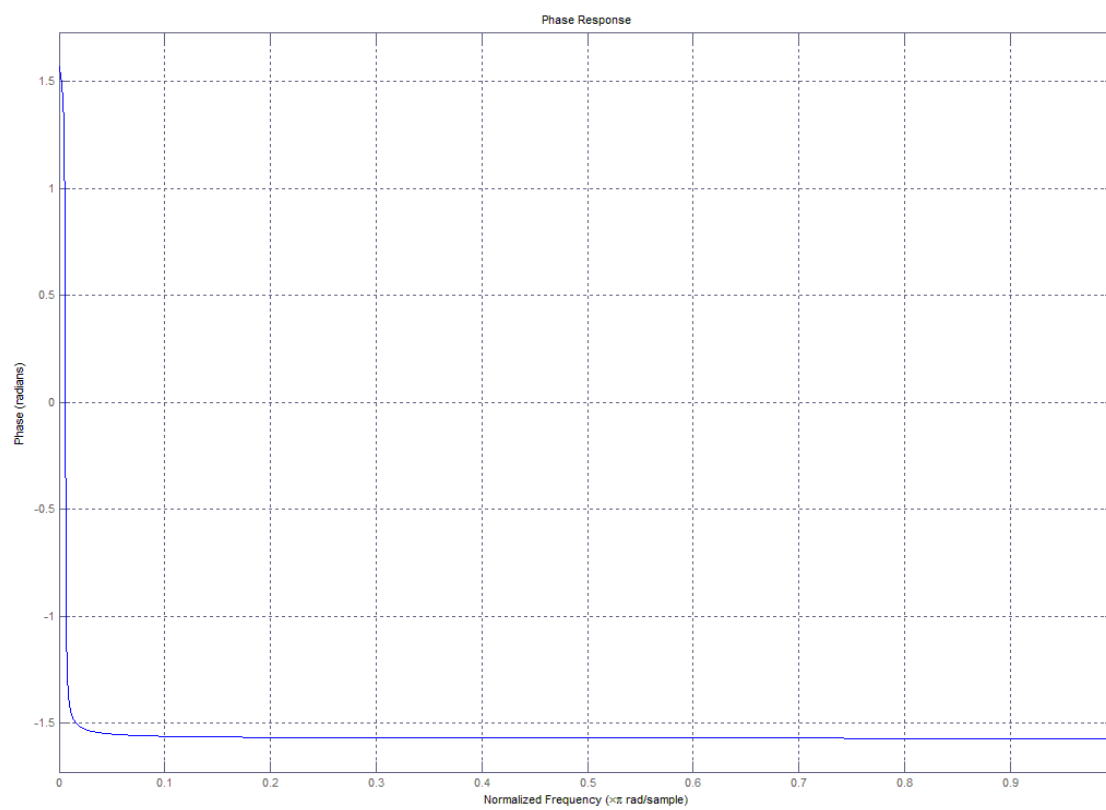
The filter properties are represented below:

Magnitude

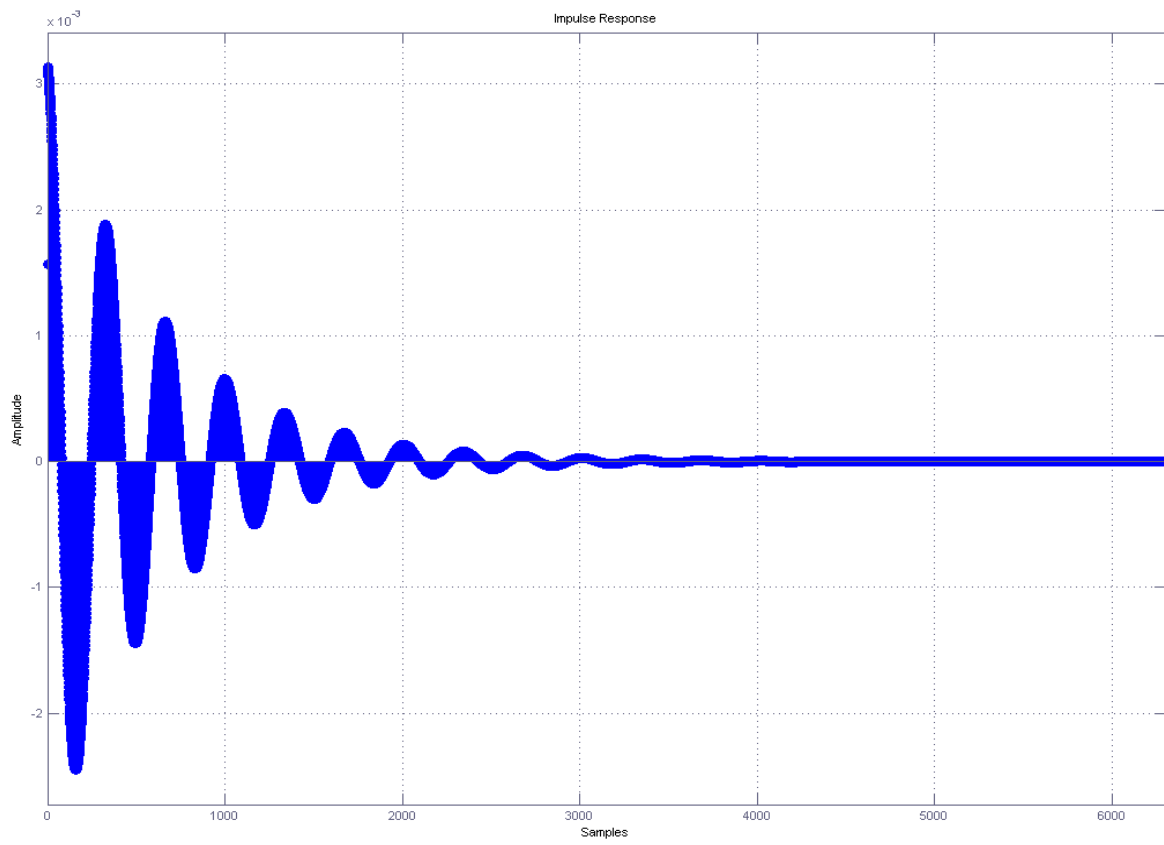
response:



Phase response:



Impulse response:



Filter information:

```

Discrete-Time IIR Filter (real)
-----
Filter Structure      : Direct-Form II, Second-Order Sections
Number of Sections   : 1
Stable                : Yes
Linear Phase         : No

Design Method Information
Design Algorithm      : butter

Design Options
Scale Norm           : no scaling

Design Specifications
Sampling Frequency    : N/A (normalized frequency)
Response              : Bandpass
Specification         : N,F3dB1,F3dB2
Filter Order          : 2
First 3-dB Point     : 0.0054968
Second 3-dB Point    : 0.0064968

Measurements
Sampling Frequency    : N/A (normalized frequency)
First Stopband Edge   : Unknown
First 6-dB Point      : 0.0051723
First 3-dB Point      : 0.0054968
First Passband Edge   : Unknown
Second Passband Edge  : Unknown
Second 3-dB Point     : 0.0064968
Second 6-dB Point     : 0.0069044
Second Stopband Edge  : Unknown
First Stopband Atten. : Unknown
Passband Ripple       : Unknown
Second Stopband Atten. : Unknown
First Transition Width : Unknown
Second Transition Width : Unknown

Implementation Cost
Number of Multipliers : 3
Number of Adders       : 3
Number of States       : 2
Multiplications per Input Sample : 3
Additions per Input Sample : 3

```

Filter Coefficients:

```

-----
Section #1
-----
Numerator:
 1
 0
-1
Denominator:
 1
-1.9965114351885698
 0.99686333183344433
Gain:
0.001568334083277838
-----
Output Gain:
1

```

11.3 Force Transducers



Model 208C02

Product Type: Load Cell, Force Sensor

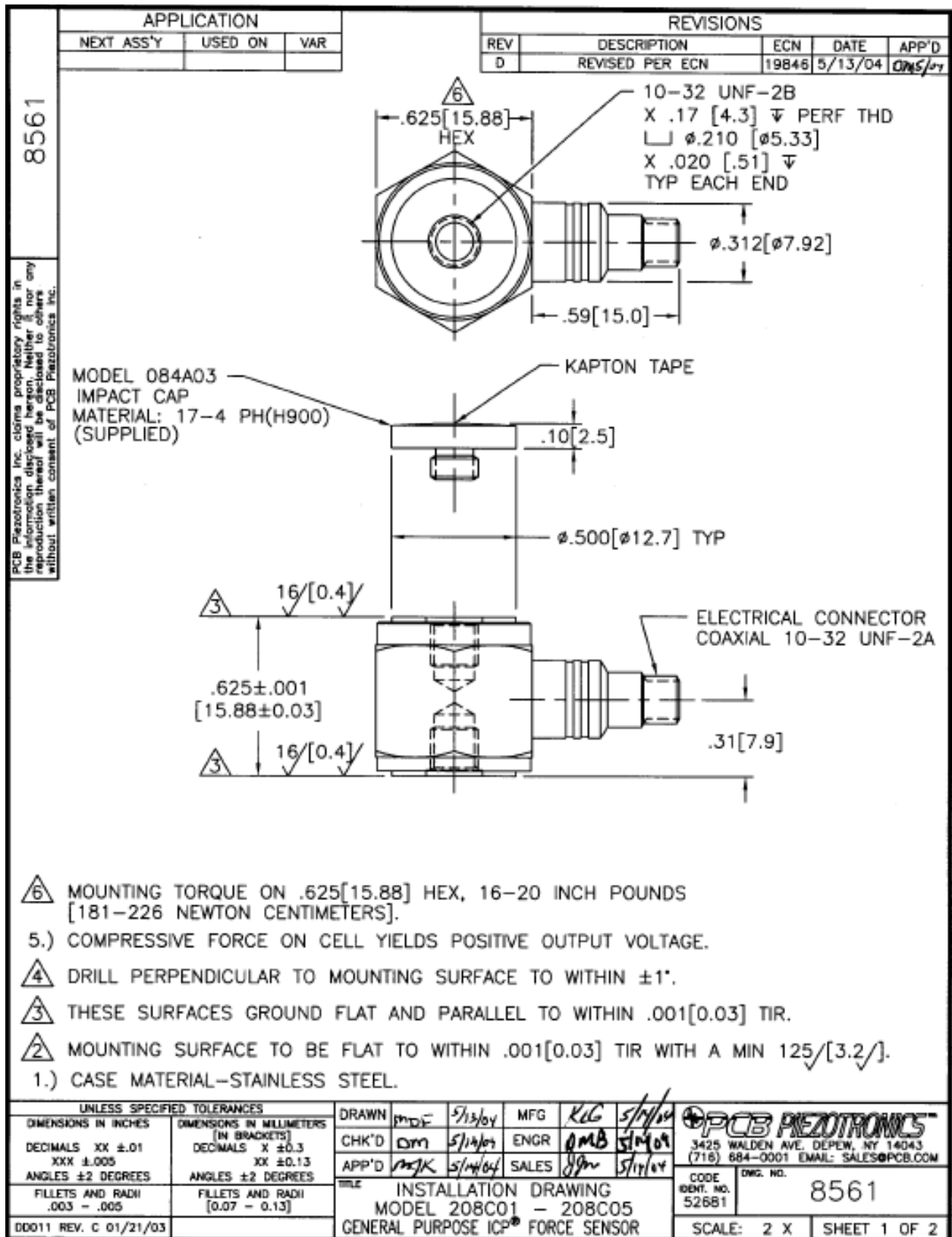
Multi-purpose, ICP® force sensor, 100 lb comp., 100 lb tension, 50 mV/lb

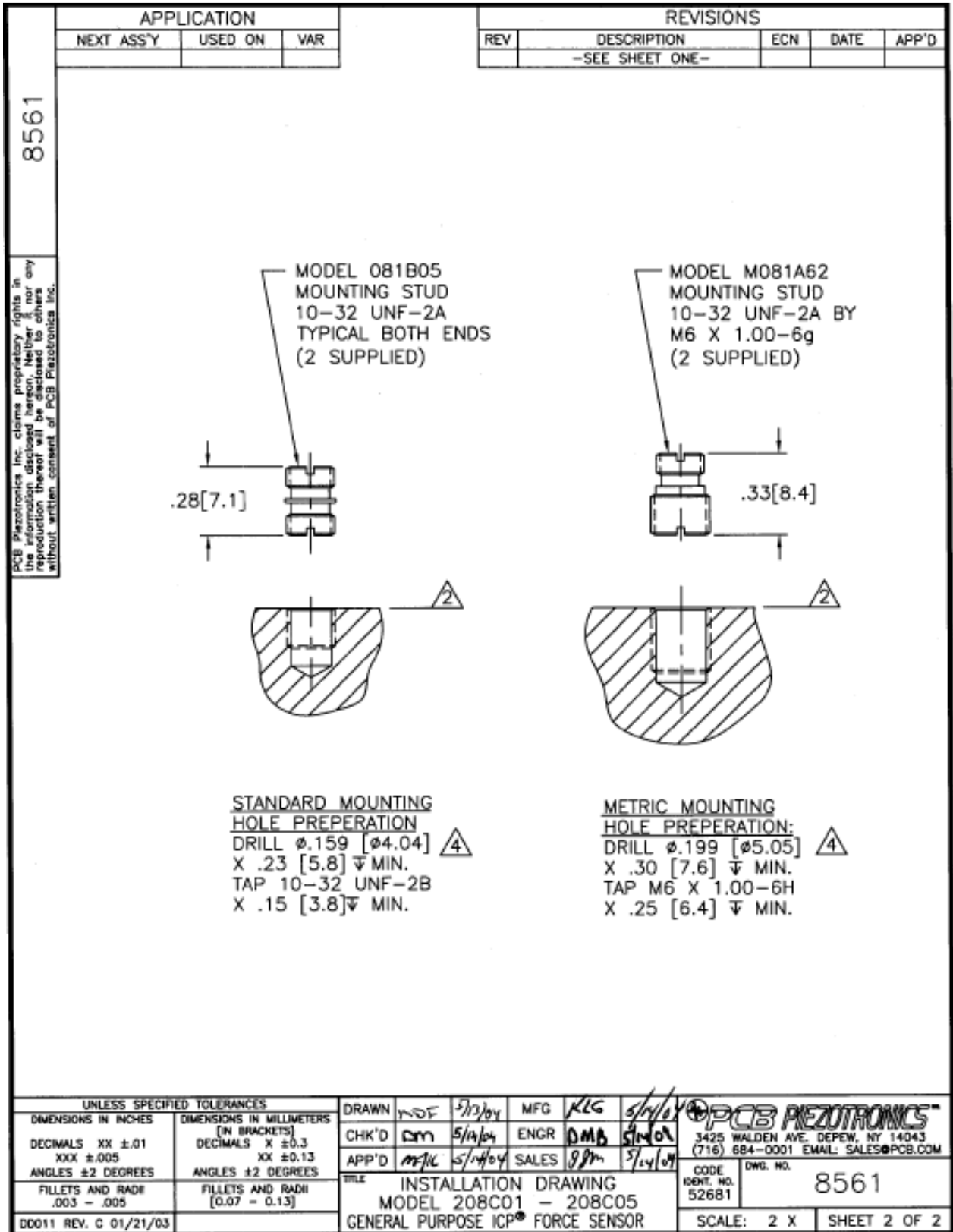
PERFORMANCE	ENGLISH	SI
Sensitivity(± 15 %)	50 mV/lb	11,241 mV/kN
Measurement Range(Compression)	100 lb	0.4448 kN
Measurement Range(Tension)	100 lb	0.4448 kN
Maximum Static Force(Compression)	600 lb	2.669 kN
Maximum Static Force(Tension)	500 lb	2.224 kN
Broadband Resolution(1 to 10,000 Hz)	0.001 lb-rms	0.004 N-rms [1]
Low Frequency Response(-5 %)	0.001 Hz	0.001 Hz [2]
Upper Frequency Limit	36 kHz	36 kHz [3]
Non-Linearity	≤ 1 % FS	≤ 1 % FS [4]
ENVIRONMENTAL		
Temperature Range	-65 to +250 °F	-54 to +121 °C
Temperature Coefficient of Sensitivity	≤ 0.05 %/°F	≤ 0.09 %/°C
ELECTRICAL		
Discharge Time Constant(at room temp)	≥ 500 sec	≥ 500 sec
Excitation Voltage	20 to 30 VDC	20 to 30 VDC
Constant Current Excitation	2 to 20 mA	2 to 20 mA
Output Impedance	≤ 100 ohm	≤ 100 ohm
Output Bias Voltage	8 to 14 VDC	8 to 14 VDC
Spectral Noise(1 Hz)	0.000135 lb/√Hz	0.000603 N/√Hz [1]
Spectral Noise(10 Hz)	0.0000276 lb/√Hz	0.000123 N/√Hz [1]
Spectral Noise(100 Hz)	0.0000096 lb/√Hz	0.0000427 N/√Hz [1]
Spectral Noise(1 kHz)	0.0000021 lb/√Hz	0.0000095 N/√Hz [1]
Output Polarity(Compression)	Positive	Positive
PHYSICAL		
Stiffness	6 lb/μin	1.05 kN/μm [1]
Size (Hex x Height x Sensing Surface)	0.625 in x 0.625 in x 0.500 in	15.88 mm x 15.88 mm x 12.7 mm
Weight	0.80 oz	22.7 gm
Housing Material	Stainless Steel	Stainless Steel
Sealing	Hermetic	Hermetic
Electrical Connector	10-32 Coaxial Jack	10-32 Coaxial Jack
Electrical Connection Position	Side	Side
Mounting Thread	10-32 Female	Not Applicable
Mounting Torque(Recommended)	16 to 20 in-lb	181 to 226 N-cm
SUPPLIED ACCESSORIES:		
Model 080A81 Thread Locker (1)		
Model 081B05 Mounting Stud (10-32 to 10-32) (2)		
Model 084A03 Impact Cap (1)		
Model M081A62 Mounting stud, 10-32 to M6 x 1, BeCu with shoulder (2)		
OPTIONAL VERSIONS		
N- Negative Output Polarity		
Output Polarity(Compression)	Negative	
W- Water Resistant Cable		

All specifications are at room temperature unless otherwise specified.

NOTES:

- [1] Typical.
- [2] Calculated from discharge time constant.
- [3] Estimated using rigid body dynamics calculations.
- [4] Zero-based, least-squares, straight line method.





More information can be found in the next link:
http://www.pcb.com/contentstore/docs/PCB_Corporate/ForceTorque/products/Manuals/208C02.pdf

11.4 Images of the test rig

This section contains some pictures of the test rig that may make easier the understanding of its working.

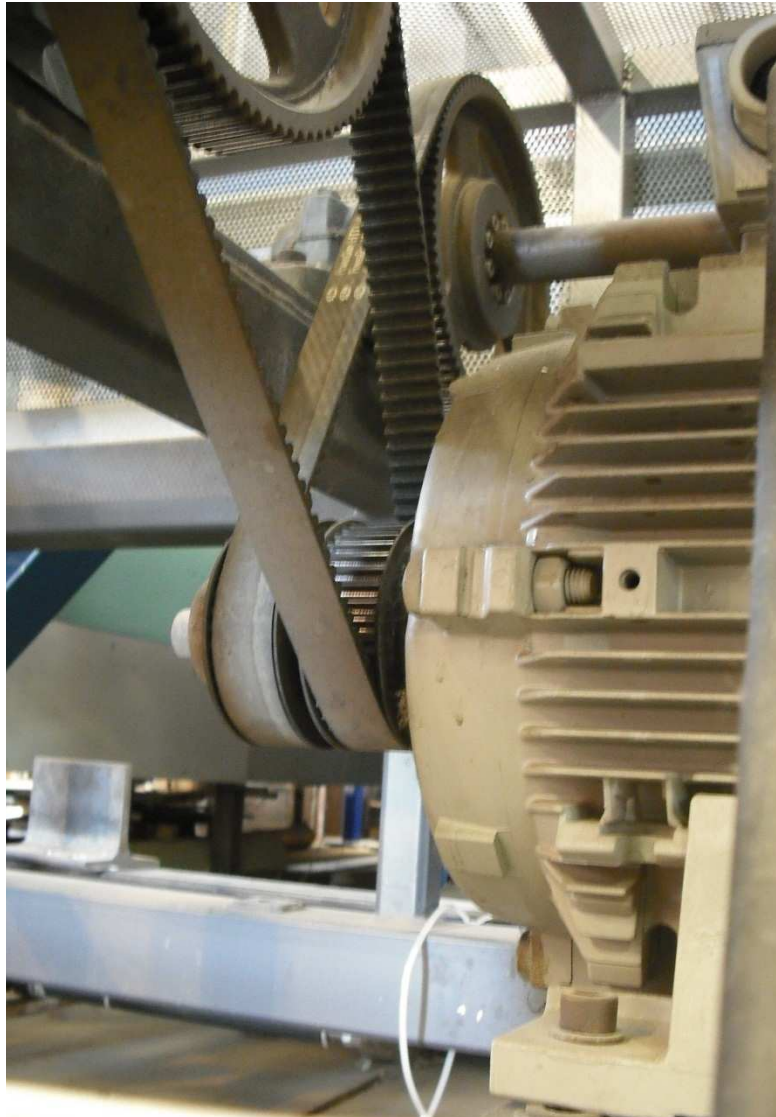


Figure 11.1: Cogged belts connecting the motor to the rotation transmitters.



Figure 11.2: Rotation transmitters moves by the cogged belts connected to the motor.



Figure 11.3: General view of the test rig in front of the wind tunnel.



Figure 11.4: Side-view of the test rig during a torsion test.



Figure 11.5: Frontal view of the test rig during a torsion test.

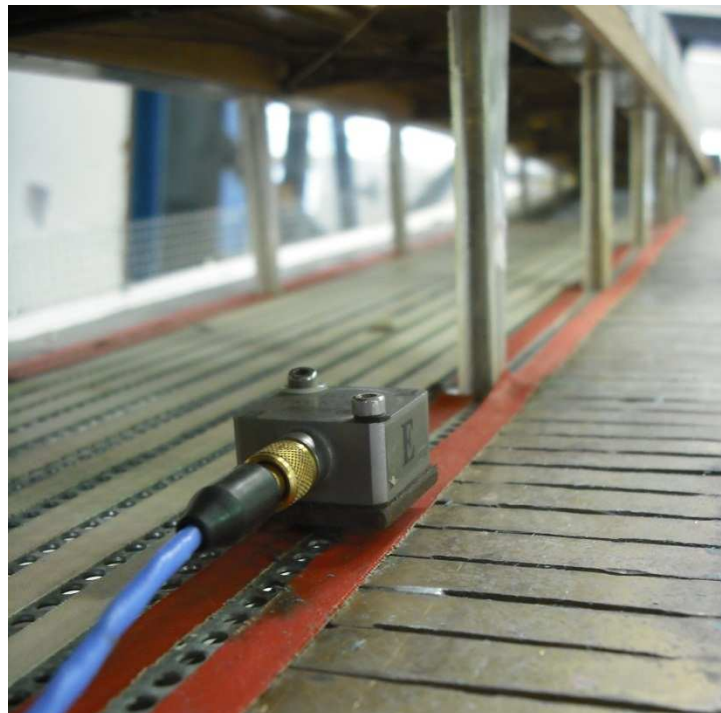


Figure 11.6: One of the two accelerometers located at middle section.



Figure 11.7: Accelerometer located at one side of the plate of one extreme of the model.

